COMPENSATION FOR THREE-COIL WIRELESS POWER TRANSFER FOR MISALIGNMENT AND EFFICIENCY IMPROVEMENT IN WIRELESS CHARGING SYSTEM

PEYMAN DARVISH

FACULTY OF ENGINEERING
UNIVERSITY OF MALAYA
KUALA LUMPUR

2021

COMPENSATION FOR THREE-COIL WIRELESS POWER TRANSFER FOR MISALIGNMENT AND EFFICIENCY IMPROVEMENT IN WIRELESS CHARGING SYSTEM

PEYMAN DARVISH

DISSERTATION SUBMITTED IN PARTIAL FULFILMENT OF THE REQUIREMENTS FOR THE DEGREE OF ENGINEERING SCIENCE

**FACULTY OF ENGINEERING
UNIVERSITY OF MALAYA
KUALA LUMPUR**

2021

UNIVERSITY OF MALAYA

ORIGINAL LITERARY WORK DECLARATION

Name of Candidate: Peyman Darvish

Matric No: 17058159/1

Name of Degree: Master of Engineering Science

Title of Dissertation

COMPENSATION FOR THREE-COIL WIRELEE POWER TRANSFER FOR MISALIGNMENT AND EFFICIENCY IMPROVEMENT IN WIRELESS CHARGING SYSTEM

Field of Study: Power Electronics

I do solemnly and sincerely declare that:

(1) I am the sole author/writer of this Work;
(2) This Work is original;
(3) Any use of any work in which copyright exists was done by way of fair dealing and for permitted purposes and any excerpt or extract from, or reference to or reproduction of any copyright work has been disclosed expressly and sufficiently and the title of the Work and its authorship have been acknowledged in this Work;
(4) I do not have any actual knowledge nor do I ought reasonably to know that the making of this work constitutes an infringement of any copyright work;
(5) I hereby assign all and every rights in the copyright to this Work to the University of Malaya ("UM"), who henceforth shall be owner of the copyright in this Work and that any reproduction or use in any form or by any means whatsoever is prohibited without the written consent of UM having been first had and obtained;
(6) I am fully aware that if in the course of making this Work I have infringed any copyright whether intentionally or otherwise, I may be subject to legal action or any other action as may be determined by UM.

Candidate's Signature Date: 19/08/2021

Subscribed and solemnly declared before,

Witness's Signature Date: 25 Aug 2021

Name: Sulaiman Wadi Harun

Designation: Professor
Jabatan Kejuruteraan Elektrik
Universiti Malaya
Kuala Lumpur

ABSTRACT

Wireless power transfer (WPT) using two or more magnetic resonance is commonly known as inductive power transfer (IPT). This technology can transfer power over distances without physical contact, offering significant benefits to modern automation systems duo its convenience, environmentally friendly, and efficient power transfer. Two coil WPT system is the most popular design over the past decades. However, recent studies have proven that a three-coil WPT design shows better performance and has higher efficiency compared to the two coil designs. This is especially critical when the source resistance and transmission distance between the primary and receiver coil increases.

Li-ion batteries are the most commonly used batteries for Electric Vehicles (EVs) applications because of their longer cycle life, higher power density, and improved battery safety. A constant current (CC) charging process followed by a constant voltage (CV) charging mode is the preferred charging technique for Li-ion batteries. Generally, in the first stage of battery charging which is commonly known as CC mode, the battery voltage rises quickly until it reaches its predetermined voltage level while the current remains the same. In the second stage of the charging process, the battery voltage remains constant, and the magnitude of the current begins to reduce. Once the current drops to almost zero, the charging process will be stopped. This technique of charging has been adopted in Two-coil WPT systems. Moreover, Zero Phase Angle conditions (ZPA) for both modes could be achieved to reduce the reactive power, increase efficiency, and prevent the hard switching of the MOSFETs.

Three-coil WPT system, similar to two-coil system, is capable of achieving constant output current and constant output voltage with ZPA. However, in the CV mode of the conventional three-coil design, the efficiency of the light load system dramatically decreases as the load becomes smaller. Genreallly, In this work, a new Series-Series-LCLCC (S-S-LCLCC) compensation design for three-coil WPT system with load-independent output voltage, which is capable of realizing ZPA characteristics during the entire process of charging process, is proposed. The new design is capable of significantly improves the energy efficiency stiffness against the load variation, misalignment, increases the flexibility to optimize the system efficiency, reduces the voltage stress and increases the power delivery to load compared to the conventional topology. Moreover, the quality factor analysis for both conventional and the new design has been simulated, and the results show the novel system has the potential to improve the overall performance. The lab-made experimental design of a three-coil S-S-LCLCC WPT system with power rating of 420W and 96 V output voltage shows that the overall trend of efficiency of the proposed design is higher than the conventional S-S-S design as the load decreases and the new system has approximately 10% higher efficiency when the battery equivalent load resistance reaches 222 Ω. Moreover, the new design shows much better performance than the conventional system in the case of misalignment. Simplified models of S-S-LCLCC and S-S-S have also been successfully proposed and tested in this work to ease the simulation and the theoretical analysis.

ABSTRAK

Pemindahan kuasa tanpa wayar (WPT) menggunakan dua atau lebih resonans magnetik biasanya dikenali sebagai pemindahan kuasa induktif (IPT). Teknologi ini dapat mentransfer kuasa dari jarak jauh tanpa hubungan fizikal, memberikan manfaat yang besar kepada sistem automasi moden yang memudahkan, mesra alam, dan pemindahan tenaga yang cekap. Sistem WPT dua gegelung adalah reka bentuk yang paling popular sejak beberapa dekad yang lalu. Walau bagaimanapun, kajian baru-baru ini membuktikan bahawa reka bentuk WPT tiga gegelung menunjukkan prestasi yang lebih baik dan mempunyai kecekapan yang lebih tinggi berbanding dengan reka bentuk dua gegelung. Ini sangat kritikal apabila rintangan sumber dan jarak penghantaran antara gegelung utama dan penerima meningkat.

Bateri Li-ion adalah bateri yang paling biasa digunakan untuk aplikasi Kenderaan Elektrik (EV) kerana jangka hayatnya lebih lama, ketumpatan kuasa yang lebih tinggi, dan keselamatan bateri yang lebih baik. Proses pengecasan arus tetap (CC) diikuti dengan mod pengecasan voltan malar (CV) adalah teknik pengecasan yang disukai untuk bateri Li-ion. Secara amnya, pada tahap pertama pengisian bateri yang biasanya dikenali sebagai mod CC, voltan bateri naik dengan cepat sehingga mencapai tahap voltan yang telah ditentukan sementara arus tetap sama. Pada peringkat kedua proses pengecasan, voltan bateri tetap berterusan, dan besarnya arus mula berkurang. Setelah arus turun hampir menjadi sifar, proses pengecasan akan dihentikan. Teknik pengisian ini telah diadopsi dalam sistem WPT Two-coil. Lebih-lebih lagi, keadaan Zero Phase Angle (ZPA) untuk kedua-dua mod dapat dicapai untuk mengurangkan daya reaktif, meningkatkan kecekapan, dan mencegah pertukaran MOSFET secara sukar.

Sistem WPT tiga-gegelung, serupa dengan sistem dua-gegelung, mampu mencapai arus keluaran tetap dan voltan keluaran tetap dengan ZPA. Walau bagaimanapun, dalam mod CV reka bentuk tiga gegelung konvensional, kecekapan sistem beban ringan menurun secara mendadak apabila beban menjadi lebih kecil. Secara genre, dalam karya ini, dicadangkan reka bentuk pampasan Series-Series- LCLCC (SS-LCLCC) baru untuk sistem WPT tiga-gegelung dengan voltan keluaran bebas beban, yang mampu merealisasikan ciri-ciri ZPA selama keseluruhan proses pengisian, dicadangkan . Reka bentuk baru ini mampu meningkatkan kekukuhan kecekapan tenaga dengan ketara terhadap variasi beban, ketidaksejajaran, meningkatkan fleksibiliti untuk mengoptimumkan kecekapan sistem, mengurangkan tegangan voltan dan meningkatkan penyampaian daya untuk memuat berbanding dengan topologi konvensional. Lebih-lebih lagi, analisis faktor kualiti untuk reka bentuk konvensional dan baru telah disimulasikan, dan hasilnya menunjukkan sistem novel berpotensi meningkatkan prestasi keseluruhan. Reka bentuk eksperimental buatan makmal 420W dengan voltan keluaran 96 V menunjukkan bahawa trend kecekapan keseluruhan reka bentuk yang dicadangkan lebih tinggi daripada reka bentuk SSS konvensional kerana beban menurun dan sistem baru mempunyai kecekapan sekitar 10% lebih tinggi apabila bersamaan bateri rintangan beban mencapai 222 Ω. Lebih-lebih lagi, reka bentuk baru menunjukkan prestasi yang jauh lebih baik daripada sistem konvensional sekiranya berlaku ketidaksejajaran. Model ringkas S-S-LCLCC dan S-S-S juga telah berjaya dicadangkan dalam karya ini untuk memudahkan simulasi dan analisis teoritis.

ACKNOWLEDGEMENTS

I would like to express my deep gratitude to my supervisors, Professor Dr. Saad Mekhilef and Associate Professor Ir. Dr. Hazlee Azil Illias. Their great help has made my study at the University of Malaya possible. They have given me invaluable guidance, inspiration and suggestions in my quest for knowledge. Without their good supervision, this thesis would not have been possible and I am eternally grateful to them for their assistance. I would like to express my great appreciation to Marif Daula Siddiqui and Asif Mustafa, who guided me on this journey as my elder brother and fellow researcher.I would also like to thank Dr. Nadia Tan Mei Lin as well for allowing me use UNITEN University Laboratory to get some parts of my experimental results and I am very thankful for her great help, guidance, suggestions and for providing me with the essential facilities to complete my research.

TABLE OF CONTENTS

LIST OF FIGURES

LIST OF TABLES

LIST OF SYMBOLS

V_{in}	:	Input DC Voltage
V_1	:	Square wave form of the fundamental harmonic voltage
C_i	:	Resonant Capacitor
L_i	:	Resonant Inductance
L_{LR}	:	Leakage Inductance
L_M	:	Mutual Inductance
K	:	Coupling coefficient
R_{L}	:	Load Resistnace
Q	:	Quality Factor
C_B	:	Filter output Capacitor
ω	:	Operating Angular Frequency
f	:	Resonant Frequency
R_{ds}	:	MOSEFET Drain to Source Resistance
θ	:	Phase Angle of the Input Voltage
I_1	:	Inverter Current
I_{1s}	:	Primary Coil Current
I_{0s}	:	Receiver Coil Current
I_B	:	Battery Current
I_{1n}	:	Primary Coil Current of S-S-LCLCC Topology
V_{0n}	:	Out put voltage of S-S-LCLCC Topology
Zin_{3s}	:	Input impedence of S-S-S system
Zin_{3n}	:	Input impedence of S-S-LCLCC system
η	:	Efficiencyof WPT system
α	:	Capacitance Ratio of S-S-LCLCC system

LIST OF ABBREVIATIONS

PDL	:	Power Delivery to Load
PTE	:	Power Transfer Efficiency
WPT	:	Wireless Power Transfer
EV	:	Electric Vehicle
CC	:	Constant Curent
CV	:	Constant Voltage
PWM	:	Pulse Width Modulation
ESR	:	Equivalent Series Resistnace
ZVS	:	Zero Voltage Switching
RMS	:	Root of Mean Square
CP	:	Circular Coil
RP	:	Rectangular Coil
QC	:	Quadrature Coil
ZPA	:	Zero Phase Angel
CPT	:	Capacitive Power Transfer
IPT	:	Inductive Power Transfer
DWC	:	Dynamic Wireless Charging
AWG	:	American Wire Gauge
SWC	:	Static Wireless Charging
PHEV	:	Plug in Hybrid Eletric Vehicle
FEA	:	Finite Element Analysis

CHAPTER 1: INTRODUCTION

1.1 Research background

Consumer electronics, commercial electronics, and autonomous cars have all seen strong growth in the last decade (EVs). However, the most significant impediment to their continued expansion is battery technology. The range of EV cars in comparison to galion vehicles are significantly lower due to the capacity of commercialized lithium-ion (Li-Ion) batteries. According to (Hui, Zhong, & Lee, 2014), the energy density of Li-Ion batteries is only 100–250 Wh/kg, compared to 12000 Wh/kg of gasoline. The batteries cost an average of $200 to $400 per kWh and they are heavy and more expensive. Additionally, depending on the power level of the EV, the charging time of a Li-Ion battery may take about half an hour or until several hours, which is way longer than petrol and gasoline refueling. To fix the power constraint without needing a significant investment in battery systems, a lightweight, efficient and ubiquitous charging solution is needed. Increasing the cruising range entails adding more battery cells and parts to the car, which increases its weight and cost.

Wireless power transfer (WPT) technology has been developed and studied thoroughly in recent years as an alternative charging mechanism to conductive charging methods. Modern technology uses a pair of physically separating couplers to replace the wired interface, allowing energy to be transmitted without touching and wirelessly, which in comparison to traditional conductive power transfer, WPT technology features high application convenience and adaptability. Moreover, WPT system reduces the need for bulky charging cables and connections, as well as being weather-resistant and vandalism-resistant. WPT was first proposed more than a century ago by scientist Nikola Tesla but it took time for the technique to develop and become a theoretically viable and economically successful solution. In recent years, WPT becomes more popular due to offering the EV battery to be charged at any time and in any place, even when the vehicle is in motion, due to the power supply and the powered device are coupled through the magnetic field (Zakerian, Vaez-Zadeh, & Babaki, 2020). Hence, by using dynamic WPT it is possible to prevent the issue where the battery runs out of power before it reaches to the destination (Feng et al., 2020). Moreover, in a traditional plug-in system, there are issues of worn conductor and insulation caused by friction of the contact because of the environment. In WPT system, these problems are removed, which increases the safety and reliability of the system (S. Li, Li, Deng, Nguyen, & Mi, 2015). Because of these advantages, WPT techniques are widely adopted for applications from low-power electronic devices to high-power EV systems. Moreover, this technique can be used for the application where automated, space-isolated and reliable power transfer is needed. All these advantages have made wireless power transfer convenient for implementing it in a large scale to ensure safe charging like electric and electrified transportation charging system.

Wireless charging can be classified into stationary, quasi-stationary and dynamic. Public charging points, households and offices will all benefit from stationary wireless charging. The main use of quasi-stationary charging can be found at traffic lights, laybys and rest areas along highways, as an extension of stationary charging. With dynamic wireless charging, a BEV's range anxiety can be mitigated (Y. Li et al., 2019).

Nowadays, high-power Stationary Wireless Charging (SWC) technology has gradually matured. In 1997/1998, IPT – stationary charging Technology demonstrated an electric vehicle with wireless charging at Rotorua Geothermal Park in New Zealand, followed by the first bus charging wirelessly at bus stops in Genoa and Turin in 2002. WiTricity, Qualcomm, Conductix- Wampfler, Momentum Dynamics and Bombardier are among the major companies conducting research and implementing stationary WPT for EV (Fisher, Farley, Gao, Bai, & Tse, 2014). WiTricity is a spin-off from the Massachusetts Institute of Technology (MIT). They have developed transmitter and receiver that operate on strongly coupled magnetic resonance. WiTricity has reported system efficiency of around 90% for 3.3kW power rating operating at 145 kHz with lateral misalignment of ±20cm and ±10cm bumper to bumper. Qualcomm's Halo partnered with the University of Auckland to develop "Double D" polarised magnetic pads that can provide twice the power rating with better performance than circular pads running at a frequency of 20kHz . However this claim was not entirly fair since the total dimentions of the DD and circular coil were not the same. Later on, (Bandyopadhyay, Venugopal, Dong, & Bauer, 2019) shows that for a specific dimension, circular coils are capable of providing the highest efficiency in comparison to other coil design. In Torino, Italy, Conductix-Wampfler has installed stationary charging for the electric bus. They tune each system's resonant frequency to achieve 90% efficiency at a 40mm separation gap for 60kW power transfer (Patil et al., 2018). Momentum Dynamics has developed a stationary WPT system with a power transfer efficiency of 92 percent with an air gap of 24 inches at 3.3kW. The charger can also be upgraded to 7.2kW and 10kW, allowing it to charge the Chevy Volt in around an hour. The WPT system from Momentum Dynamics is currently being installed in select FedEx trucks from Smith EVs(Conductix-Wampfler, 2013). HEVO Power is in the process of putting its plan into implementation as well.

The attempt to improve charging a moving vehicle has gained attention in recent years. The idea of automatically charging an EV at bus stops, shopping centers, or even traffic lights, where EVs densely assemble or make stops along the route (Mohamed, Lashway, & Mohammed, 2017), can ease the charging process compared to conventional manual charging. Moreover, dynamic wireless charging can help to reduce the battery capacity and the limited cruising range. Despite the implementation of DWC system demand has high initial cost, according to the literature (S. Jeong, Jang, & Kum, 2015), the long-term advantages of adding DWC facilities the initial installation costs and the total cost will not rise dramatically, making dynamic wireless charging a financially feasible option.

This is due to in theory, it is possible to reduce battery capacity and solve the issue of limited cruising range (Chopra & Bauer, 2013).

1.2 Problem statement

Over the past decade, the majority of the studies regarding wireless charging have been focusing on Inductive Power Transfer (IPT) in EVs (Khaligh & Dusmez, 2012; Nagendra, Covic, & Boys, 2014). The quality factor, coupling coefficient and compensation circuit are playing a critical role in the system efficiency (Tran, Vu, & Choi, 2018). Coil designs in WPT have a crucial influence on improving quality factor and coupling coefficient. Many different coil design and control techniques have been proposed to improve the misalignment performance, efficiency, ZPA, constant output characteristics, voltage/current stress and cost of the WPT system. Compensation methods are another approach to improve the overall system efficiency. By regulating the frequency and designing the compensation tank, it is possible to realize Zero Phase Angle (ZPA) across the inverter of WPT system to eliminate or minimize the reactive power, which will decrease the inverter losses, reduce the voltage and current stress and contribute the system to operate in soft-switching mode during the entire process of charging. This eventually leads the system to have higher efficiency (Tran et al., 2018).

Generally, there are two main stages to charge lithium ion batteries, which is considered as one of the most suitable batteries for Electric Vehicle. In the initial stage, the battery voltage rapidly increases while the charger charges the battery in CC mode until the voltage across the battery reaches its maximum charge. In the second stage, the CC charging process will be replaced with CV mode and eventually, when the current is becoming relatively small, the charging process will stop.

In order to design a CC/CV charger for EVs, researchers have investigated the characteristics of load-independent output voltage and current of two coil system.

Other approaches have adopted the analysis on the effects of intermediate coils to further increase the transmission distance, power delivery to the load and the efficiency of a WPT topology. It has been shown in (Kiani, Jow, & Ghovanloo, 2011) that over the distance of 12cm, the efficiency and power delivery of three and four coils system are significantly higher in comparison to conventional two coils designs. The attempt to achieve high efficiency three-coil design in (Y. Li et al., 2018), a three-coil wireless charger, which can achieve both CC/CV and capable of operating in soft switching mode, is implemented and tested. Achieving CV in (Y. Li et al., 2018) has been done by using S-S-S compensation, which has better performance than S-S compensation in two-coil design (J. Zhang, Yuan, Wang, & He, 2017). However, the system efficiency dramatically decreases as the load power decreases during this stage. Therefore, to further improve the three coil system efficiency at CV mode, a new compensation technique is required.

1.3 Objectives of Study

The overall goal of this study is to develop a novel compensation topology for three-coil WPT system to improve the misalignment and energy efficiency stiffness of the wireless charging system. The specific objectives of this study are as follows:

1. To design a novel compensation topology for three-coil WPT system to improve the energy efficiency stiffness against the load variation and misalignment
2. To examine the design flexibility of the new system and optimize the system efficiency
3. To simulate the proposed topology and perform hardware implementation
4. To evaluate the constant voltage and zero phase angle performance of the proposed converter for a wide range of load resistances

1.4 Thesis Outline

This study proposes a novel topology for three coils resonant WPT system that is suitable for charging an EV's battery. This research work is divided into 5 chapters and is organized as follows:

Chapter 2 presents a detailed literature survey of the IPT. Different topologies are discussed on the basis of achieving constant output current/voltage with ZPA. Moreover, the detailed pros and cons of the recent magnetic couplers are discussed in this chapter.

Chapter 3 presents the detailed operation of the proposed topology. It represents the FHA to simplify the analysis of the circuit. It also discusses the detailed influence of the additional components and explains in detail how the proposed system can improve the overall performance of the three coil system when mutual inductance between relay and receiver coil is small.

Chapter 4 shows the experiment results of the proposed system for the wide load. Moreover, the experimental effect of misalignment of both conventional and proposed system together some discussions are also discussed.

Finally, Chapter 5 summarizes and concludes the main contributions of the report and discusses future work as well.

CHAPTER 2: LITERATURE REVIEW

2.1 Introduction

This chapter first discusses a quick summary of WPT based on different physical principles and then focuses on IPT charging system for EVS application. Recent compensation topologies, coil designs and power electronics works for high power wireless chargers, together with their details pros and cons, are also discussed in this chapter.

2.2 WPTS technologies

The histroy of WPT spans from Hertz's groundbreaking efforts to the present. In 1890, Nikola Tesla conducted his experiments on the transmission of power by radio waves. His first attempt at transmitting power was in 1899 at Colorado Springs, Colorado. In his laboratory, he created a large coil with a copper ball positioned on a tower. Although it is found in some recent literature that the Tesla coil was designed to resonate at a frequency of 150 kHz while supplied with 300 kW ("The Lost Journal of Nikola Tesla," 2016), there is no proof of its successful demonstration. In the 1960s, a far-field (radiative) wireless power transfer system was demonstrated by William C. Brown. Microwave technology could be demonstrated by the development of klystron, magnetron tubes and parabolic antennas. William C. Brown later demonstrated short-range transmission from 475 W of microwaves to DC performance at 54 percent DC in 1975 (Patil et al., 2018). Following this, Brown and Robert Dickinson transmitted 30 kW DC output power over a distance of 1.5 km at NASA's Jet Propulsion Laboratory. In 2007, Tesla's experiment based on a coupled-mode theory using magnetic resonance with an efficiency of 40 percent over a distance of 2 m was replicated by a group of researchers from MIT using coupling coils with a radius of 30 cm. Over the past centuraty many other work by other great researchers have been done which have contributed the world to use WPT technology in a more efficient way. Overall The WPT Technology can be applied on the basis of various physical concepts.

This technology is primarily classified into three groups of microwave radiation WPT, capacitive WPT and inductive WPT according to the medium for power accumulation and transmission (Dai & Ludois, 2015; Sasaki, Tanaka, & Maki, 2013).

2.2.1 Microwave radiation-based WPT

WPT systems are based on microwave transmit energy by spatial microwave directional radiation. A DC signal is converted to microwaves by an RF power amplifier. Then, the transmitting antenna sends the microwave beam out. The transmitting antenna is configured to absorb microwaves and ultimately rectifies them into the DC source that the equipment will use. The microwave-based WPT is primarily used in long-distance and high-power WPT applications due to its characteristics, such as long transmission distance and potential high power capability. Previously, this technique was used in solar space power plants, microwave aircraft and wireless inter-island transmissions (McSpadden & Mankins, 2002; Shinohara, 2013). There were several attempts to power an aircraft model by the use of microwaves at 2.45 GHz as early as 1988. The transfer power of the system was 10 kW, which is capable of moving an aircraft model of 2.9 x 4.5 m^2, 150 meters above the ground. Mitsubishi Electric partnered with Kyoto University to design a commercial EV microwave charging device for EV charging applications. To pass 1 kW to the receiving antenna mounted on the vehicle chassis, they used magnetron-based 2.45 GHz microwaves. The end-to-end efficiency of the experiment was above 70%. The possible effect of microwave radiation on the human body and the difficulty of safely orienting the microwaves are the key problems in implementing this technology for EV charging. Furthermore, for wider applications of high-power charging systems, the performance of such systems needs to be improved.

2.2.2 Inductive WPT

The most widely studied and employed WPT method is WPT via near-field magnetic coupling. The receiver coil picks up the magnetic field produced by the high-frequency current in primary coils in magnetically coupled systems and converts it to DC current for charging. A magnetically-coupled near-field coils with their primary and secondary windings separated by a large distance can be regarded as a loosely coupled transformer (Yilmaz & Krein, 2013). The leakage of loosely coupled coils is much greater than in standard transformers because of the wide air gap and the resulting coupling factor is typically below 0.3. Efficient power transmission can still be realized considering the low coupling if the quality factor of coils is correctly optimized (Waffenschmidt & Staring, 2009). The WPT efficiency is proportional to that of conductive charging. Hundreds of kilowatts have already hit the power stage and megawatts of power can also be obtained by paralleling several modules or implementing polyphase systems (J. H. Kim et al., 2015). In addition, several tens of centimeters are reached by the vertical air difference and horizontal permissible misalignment and are equivalent to half of the coil diameter. The theory of magnetic resonance was suggested for WPT systems in 2008. However, it is basically a unique case when the quality factor of an air-core coil is increased by the excitation of the MHz range to adjust for the decrease in the coupling factor, such that even large air gaps can achieve high-efficiency power transfer (Ho, Wang, Fu, & Sun, 2011).

2.2.3 Capacitive WPT

Two pairs of plates are used by electric field-coupled WPT systems, referred to as capacitive power transfer (CPT) systems, to form an analogous power transfer capacitor. Due to its specific operating concept and since a capacitor is formed from each conductor plate to the metallic surface (Theodoridis, 2012), the CPT can be used in applications that involve power transfer through metals. In addition, it has desirable characteristics such as lightweight and cost-effective couplers than couplers in WPT magnetically coupled systems; and the transfer of power is less vulnerable to misalignment than the electric field between the bends of the plates with the plate misalignment. However, the capacitance formed of parallel plates is normally very weak, which adversely affects the ability of couplers to transfer power (Sinha et al., 2017). High operating frequencies in the MHz range are needed to reduce the impedance of the power flow channel to solve this problem.

A stacked, four-layer system with LCL compensation is applied in (H. Zhang, Lu, Hofmann, Liu, & Mi, 2016) to pass 1.88 kW at a 150-mm air gap. A six-plate coupler is set up in (Sinha et al., 2017) for the reduction of electric field emissions. At a 150-mm air-gap, a 1.97-kW power transfer is achieved. A CPT device transferring 2.4 kW at a 150-mm air gap is described in (Lu, Zhang, Hofmann, & Mi, 2015). Using CPT, the power level of several kilowatts is usually achievable. However, the power density restriction is one of the key obstacles of a high-power CPT device. The dimension of the coupler should normally be much larger than the air gap to provide power efficiently for a wide air gap, which might not be feasible in certain situations. The reported power density is still as low as 11.88 kW/m^2 with dedicated coupler integration (H. Zhang et al., 2016). By pushing the frequency to 13.56 MHz, it is possible to raise the power density to 29.5 kW/m^2. In contrast, according to (Bosshard & Kolar, 2016b), the state-of-the-art surface power density of magnetically coupled wireless power transfer can reach up to 1.6 kW/dm^2 (160 kW/m^2), and higher power densities with polyphase couplers are possible. One viable approach is to improve the operating frequency further. However, ultra-fast switching frequency and high power capacity are hindered by current semiconductor system technology. Besides, high frequency on compensation networks may cause excessively high-voltage stress. It is anticipated that enhancing the switch technology of Gallium Nitride (GaN) and multiphase modular design would fuel the potential production of high-power CPT charging systems.

The large-scale implementation of WPT systems has become feasible through various research efforts and prototype demonstrations. In addition, the recent evolution of WPT systems poses a trend toward higher capacity, high power density and greater versatility and robustness, followed by the rapidly increasing demand for rapid charging infrastructure. Several 200 kW wireless charging systems have been initiated by Bombardier Primove for electric buses fitted with 60 kWh and 90 kWh battery packs. In very few minutes of dwelling time spent at the end station, electric buses are charged and the recorded AC to DC efficiency is more than 90%. A WPT system for electric trucks and vans with a power level of up to 200 kW has also been developed by Momentum Dynamics. In (Guidi, Suul, Jenset, & Sorfonn, 2017). A 1-MW WPT system for plug-in hybrid vessels is designed and tested to enable stable onshore charging in a damp environment.

2.2.4 Summary of Commercialized WTP systems

ETH researchers gave a detailed design consideration with regard to a 50 kW wireless charger based on Silicon Carbide (SiC) (Guidi et al., 2017). The efficiency, power density and leakage field were jointly optimized, accounting for the limitation of heat and scale. Together with the University of Auckland, Conductix tested a 60 kW charger on electric vehicles. In Southern California, WAVE designed and tested a 250-kW wireless charger for electric power fleets. This new DOE project envisages a 500 kW wireless drainage truck charging system. A series of products of up to 11 kW have been presented by WiTricity and prototypes supporting 25 kW power transfer are being further produced. The prototype of WiTtricity realized a complete SiC-based operation and showed a grid to battery efficiency of 91 percent to 93 percent . A full-power electronic prototype for a 22 kW bidirectional wireless charger was demonstrated by the Fraunhofer Institute in Germany. Due to a new controller configuration, the highest dc-dc efficiency reached more than 96 percent (Tritschler, Reichert, & Goeldi, 2014).

In order to comply with the International Commission on Non-Ionizing Radiation Protection (ICNIRP) leakage field emission guideline (Suzuki et al., 2017), Toshiba tested a 44 kW modularized WPT system for electric buses and evaluated its EMI efficiency. A 25 kW WPT system based on three parallel half-bridge cells is constructed in (Bojarski, Asa, Colak, & Czarkowski, 2017) and 95% dc-to-dc efficiency is achieved. Regarding the dynamic charging system, the Korean Advanced Research Institute (KAIST) has completed a series of large-scale railway transit and EV demonstrations in which various magnetic coupler structures are proposed to enhance compactness, EMC efficiency and roadway construction compatibility (Choi, Gu, Jeong, & Rim, 2015). The Korean Railroad Research Institute (KRRI) is developing a 1 MW prototype for high-speed trains with a test speed of up to 800 kW. A DWC system of 250 kW was built by Bombardier Primove for trams. A 25 m track was set up by the Integrated Infrastructure Solutions (INTIS) research team to measure the DWC output of 200 kW EVs. They also install a DWC at 30 kW for industrial movers. In (Tavakoli & Pantic, 2018), a 25 kW dynamic charging system was demonstrated by Utah State University that allowed 15 cm of horizontal misalignment while still delivering full power. In addition, the IK4-Ikerlan Research Center in Spain has also introduced a dynamic charging project of 50 kW (Villar, Garcia-Bediaga, Iruretagoyena, Arregi, & Estevez, 2018). Some commercial operations are mentioned in Table 2.1.

Table 2.1: Recent Commercial and Laboratory WPT Prototypes

Institution	Year	Power level	Power density (kW/dm2)	Efficiency (%)	Air gap (mm)
Conctix Wampfler AG	2002	120kw	N/A	90	40
The University of Auckland	2010	3kw	N/A -	85	180
Oak Ridge National Laboratory	2012	7.7 Kw	N/A	93 (Coil-Coil)	200
Korea Advanced Institute Of Science and Technology	2013	100kw	N/A	75	200
WiTricity	2013	3.7 kW	0.13	90	180
BOSCH	2015	7 kW	0.35	86 (Dc-DC)	160
Fraunhofer Institute for Solar Energy Systems (ISE)	2015	22 kW	N/A	97.4 (DC-DC)	130
ETH	2016	50 kW	1.6	95.84 (DC-DC)	160
Oak Ridge National Laboratory ORNL	2018	50 kW	1.95	95(DC-DC)	150
		120 kw	2.04	96.9 at 50kw	130

2.3 Basic theory of IPT system

The fundamentals of inductive wireless power transmission are similar to those of a transformer, with air acting as the core for coupling between primary and secondary coils. In this section, a simplified approach to model compensation networks has been made. To transmit the maximum amount of power with the least amount of reactive power supplied from the source, effective compensation is required. A simplified method for mathematical analysis focused on active and reactive power was stated by the authors in (S. Li & Mi, 2015). The maximum efficiency of the basic compensation network has been stated in various recent publications. Fig.2.1 shows the WPT system with a basic compensation network. The primary side is normally connected to a high-frequency full-bridge inverter and the receiver side is connected to a full-bridge diode to prove the DC output voltage for charging the battery. Semiconductor switches and diodes are not included in Fig.2.1 (b)to ease the study. The primary and secondary compensation networks may be connected in series, parallel, LCC, LCL and so on. Nevertheless, in this section, a simplified method has been discussed in more detail to show the basic characteristics of the WPT system. The efficiency of the WPT system for Fig.2.1(a) and (b) is stated in Eq. (2.1) and Eq. (2.2), respectively,

$$\eta_{\text{complete}} = \eta_{\text{p}}\eta_{\text{s}}\eta_{\text{cp}}\eta_{\text{cs}}\eta_{\text{inv}}\eta_{rec} \tag{2.1}$$

$$\eta_{\text{simplefied}} = \eta_{\text{p}}\eta_{\text{s}}\eta_{\text{cp}}\eta_{\text{cs}} \tag{2.2}$$

where ηcp is the efficiency of the compensation network, ηp is the primary coil efficiency, ηs is represent the secondary coil efficiency, and ηcs is the efficiency of the secondary side compensation network. The overall simplified efficiency when the losses in inverter and rectifier circuits are ignored is given by (Sohn et al., 2015).

$$\eta_{\text{simplefied}} = \frac{Re(Z_{m1})Re(Z_2)}{(\text{R}_{P1} + Re(Z_{m1}))(\text{R}_{P2} + Re(Z_2))} \tag{2.3}$$

where Z_{m1} is defined as

$$Z_{m1} = j\omega \mathrm{M}_{12} / (j\omega(L_2 - \mathrm{M}_{12}) + \mathrm{R}_{P2} + Z_2) \tag{2.4}$$

Z_2 is either series impedance Z_{2s} or parallel impedance Z_{2P} and is given by

$$Z_{2s} = R_L + \frac{1}{j\omega C_2} \qquad\qquad Z_{2p} = R_L / \frac{1}{j\omega C_2} \tag{2.5}$$

Substituting Eq. (2.3) and Eq. (2.4) in Eq. (2.5) and simplifying the equation gives the efficiency with secondary series compensation (η_S) and the efficiency of parallel compensation scheme (η_P) (Sohn et al., 2015)

$$\eta_S = \frac{(Q_1 Q_2 / Q_{LS}) k^2 \omega_n^2}{1 + (Q_1 Q_2 / Q_{LS}) k^2 \omega_n^2 + (Q_2 / Q_{LS})^2 (\omega_n - (1/\omega_n))^2} \tag{2.6}$$

$$\eta_P = \frac{k^2 \omega_n^2 Q_1 (b_1 \omega_n^4 + b_2 \omega_n^2 + b_3)}{(b_4 \omega_n^6 + b_5 \omega_n^4 + b_6 \omega_n^2 + b_7)(1 + (1/Q_2 Q_{LP}) + (Q_{LP} \omega_n^2 / Q_2)} \tag{2.7}$$

Where ω_n is the normalized angular frequency, $\omega 2$ is the secondary resonant angular frequency, Q_1 and Q_2 are the quality factors of coils and Q_{LP} and Q_{LS} are the load side quality factors. These terms are defined as follows:

$$\omega_n = \frac{\omega}{\omega_2}, \omega_2 = \frac{1}{\sqrt{L_2 C_2}}, Q_1 = \omega L_1 / \mathrm{R}_{P1}, Q_2 = \omega L_2 / \mathrm{R}_{P2}, Q_{LS} = \omega L_2 / \mathrm{R}_L,$$

$$Q_{LP} = \mathrm{R}_L / \omega L_2, b_1 = Q_{LP}{}^4 / Q_2, b_2 = Q_{LP}{}^2 (Q_{LP} + 2/Q_2), b_3 = Q_{LP} + 1/Q_2$$

$$b_4 = Q_{LP}{}^4 (1 + \frac{k^2 Q_1}{Q_2}), b_5 = k^2 Q_1 b_2 + Q_{LP}{}^2 (2 - 2Q_{LP}{}^2 + Q_{LP}{}^2 / Q_2{}^2)$$

$$b_6 = k^2 Q_1 b_3 + 2Q_{LP}{}^2 b_3 / Q_2 + (1 - Q_{LP}{}^2)^2, b_7 = (Q_{LP} + 1/Q_2)^2$$

Analysis of Eq. (2.6) and Eq. (2.7) clearly shows that in both Series- Series (S-S) and Series-Parallel compensation network, the quality factor of the coils are playing a critical role in the system efficiency of the inductive WPT system. A similar conclusion can be made for different compensation designs(Feng et al., 2020). Therefore, it is crucial to optimize compensation network and coil design simultaneously to achieve high-efficiency WPT.

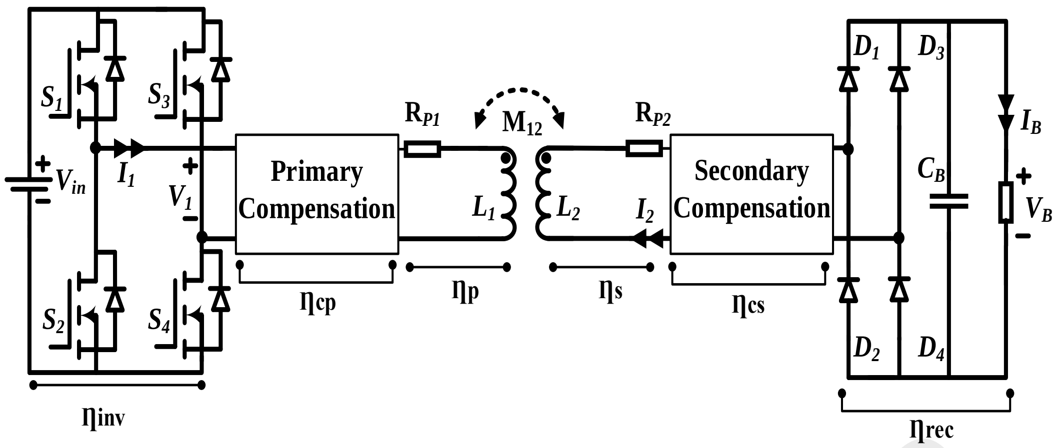

(a)

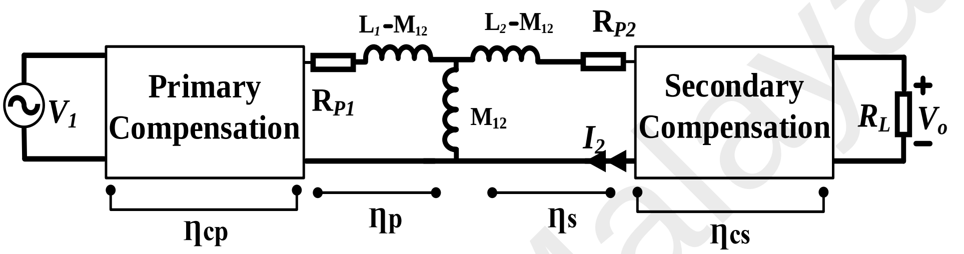

(b)

Figure 2.1: (a) General WPT system with compensation (b) Simplefied WPT system with T equivalent circuit

2.4 Magnetic Couplers

Transmitter (Tx) and receiver (Rx) pads transfer power through an air medium in most WPT systems. These pads are generally referred to as magnetic couplers in the literature and play a major role in the entire WPT operation (Budhia, Covic, & Boys, 2011). Many researches have been done on pad structures to boost the coefficient of device coupling *k*, quality factor *Q* of pads, tolerance of misalignment, coil-to-coil efficiency and reduction in stray fields. Litz wires are used to construct the magnetic couplers, which helps to reduce the loss of skin effects and increases the mutual inductance by flux directing ferrite cores and the leakage field is minimized by aluminum shielding. In the WPT system, for EV applications, single-sided coils are more popular than double-sided coils. Single-sided coils are usually referred to flux direction between the transmitter coil and receiver coil, where only one direction of flux is generated by the high-frequency current that passes through the coils. Single-sided couplers are generally be classified into a) single-coil pads, such as Circular Pads (CP), Rectangular Pads (RP) (Budhia et al., 2011) (Ramezani & Narimani, 2021), or Double D (DD) pads (Budhia et al., 2013), and b) multi-coil pads like Double D-Quadrature (DDQ) (S. Y. Jeong, Choi, Sonapreetha, & Rim, 2015), Bi-Polar (BP) pads (Zaheer, Covic, & Kacprzak, 2014), or Tri-Polar (TP) pads (S. Kim et al., 2017).

2.4.1 Circular coil

A circular pad (Patil et al., 2018) , as shown in Fig 2.2, is the most widely used coil structure (a). In the literature, circular coils are well stated and optimized (Covic & Boys, 2013; Long, Miller, Daga, Schrafel, & Wolgemuth, 2016). Optimization and guidance for the design of a circular coil are stated in (Bandyopadhyay, Prasanth, Bauer, & Ferreira, 2016; Bosshard et al., 2015)with regard to efficiency and area-related power density. Authors in (Bandyopadhyay et al., 2016)demonstrated DC-DC performance of 96.5% with a 210 mm coil diameter and 52 mm air gap by using η -Pareto optimization. When the vertical distance between the coils is 25% of the diameter, the circular coil coupling coefficient is in the order of 0.2. If the distance between the coils is 150-200 mm, the diameter of the coils should be 600-800 mm to maintain the coupling coefficient within the range 0.15-0.2 (Budhia et al., 2013). It was stated in (Suzuki et al., 2017) that WPT coils in the Litz wire or similar cable should operate at current densities of less than $3A/mm^2$ to $5A/mm^2$ to achieve reasonable thermal efficiency. A very good evaluation of WPT for automotive applications was provided by the authors in (Bosshard & Kolar, 2016a), whcih provided excellent care for circular pad sizing and key performance factors for EV chargers. Due to the single-sided magnetic field that enters and leaves the coil from the front of the coil, the circular coil and its near variants are widely used in WPT, as shown in Fig 2.2. The magnetic field is single-sided and above the ferrite and the later channels, much of the flux under the coil and away from rebars and pipes in floor concrete

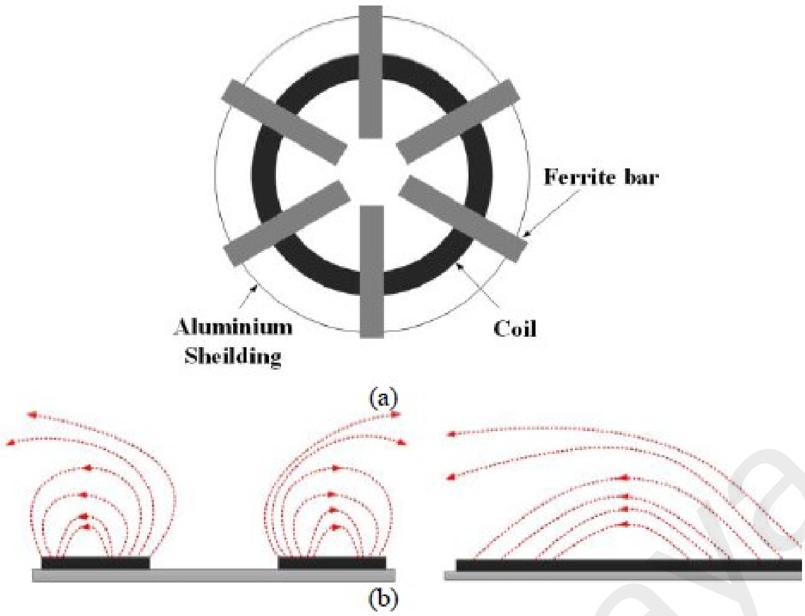

Figure 2.2 : Circular pad and its flux lines (Patil, McDonough, Miller, Fahimi, & Balsara, 2018)

is the fountain field shaped like the coil. The single-sided design of the pattern of flux helps to reduce the amount of leakage flux.

2.4.2 DD Coil

In (Budhia et al., 2013) suggested a single-sided polarized flux coupler that incorporates the benefit of both the nature of the flux pipe and the circular pad, as shown in Fig 2.3. As the coils are magnetically linked in series, the middle portion of the DD coil is identical to the flux pipe (Budhia et al., 2010). The ferrite is placed under the coils; this makes it possible to put aluminum shielding under the ferrite without quality factor loss. The key characteristics of the DD coil are single-sided flux paths, the height of the flux path that is equal to half the length of the pad, resulting in a higher coupling coefficient, lower aluminum shielding losses, and low leakage flux from the back of the coil. Moreover, the quality factor Q of the system is improved (Covic, Kissin, Kacprzak, Clausen, & Hao, 2011).

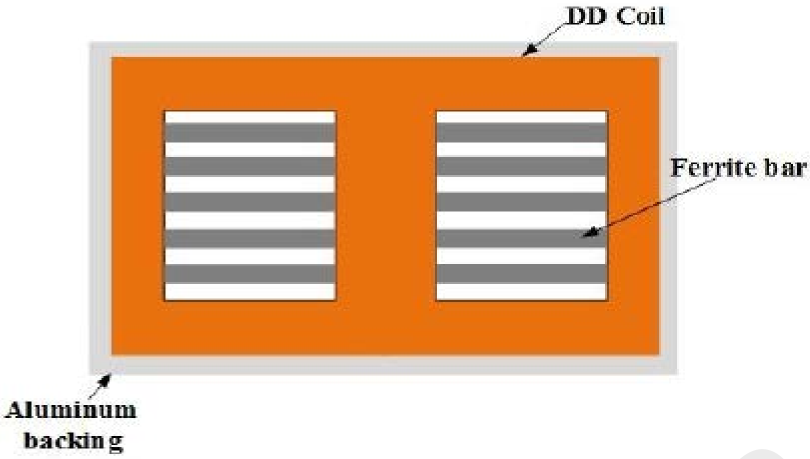

Figure 2.3: DD-Coil Structure (Budhia, Boys, Covic, & Huang, 2013)

2.4.3 DDQ Coil

By introducing the quadrature coil, the DDQ coil is derived from the DD coil, as shown in Fig 2.4. The location of the coil is at the center of the DD coil. The coils are oriented so that the *d*-axis flux is captured by DD coils and the *q*-axis flux is captured by Q coils. Therefore, to a large degree, this coil arrangement compensates the misalignment. However, with respect to the circular pad or the square coils, the size of the coils increases by approximately three times (Budhia et al., 2013).

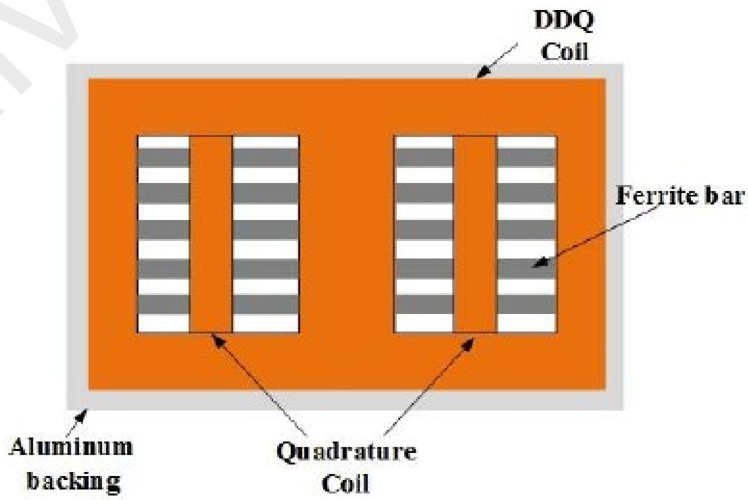

Figure 2.4 : DDQ Coil Structure (Budhia et al., 2013)

2.4.4 Bipolar Pad

As shown in Fig 2.5, the bipolar pad (BP) (Patil et al., 2018) is a multi-coil coupler with two coils mounted on a ferrite bar with an overlap. BP consists of two similar and partially overlapped coils. The bipolar pad has a high tolerance for misalignment and a high coupling coefficient, comparable to the DDQ pad. Compared to DDQ pad, the key benefit of BP is that it needs 25 to 30 percent less copper.

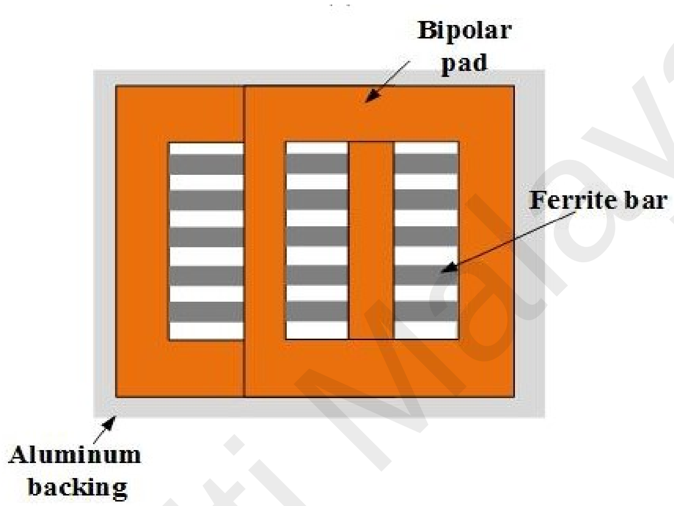

Figure 2.5 : Bipolar Coil Structure (Patil et al., 2018)

2.4.5 Tripolar Pad

The Tripolar Pad (TPP) is a three mutually decoupled coils coupler arranged in such a way as shown in Fig 2.6 (S. Kim et al., 2017). High rotational misalignment tolerance of a non-polarized pad is allowed by this form of assembly. To attain the highest coupling factor, the three mutually decoupled coils are driven independently. Authors have shown an improvement in the effective coefficient of bipolar and circular pad coupling as a secondary coil. This was done by regulating the voltage magnitude and phase of the coil currents of the transmitter. The apparent power demand for an airgap of 150 mm is reduced by 45 percent compared to the circular pad (S. Kim et al., 2017). The stated magnetic leakage field is also lower than that described in ICNIRP. Three separate inverters are needed to power three mutually decoupled coils, which increases the cost and complexity.

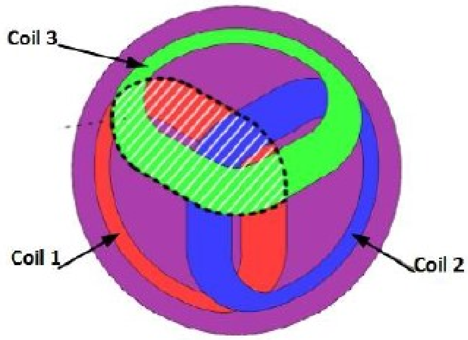

Figure 2.6: Tripolar Coil Structure (S. Kim, Covic, & Boys, 2017)

2.4.6 Flux pipe

Different coil shapes, including the rectangular ferrite bar with a coil wound along its length shown in Fig 2.7 (Budhia et al., 2010), are suggested in the literature to enhance the coupling. For horizontal misalignment, this solenoidal field design has a strong tolerance, plus the fact that it increases the ferrite flux direction to locate it at the end of the coils. The advantage of the design of the flux pipe is that the height of the simple flux path is half the length of the receiver pad. Moreover, the tolerance of horizontal (lateral) misalignment is high and the coupling coefficient is equivalent to that of a circular pad. The drawback of this coil design is that it is solenoidal, hence its proximity to one side of the coil winding would result in interception of flux and thus reduce the quality factor

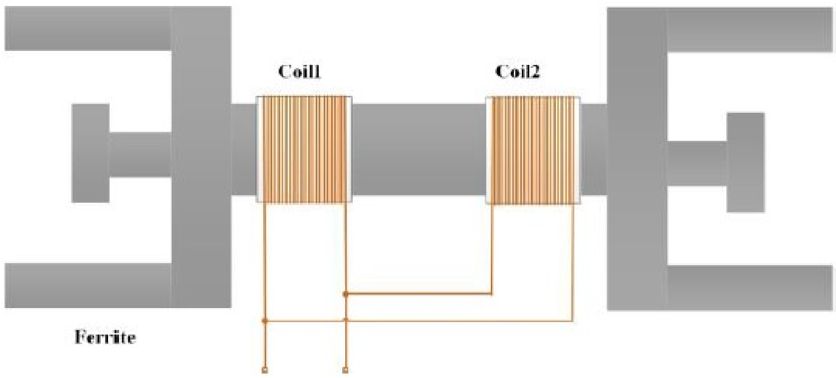

Figure 2.7 : Flux pipe Coils (Budhia, Covic, & Boys, 2010)

when aluminum shielding is used. The efficiency of EV charging is reduced by this loss of quality factor.

2.4.7 Intermediate coil

Intermediate coils can be used to act as repeaters and boost the power transfer between the source and the load (Seungyoung & Joungho, 2011) in order to increase the power transfer distance. In the literature (D. Ahn & Hong, 2013; J. Kim, Son, Kim, & Park, 2011; Seungyoung & Joungho, 2011), design procedures are explored to optimize their benefits. In the same plane as the primary-side coil, which is also called a coplanar coil, the intermediate coil can be located. Coplanar coils have been shown to improve the coefficient of device coupling, efficiency, and tolerance for misalignment (Kamineni, Covic, & Boys, 2015).

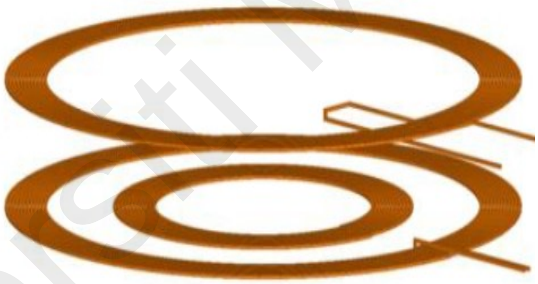

Figure 2.8 : Intermediate Three Coil Structure (Seungyoung & Joungho, 2011)

2.5 Comparison between different coil design

Under some conditions, several works have compared various geometries. Many researchers have considered coupling factor *k* as the criterion for comparison to compare various designs (Bosshard, Mühlethaler, Kolar, & Stevanović, 2013; Ongayo & Hanif, 2015). In some designs, kQ is used as the criteria (Bosshard, Iruretagoyena, & Kolar, 2016) and in some other studies uncompensated power Psu has been used (Zaheer, Kacprzak, & Covic, 2012). Different results were drawn depending on the test conditions. In (Bosshard et al., 2013), for instance, the authors researched three forms, including a

Square Pad (SP), an RP and a CP, and find that the surface area of the coupler is more significant than the shape itself. Although it is seen in (Liu & Habetler, 2015) that SP performs better than CP and DDP and in (Luo & Wei, 2018), it is concluded that SP is a better choice than CP for WPT. RP compared to DDP is selected in (Bosshard et al., 2016) and it is shown in (Budhia et al., 2013) that DDP is preferred to CP. Compared to CP, TP pad output is evaluated in (S. Kim, Covic, & Boys, 2018) and the coupling factor and leakage magnetic field of TP pads are shown to be better than that of CPs. The magnetic couplers should be optimized under the same constraints to ensure a fair comparison between different structures (Bandyopadhyay et al., 2019). However, majority of the aforementioned reports lack certain requirements.

Four major topologies including 1) CP, 2) RP, 3) DD-DD, and 4) DD-DDQ are compared in (Bandyopadhyay et al., 2019). To maximize the efficiency, volumetric power density, gravimetric power density and misalignment tolerance, each geometry is optimized. Some of the key results of the comparison are as follows: 1) for the same gravimetric power density, CP shows the best efficiency and coupling factor, 2) CP uses the most ferrite and the least copper for the same value, 3) For the same power density, CP and RP outperform the polarized pads, CP in comparison to RP has better power density, however, in some applications such DWPT or in multi receivers application RP and SP are preferred over CP (Liu & Habetler, 2015), 4) polarized coils demonstrate better output in particular misaligned directions, and 5) relative to the polarized pads, the CP and RP have lower stray fields. Since double-sided flux coils tend to create a higher leakage field, as in flux pipe, and have higher eddy current loss, which are not suitable for EV applications, majority of the reported coils in Table 2.2 are those that generate single-sided flux.

Table 2.2: Conversion of Input Voltage source to Constant Current

Coil Structure	Field Distribution	Flux direction	Misalignment tolerance	Null Zone
Circular	E-type	Single-sided	Weak	At 40 % of the pad diameter
Rectangular	E-type	Single-sided	Weak	At 50 % of the pad width
DD	C-type	Single-sided	Moderate	At 34% of the pad length
DD-Q	C/E-type	Single-sided	Moderate	At 77 % of the pad length
Bipolar	C/E-type	Single-sided	Moderate	At 77 % of the pad length
Tripolar	C/E-type	Single-sided	Very good	N/A
Flux pipe	C-type	Double-sided	Moderate	An elliptical null all around. Not any point of null

2.6 IPT Compensation Topologies

The self-resonant frequencies of the new WPT coil models are far above the operating frequency of the system, which involves the attachment of additional compensation capacitors on both the primary and secondary sides. The compensation is levied only in the early stages of the design of an IPT scheme (Ghahary & Cho, 1992). However, double-sided compensation network has long altered this design because conventional single-sided compensation is not able to offer enough degree of freedom to meet the requirements of the current architecture of the WPT system. Generally, in developing a compensation topology, there are four priorities that can be stated as follows.

1) Minimizing reactive power and maximizing power transfer capability: The basic necessity for a compensation capacitor is to resonate with the transmitter and/or receiver coil to provide the coils with reactive power and to produce sufficient magnetic fields. Moreover, the total input impedance on the primary side is usually designed to minimize the Volt Ampere rating of the power supply. However, it is advisable to keep a small portion of reactive power to achieve soft-switching during the charging process. On the secondary side, the inductance of the receiver coil will cancel out by the additional compensation to optimize the transfer capability.
2) Constant output properties against a wide range of load and coupling coefficient variation: Coupling variation will often occur due to the existence of vertical or/and horizontal misalignment that is hardly inevitable. For instance, when the patient is breathing or in dynamic WPT applications, the net distance between the main coils constantly changes. Moreover, depending on the different battery profiles, it is required to achieve constant current (CC) and/or constant voltage (CV) under a wide variation of load during the charging process. Therefore, a resonant network compensation requires to reduce the output fluctuation and contribute the system to be less sensitive to the load and coupling coefficient variation, which eventually simplifies the control part as well.
3) Wide range of soft switching operation: In typical WPT applications, half bring or full-bridge converters are used to convert the DC to high-frequency AC voltage. In the latest WPT works, MOSFETs are the most widely used switching devices in designing the inverters. It is necessary to either run the converter above the resonant frequency or de-tune the compensation network to minimize the losses in the Mosfets by making the input current slightly lag the input voltage to benefit the converter from turn-on zero voltage switching (ZVS). Achieving ZVS

contributes to the improvement of the overall system efficiency as well.

4) Bifurcation tolerance, cost, voltage and current stress: The bifurcation phenomenon should be avoided to ensure system stability. This phenomenon refers to the condition where multiple frequencies can realize zero phase angle (ZPA) across the output of the inverter. Load condition and the compensation topologies are the main factors in deciding the number of frequency points to realize ZPA. Another important consideration in designing a compensation network is to reduce the current and voltage stress while maintaining a high power transfer. Moreover, some other factors such as the cost of the system and fault protection, are also equally important depending on the application needs.

Over the past three decades, multiple different compensation topologies have been proposed to fulfill at least two of the mentioned four objectives. Conventional compensation methods include four schemes with a single compensation element on their primary and secondary sides, known as Series-Series (SS), Series-Parallel (SP), Parallel-Series (PS), and Parallel-Parallel (PP). All of the four basic compensations can be design in a way to achieve whether CC or CV characteristics. To illustrate different solutions and general methods for each compensation to achieve load-independent properties, several typical compensation topologies can be summarized in Table 2.3 to 2.6. These tables are from the study (W. Zhang & Mi, 2016), which can simplify the design procedure of the IPT modern compensations.

Table 2.3: Conversion of Input Voltage source to Constant Current (W. Zhang & Mi, 2016)

V-C-1	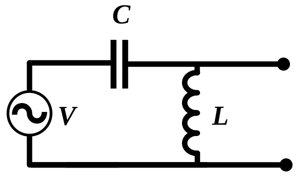	$\omega = \frac{1}{\sqrt{LC}}$
V-C-2	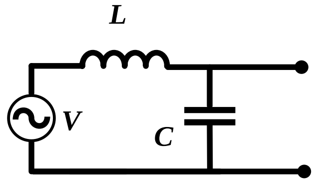	$\omega = \frac{1}{\sqrt{LC}}$

Table 2.4: Conversion of Input Voltage source to Constant Current (W. Zhang & Mi, 2016)

C-V-1	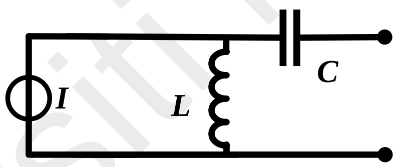	$\omega = \frac{1}{\sqrt{LC}}$
C-V-2	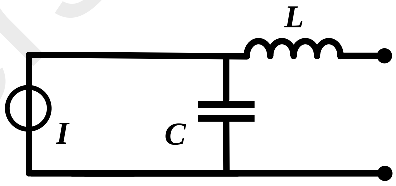	$\omega = \frac{1}{\sqrt{LC}}$

Table 2.5: Conversion of Input Voltage source to Constant Current (W. Zhang & Mi, 2016)

V-V-1	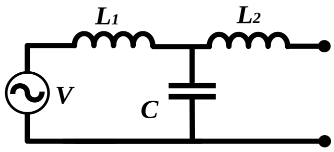	$\omega=\sqrt{\frac{1}{L_1C}+\frac{1}{L_2C}}$
V-V-2	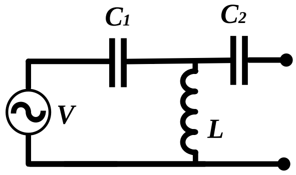	$\omega=\frac{1}{\sqrt{LC_1+LC_2}}$
V-V-3	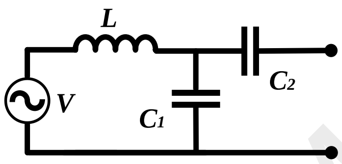	$\omega=\frac{1}{\sqrt{LC_1+LC_2}}$
V-V-4	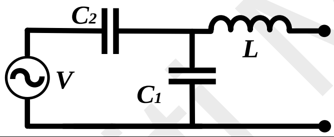	$\omega=\frac{1}{\sqrt{LC_1+LC_2}}$
V-V-5	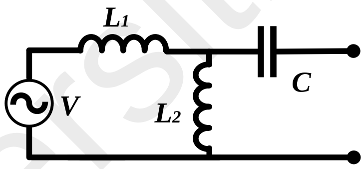	$\omega=\sqrt{\frac{1}{L_1C}+\frac{1}{L_2C}}$
V-V-6	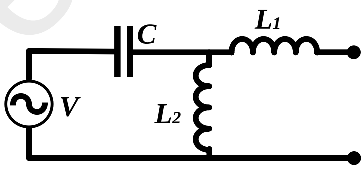	$\omega=\sqrt{\frac{1}{L_1C}+\frac{1}{L_2C}}$
V-V-7	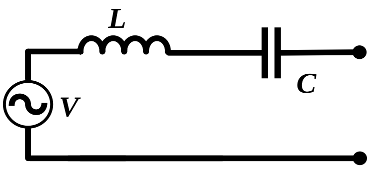	$\omega=\frac{1}{\sqrt{LC}}$
V-V-7	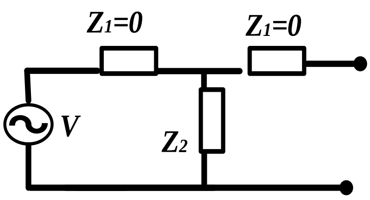	----

Table 2.6: Conversion of Input Current source to Constant Current (W. Zhang & Mi, 2016)

C-C-1	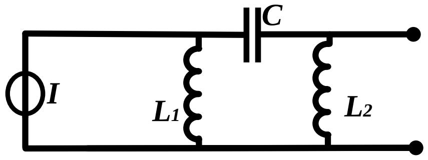	$\omega = \sqrt{\frac{1}{L_1C} + \frac{1}{L_2C}}$
C-C-2	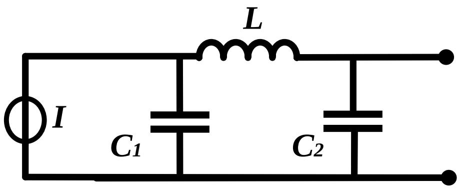	$\omega = \frac{1}{\sqrt{LC_1 + LC_2}}$
C-C-3	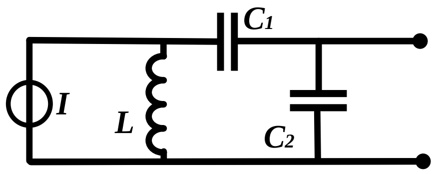	$\omega = \frac{1}{\sqrt{LC_1 + LC_2}}$
C-C-4	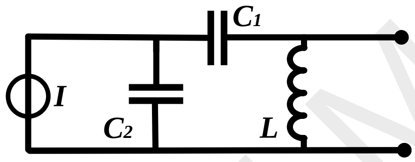	$\omega = \frac{1}{\sqrt{LC_1 + LC_2}}$
C-C-5	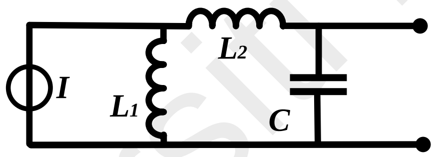	$\omega = \sqrt{\frac{1}{L_1C} + \frac{1}{L_2C}}$
C-C-6	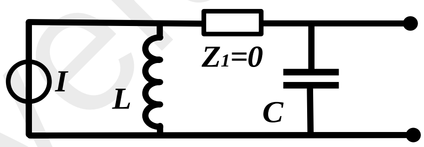	$\omega = \frac{1}{\sqrt{LC}}$
C-C-7	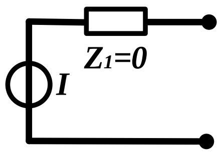	---

2.6.1 S-S Compensation

Series-Series (S/S) compensation and its equivalent Network is illustrated in Fig 2.9. S-S compensation can be compensated to have a constant output current while achieving ZPA (Chwei-Sen, Stielau, & Covic, 2005). According to (W. Zhang & Mi, 2016), the components in-between node a and b, which are placed in the block diagram of 1 can be regarded as V-C-2 in Table 2.3, which indicate that if the operating frequency of the first block diagram is design according to Eq. (2.9), it is possible to achieve Constant output current across the node b. Moreover, the secondary block diagram which is placed in between node b and c can be regarded as C-C-7. Therefore, constant output current independent of load can be achieved at node c according to Table 2.6.

Note that since the components in block 2 are all in series, a constant current can be achieved regardless of the value of ZL_1. Therefore, ZL_1 has no major influence on CC characteristics, but it can change the input phase angle and benefit the system to achieve ZPA or ZVs. This eventually leads to improve the system efficiency and ease the control circuit of the WPT system. ZL_1 can be defined as

$$Z_{L_1} = j\omega L_{LS} + \frac{1}{j\omega C_S} \tag{2.8}$$

$$\omega = \frac{1}{\sqrt{(L_{LP} + L_M)C_P}} = \frac{1}{\sqrt{L_P C_P}} \tag{2.9}$$

The S-S topology can also be designed to have a CV mode (W. Zhang & Mi, 2016).

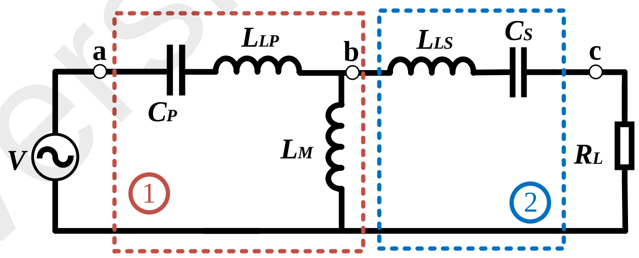

Figure 2.9 : CC conditions for S-S compensation

However, unlike the CC mode, the operating frequency to achieve CV in S-S compensation is not unique. To achieve CV for the S-S topology, Fig 2.10 has been plotted. It can be seen from the block diagram of 1 in Fig. 2.10, the components between node a and c can be regarded as V-V-6 or V-V-8 depending on the operating frequency. This indicates that both C_P and C_S need to be designed according to Table 2.6 in the CV operation of S-S topology. Therefore, unlike the CC mode of S-S system, capacitor C_S

can not be designed freely to control the input phase angle of the system, which makes achieving ZPA and CV simultaneously hardly possible. This eventually causes the maximum efficiency of CV mode to be lower than CC mode in S-S system. Another disadvantage of this design is that C_P and C_S both need to be designed to compensate for the leakage inductance of the main coils. Since mutual inductance and leakage inductance of the transmitter and receiver coil can be changed in the misalignment position, the system may lose its CV properties as well when the main coils are not fully aligned.

In (Chwei-Sen et al., 2005), the relationship between the load condition and the

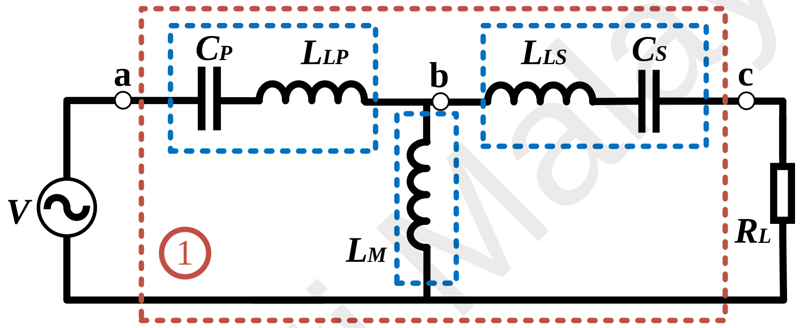

Figure 2.10 : CV conditions for S-S compensation

frequency-splitting phenomenon of basic compensation based on the condition to achieve ZPA has been discussed. Moreover, the reflected capacitor on the primary side to mitigate the system reactive power also discussed. In Order to obtain a constant current output source and to ensure the capacitor's compensation are independent of leakage inductances, the work in (W. Zhang, Wong, Tse, & Chen, 2015) compensates the primary and secondary capacitors with the self-resonant frequency of the mail coils. Similarly, the leakage inductance of a load-independent constant output voltage source can be compensated for SS topology. In general, there are several “specific” operating frequencies for SS compensation to achieve a gain with CC or CV Output characteristics and by operating the system on different “specific” frequencies, it is possible to switch between CC and CV mode to ease the control circuitry of the EV battery. (W. Zhang, Wong, Tse, & Chen, 2014a).

2.6.2 S-P Compensation

S-P compensation is usually designed to have constant voltage output. From Fig 2.11 (a), if $ZL1(\omega)<0$, the S-P compensation topology can be regarded as the combination of the resonant network V-V-6 in block ① and V-V-8 in block ②. A constant-voltage output can be achieved when operating at

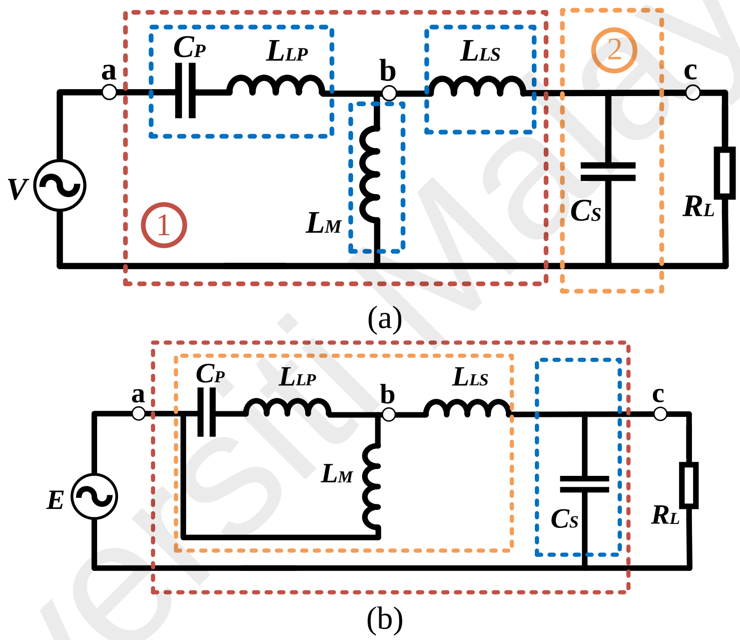

Figure 2.11: (a) CV and (b) CC conditions for S-P compensation

$$\omega = \sqrt{\frac{1}{C_P\left(L_{LP} + \frac{L_M L_{LS}}{L_M + L_{LS}}\right)}} \tag{2.10}$$

S-P compensation can also realize constant-current output. By further manipulation using Thévenin's equivalent circuit, S/P compensation topology can be reorganized as Fig. 11 (b), which illustrates the constant-current output condition. E is defined as

$$E = V \frac{j\omega L_M}{j\omega L_{LP} + \frac{1}{j\omega C_P}} \tag{2.11}$$

If the operating frequency is selected to let the impedance in the orange dotted block performs as an equivalent inductor, which can resonate with C_S, it can be regarded as the resonant circuit V-C-1 in Table 2.3, and the output current is constant.

2.6.3 P-S Compensation

A paralleled capacitor cannot be used as compensation on the main side in WPT applications since the voltage supply is most widely used to operate high-power converters. Therefore, PS Compensation requires current source input (as shown in Fig 2.12) to avoid any instantaneous change in the voltage (W. Zhang, Wong, Tse, & Chen, 2014b). To solve this problem, an inductor is added to create LCL resonant tank. This configuration is called the P–S compensating technique and is the focus of some researchers. PS circuit, similar to other basic compensation, is capable of achieving constant output voltage or current by compensating its capacitor according to Tables 2.4 to 2.6. The transferred impedance in P–S and S–S configuration is the same. The main advantages are high efficiency and high PF at relatively low mutual inductance and a relatively large range of variation of load and mutual inductance (Choi et al., 2014; S. Kim, Park, Kim, Kim, & Ahn, 2014). The PF in P-S is not at unity under low mutual inductance according to (Patil et al., 2018).

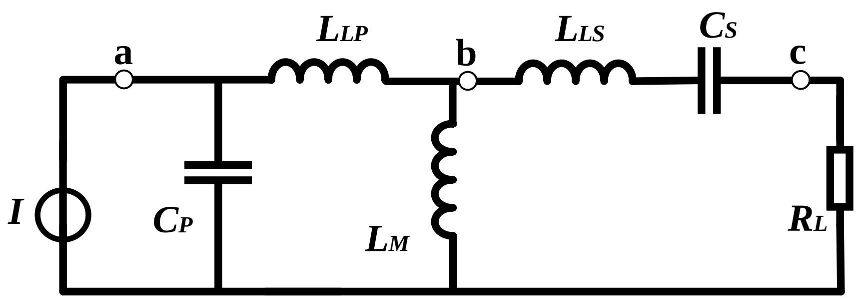

Figure 2.12 : P-S compensation

2.6.4 P-P Compensation

In a P–P compensation, the transferred impedance to the primary side is the same as in S–P compensation. This configuration suffers from the low PF, a high load voltage of the parallel secondary and large current source requirements of the parallel primary (S. Ahn et al., 2010). Moreover, This compensation is not widely studied because of it has more disadvantages compared to the other basic compensations (Chwei-Sen, Covic, & Stielau, 2001). (Choi et al., 2014) reported a detailed optimal sizing of 200-kW IPT for different compensation networks. Table 2.7 summarizes the performance comparison for basic compensation networks. S–S compensation requires the least amount of copper among all. This is a direct saving in cost for the system. S–S and S–P compensations are suitable for high power from an economic point of view. P–S or P–P compensations are typically used for high-power current source is driven cables that run over a long distance.

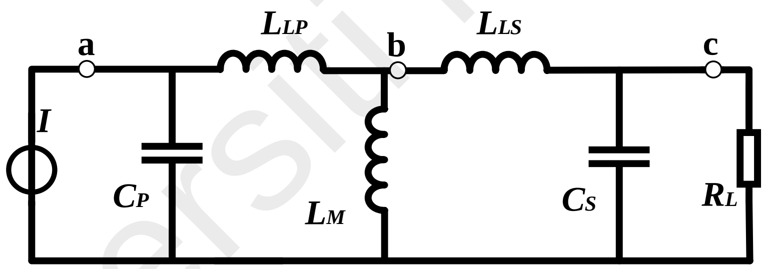

Figure 2.13 : P-P compensation

Table 2.7: Comparison of four basic compensation network

	S-S	S-P	P-S	P-P
Dependency	Independent of R_L and k	C_S is Dependent on k	C_P is Dependent on k	Both C_P and C_S are Dependent on k
voltage rating	Lowest voltage requires	Low voltage requires	Higher voltage compared to S-S and S-P	Higher voltage compared to S-S and S-P

2.6.5 Analysis and Comparison between modern and basic compensations

As discussed in the previous section, compensation can be designed to make the output voltage or current to be independent from load changes. Therefore, the impact of load variation is removed in all of those compensation systems, leaving the controller to comply only with coupling variation. However, since some load-independent single-element compensations rely on parameters like leakage inductance that are strongly dependent on coil location, the constant output characteristic suffers when the coupling factor starts to drift. According to (Hou et al., 2015), the voltage gain of SS and SP compensations at a given frequency is proportional to the coupling coefficient, causing the system to have a low tolerance to coupling variation. (W. Zhang et al., 2014a) optimizes the impedance of an SS-type topology running at a fixed frequency to achieve load-independent voltage gain. The frequency is set to be as similar to the resonant frequency as possible, lowering the system's reactive power. However, this approach necessitates a trade-off between reactive power and output voltage stabilization and it fails to address the relationship between output voltage gain, reactive power and the varying coupling factor profoundly. Compensations of multiple elements

To address these key challenges of single-element compensations, using series-parallel hybrid compensation with various elements is an effective solution. Since the output voltage is fully independent of load, LCL compensation is widely used in some applications. Besides, irrespective of the load or coupling state, the resonant network's input port will gain a unity power factor (Esteban, Sid-Ahmed, & Kar, 2015). By connecting a capacitor to the coil branch, another improved LCC compensation is developed, which retains all of the benefits of an LCL compensation. Furthermore, the voltage gain is improved since the extra capacitor partially cancels the coil's leakage inductance (Pantic, Bai, & Lukic, 2011). In contrast to the secondary side series compensation shown in Fig 2.14, the parallel compensation of the secondary side would also adjust the output source characteristics (W. Zhang & Mi, 2016). According to a previous study, the LCL-P compensation cascaded by a boost converter for EV charging is widely used (Zaheer, Neath, Beh, & Covic, 2017). In this case, the LCL-P compensation is considered as a current source to interface the boost inductor.

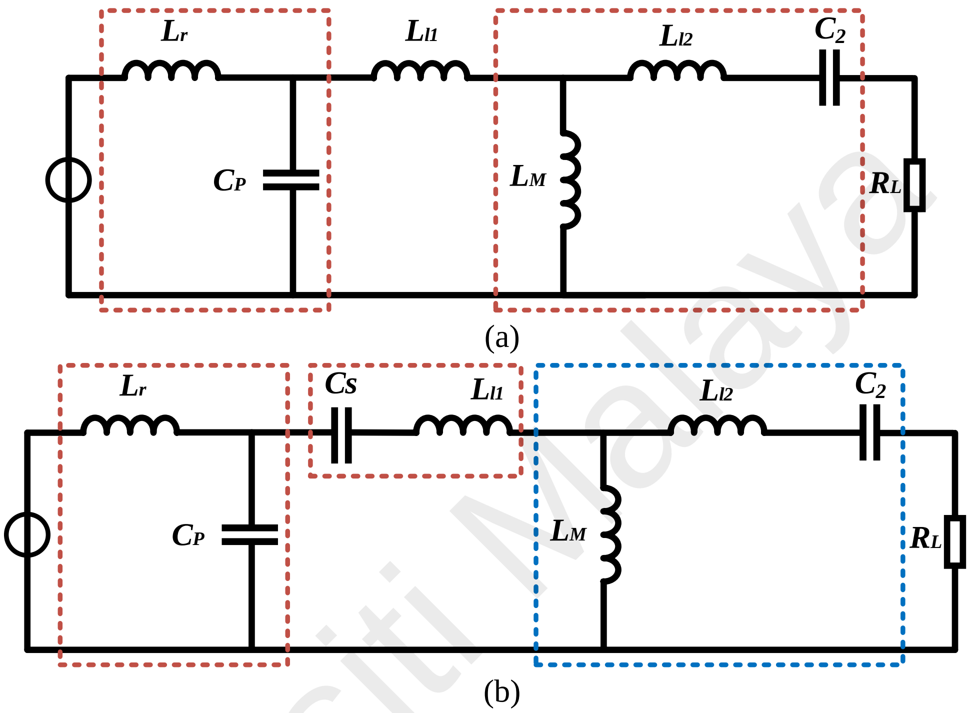

Figure 2.14 : CC and CV condition for LCC-S compensation

The T-type compensation topology is further extended to the secondary side (Feng et al., 2020), as shown in Fig. 2.15. To obtain unity power factor for the primary and secondary ports, the LCL compensation structure is used as the starting point and this characteristic has strong parameter flexibility. A better secondary LCL compensation is suggested in (Keeling, Covic, & Boys, 2010). The series capacitor in the secondary inductor section tunes with the corresponding internal inductor from the rectified load to ensure unity power factor and this improves the LCC compensation as well. To achieve a constant current output, a work in (S. Li et al., 2015) also extended LCC compensation to both sides. Furthermore, the resonant inductors are also inserted into the main coils that used a planar coil to improve the compensation network's compactness (W. Li et al., 2015), (Kan, Lu, Nguyen, Mercier, & Mi, 2018). Despite the benefits of load-independent constant voltage/current performance characteristics and low reactive power and coupling conditions, output sensitivity to the coupling factor is still considered a key challenge in compensation topologies.

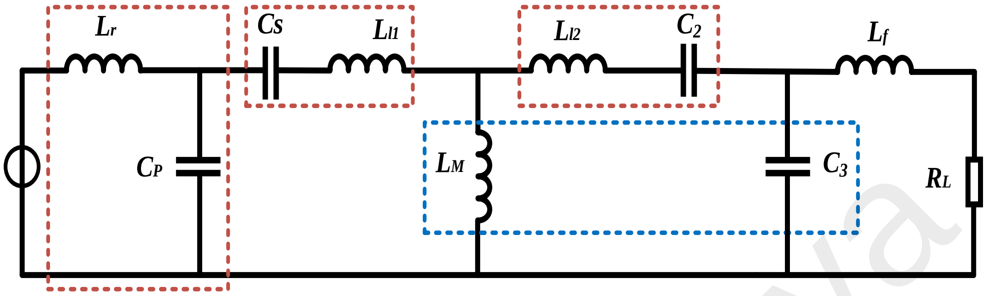

Figure 2.15: Double sided LCC compensation (Feng, Tavakoli, Onar, & Pantic, 2020)

In (Hou et al., 2015), the concept of SS and SP is combined and creates a S/SP type compensation topology, as shown in Fig 2.16, to enhance the robustness of these compensations to coupling variation. The S/SP type achieves complete leakage and magnetizing inductance compensation, leading to low reactive strength. As shown in Fig. 2.16, stable voltage gain is also achieved for a particular load and coupling factor set. The disadvantage is that the reactive power starts to increase as the coupling factor decreases, suggesting an insufficient decoupling with the coupling factor.

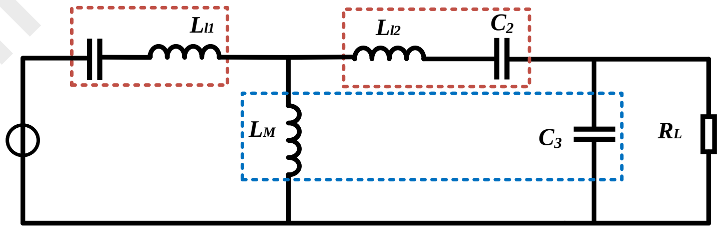

Figure 2.16 : S-SP compensation Network (Hou, Chen, Wong, Tse, & Ruan, 2015)

A basic concept for generating a position-tolerant compensation circuit in primary-side is discussed in (J. Zhao et al., 2016). Figure 2.17 depicts a progression in the number of compensation components, with one-element (Feng et al., 2018), two-elements (L-type) (Lu, Hofmann, Deng, & Mi, 2015), and three-elements (T-type) (Feng et al., 2016)compensations being proposed in this order. The characteristics of these topologies are said to be capable of keeping power transfer within 80% of its nominal value over a large coupling factor variance (from *k*min to 2*k*min). Because of it's high degree of freedom, design specifications such as coupling variance tolerance, full range ZVS, and reactive power reduction can all be met at the same time within a given coupling range. To achieve a more reliable performance, hybrid compensations incorporating various types of networks have recently been proposed. The power transfer characteristics of LCC and SS compensations are formulated to compensate each other, as shown in Fig. 2.18 in (L. Zhao, Thrimawithana, & Madawala, 2017). As compared to the single position-tolerant compensation, the resultant power transfer stability is increased. Furthermore, in (Lu, Zhang, Hofmann, Su, & Mi, 2018), the resonant inductors of traditional double-sided LCC compensation are designed as planar auxiliary coils to participate in the power transfer process, which is referred to as dual-coupled compensation. Due to the complementary properties of both compensation and main winding flux paths, the power transfer characteristics is further enhanced.

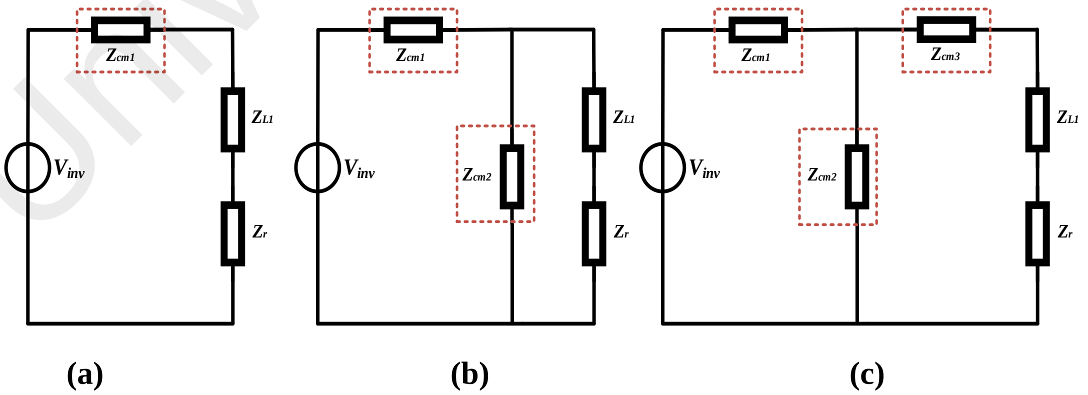

Figure 2.17 : Position -tolerant compensations: (a) One-element (b) Two elements (c) Three elements (Feng et al., 2016)

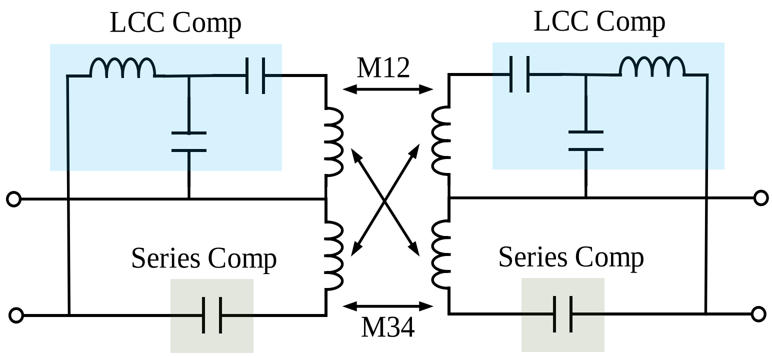

Figure 2.18: Hybrid compensation paralleling LCC and SS compensations in one resonant tank (L. Zhao et al., 2017)

2.7 CPT Compensation

There is typically a larger number of components in a CPT compensation network. In asymmetric structure, a standard configuration requires two pairs of coupling plates to create two identical capacitors in the circuit. Therefore, conventional compensation is also symmetrically constructed. In (Theodoridis, 2012), on both sides of the coupling plates, LCL compensation is applied. The voltage on the coupling plates is boosted through the resonance of inductors and capacitors to allow for high-power transfer. However, the inductor necessary to resonate with a capacitance of several pF is extremely big. Another difficulty is the development of such an inductor operating in the MHz range. In (Lu, Zhang, et al., 2015), the LCLC compensation parallels the external shunt capacitors to the lower series inductance coupling capacitors, with a total of eight external components applied to the device in this case. Under an air gap of 150 mm, a 2.4 kW power transfer is achieved. In (Lu, Zhang, et al., 2015), where an LC resonance is used to replace the LCLC, at the expense of a reduced power level, an attempt to simplify compensation is recorded.

A work in (Lu, Zhang, & Mi, 2018) suggested a two-plate CPT system that uses the vehicle frame and ground plane as the other two plates to further decrease the system complexity. Current CPT compensation focuses largely on improving the ability to move power and reducing the complexity of the hardware. In magnetically coupled WPT systems, these design goals have already been solved. There is no unified conclusion about which compensation is the most reasonable for high-power CPT systems because of the scarcity of large-scale engineering experience in the high-power CPT sector. Performance-oriented design The performance needed can vary from case to case, depending on different application scenarios. Therefore, in achieving multiple design goals and achieving a balance between different performance indices, a performance-oriented design approach is important. Several candidates are discussed in terms of their practicality, taking into account the reliability and controllability issues of a high-power charging device. The most widely implemented compensation in charging schemes is the standard series-series (SS) compensation. To completely compensate for the auto-inductance at the resonant frequency, resonant capacitors are chosen. Due to symmetry and duality between the primary and secondary sides, a theoretically ideal reactive power compensation is obtained, independent of the coupling and load. Due to the superior reactive power compensation capability and its simple structure, high efficiency can be achieved. It can adapt to a broad range of battery systems where a constant current charging time is necessary, acting as a load-independent constant current source.

In (Bosshard & Kolar, 2016b) and (Galigekere et al., 2018) have a selection of SS applications for prototypes or consumer goods. Another value of reimbursement for the SS comes from its symmetrical form. In bidirectional wireless charging systems, compensation symmetry allows the voltage and current stress on both sides of the magnetic coupler to be equally distributed (Zahid, Dalala, Chen, Chen, & Lai, 2015).

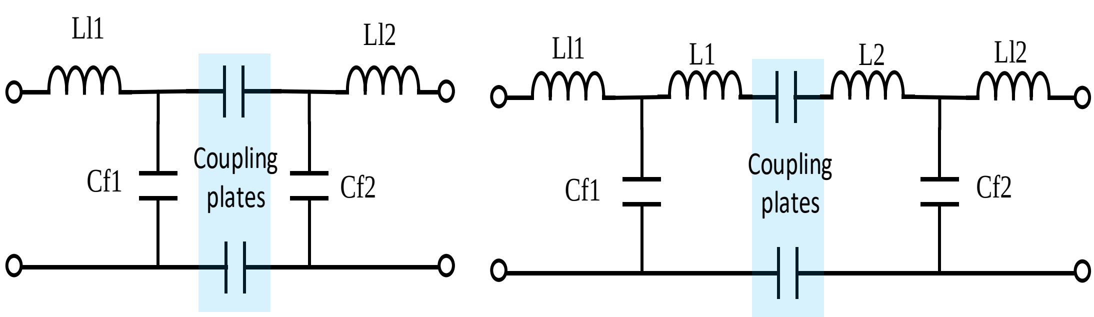

(a) (b)

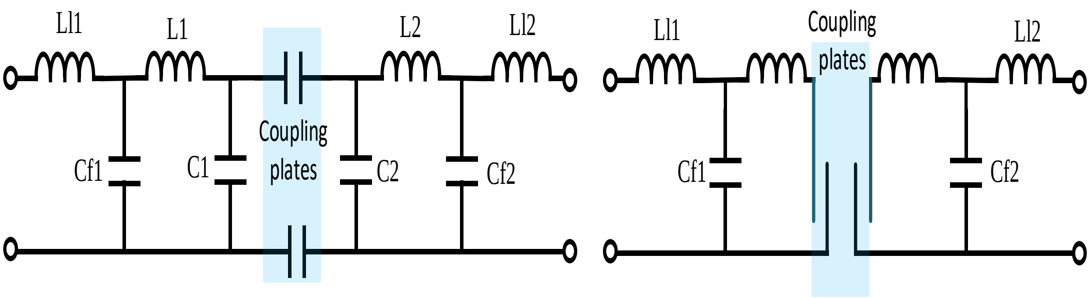

(c) (d)

Figure 2.19: Different CPCT compensations (Feng et al., 2020)

In addition, in both power flow directions, it retains equivalent voltage or current gain characteristics and facilitates their control. Tuning sensitivity is the drawback of SS compensation. Both have a high slope rate at the resonance stage, the output characteristic, as well as the input impedance, which gives a high sensitivity to the minimum parameter change. The effect could be a loss of soft-switching and a large difference in output. Either the resonant tank is slightly detuned to establish the ZVS condition for the power stage or the device operates slightly above the resonant frequency to add inductive loading at the output of the inverter. On the other hand, the mentioned problem, though alleviated, still exists. The SP compensation in which the operating point is chosen to realize a load-independent characteristic is another option for a high-power WPT scheme.

SP topology also has zero-phase-angle (ZPA) characteristics, suggesting that it is possible to fully remove the reactive power in the resonant network. However, this meritis fragile as the compensation capacitor is heavily dependent on magnetic coupling. The load-independent and ZPA properties will no longer hold once the coupling drifts away from the stated nominal state. Besides, due to the boost mode of parallel resonance, the voltage gain at the load-independent point is typically much higher than unity. This is not favored because the low number of secondary turns greatly decreases the secondary coil's quality factor, resulting in the deterioration of the transmission efficiency. Another downside of SP is that for load matching, the necessary coil inductance is typically too low to dissipate the losses produced in a high-power WPT system.

However, SP compensation may still be an ideal candidate for certain applications where the relative location is fixed and the power is relatively low. The presence of the front-end inductor can largely restrict the current flowing into the primary-side coil for LCL compensation. The voltage gain of the LCL-type resonant network is therefore typically low, making it ideal for low-voltage charging systems, low-speed EVs, electric scooters (Petersen & Fuchs, 2015) , lift trucks and distributed WPT systems where, as in the case of automatic guided vehicle (AGV) systems, multiple devices from a common rail are supplied (Covic & Boys, 2013). It can also be equipped with a parallel compensation on the secondary side to raise the voltage in EV charging scenarios.

LCL's practical problems lie in the fact that high-power, high-inductance inductors are normally expected to fit the inductance of the coil to ensure ZPA and soft-switching (Hao, Covic, & Boys, 2014), leading to higher losses. Building high-frequency resonant inductors with high inductance to handle high power is not practical from a manufacturing point of view, particularly considering their contemporaries in traditional resonant converters (LLC), which are typically less than 20 μH. Double-sided LCC systems have unity voltage gain with similar primary and secondary-side components and by changing the component values, the voltage gain is normally adjustable. The significant downside is the high number of components of compensation. Performance, reliability and simplicity are major design issues in high-power wireless charging systems. Hence, it is inferred that primarily due to its simplicity, SS compensation is an ideal solution for many applications. Real-time analysis of the input impedance and slight frequency changes are required to account for the non-ZVS conditions induced by the drift of operating conditions and parameters in order to ensure the safe and efficient system of high-power wireless chargers.

CHAPTER 3: : RESEARCH METHODOLOGY

3.1 Introduction

This chapter presents the novel S-S-LCLCC and the conventional S-S-S converter topologies and their equivalent circuit model. The operation of the proposed converter is explained in Section 3.3 based on the mutual inductance model. The proposed S-S-LCLCC converter employs a Fundamental Harmonic Approximation (FHA) for the steady-state analysis, which is detailed in Section 3.4. The characteristics of the proposed converter like voltage gain, voltage and current stresses of power devices are discussed further in Section 3.5-3.7. Section 3.8 and 3.9 derive the Quality factor and Power Delivery to Load equations to investigate the system's performance. Lastly, in Section 3.10, the prototype of the experimental setup and the components selections are discussed.

3.2 Analysis of S-S-S Compensation for Achieving CV with ZPA

The S-S-S compensation circuit is presented in Fig 3.1. The primary side of the circuit is connected to a full bridge inverter to convert DC power to high frequency AC square wave. The battery equivalent load resistance R_L is connected to a full bridge rectifier on the receiver side of the circuit. By applying FHA method, all of the high-order harmonics will be ignored for simplicity. Moreover, every switch operates at 50% duty cycle to maximize the output voltage and ω represents the operating angular frequency of the inverter. The AC equivalent circuit of S-S-S compensation topology is illustrated in Fig 3.1 (b), where the self-inductances of primary, relay and receiver coils are L_1, L_2 and L_3 respectively. C_1, C_2 and C_3 are the resonant capacitors, which contribute every coil to operate at resonant frequency and eventually allow the circuit to operate under ZPA condition. M_{12}, M_{13}, M_{23} are the mutual inductance between primary and relay coil, primary and receiver coil, relay and receiver coil respectively. R_i represents the total parasitic series resistance, X_i is the total reactance and ZL_{ip} and ZC_{ip} are the inductance of the coils and the capacitors as given in (3.1). R_L and R_s are the load and source resistance, respectively. ZM_{mn} is the mutual impedances between the coils as mentioned in (3.1) as follows:

$$\begin{cases} \mathrm{R}_1 = Rs + RL_1 + RC_1 \\ Xi = j\omega Li + \dfrac{1}{j\omega Ci} \qquad i = 1,2,3 \\ \mathrm{Ri} = R_{Li} + RCi \qquad i = 2,3 \\ \mathrm{ZL}ip = j\omega Lip \qquad i = 1,3 \\ \mathrm{ZC}ip = \dfrac{1}{j\omega Cip} \qquad i = 1,3 \end{cases} \qquad \begin{cases} m \neq n \\ m = 1,2 \quad \mathrm{ZM}mn = j\omega Mmn \\ n = 2,3 \end{cases} \tag{3.1}$$

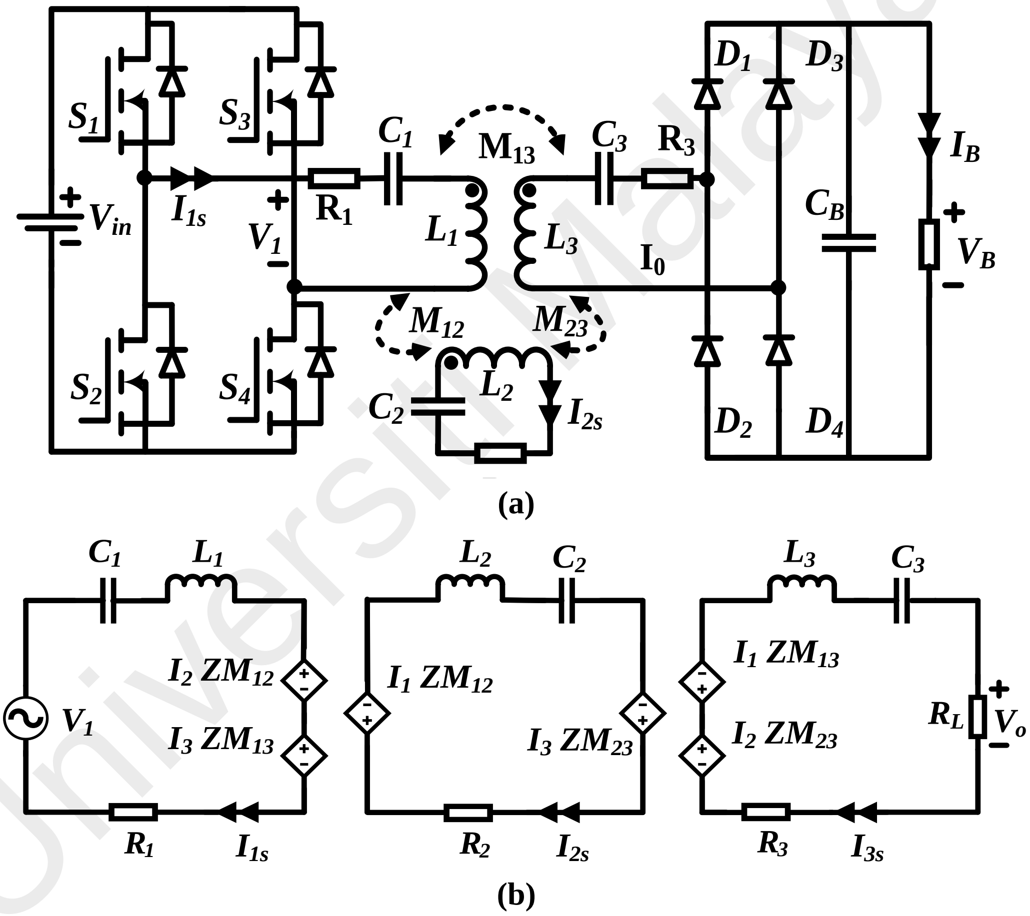

Figure 3.1: (a) Schematic circuit of S-S-S three coils compensation design(b) AC equivalent circuit of S-S-S compensation design

Based on Fig 3.1 (a) , the first harmonics can be determined as given in (3.2), where $V_1(t)$ represents the square waveform of the fundamental harmonic voltage with respect to time, V_{in} is the input DC voltage and θ is the difference in the phase angle of the input and output voltages.

$$\begin{cases} V_1(t) = \dfrac{4V_{in}\sin(2\pi ft)}{\pi} \\ V_O(t) = \dfrac{4V_B\sin(2\pi ft+\theta)}{\pi} \\ I_O(t) = \dfrac{\pi I_B\sin(2\pi ft+\theta)}{2} \\ R_L = \dfrac{8R_B}{\pi^2} \end{cases} \tag{3.2}$$

Based on Fig 3.1 (b), by applying Kirchhoff Voltage Law (KVL), the matrix equation of this system can be written as

$$\begin{bmatrix} V_1 \\ 0 \\ 0 \end{bmatrix} = \begin{bmatrix} X_1 + \mathrm{R}_1 & j\omega M_{12} & j\omega M_{13} \\ j\omega M_{12} & X_2 + \mathrm{R}_2 & -j\omega M_{23} \\ j\omega M_{13} & -j\omega M_{23} & X_3 + \mathrm{R}_3 + R_L \end{bmatrix} \begin{bmatrix} I_{1s} \\ I_{2s} \\ I_{Os} \end{bmatrix} \tag{3.3}$$

In order to show the basic characteristics of S-S-S compensation, based on the experimental setup in Table 3.4, which is from the same three coil system in (Y. Li et al., 2018), the effect of mutual inductance between the source and receiver coil is neglected due to its large distance and its small value of M_{13}, which is very close to zero. In addition, the magnitude of M_{13} is approximately ten times smaller than other mutual inductances. Recent studies have shown that M_{13} is capable of bringing the imaginary part into (3.3) and shifts the phase of the output voltage to above the resonant frequency and decreases the maximum efficiency of WPT system (Wang & Wang, 2018). In addition, it is also possible to eliminate the imaginary effect of this phenomenal even when the primary and receiver coils are close to each other by using a reactance compensation method. However, adopting the reactance compensation method requires designing capacitors at a specific load resistance, which prevents the designer to design the load-independent output voltage with ZPA characteristics during the entire process of charging. Another method has been proposed in (Wang & Wang, 2018) to achieve higher efficiency than the conventional design by adopting the compensatory reactance method as well.

Nonetheless, this design is also dependent on load resistance. Therefore, in this work, the same coil in (Y. Li et al., 2018) is implemented for better comparison analysis and the paper suggested in order to obtain the load-independent characteristics, M_{13} needs to be zero. Moreover, the parasitic resistances are also assumed to be zero and the system is operating at the resonant frequency. Nevertheless, in the next sections, the influences of parasitic resistances are analyzed since they are considered essential parameters for calculating the power efficiency. Therefore, after neglecting M_{13} and the internal resistances, the matrix equation of this system becomes:

$$\begin{bmatrix} V_1 \\ 0 \\ 0 \end{bmatrix} = \begin{bmatrix} 0 & j\omega M_{12} & 0 \\ j\omega M_{12} & 0 & -j\omega M_{23} \\ 0 & -j\omega M_{23} & R_L \end{bmatrix} \begin{bmatrix} I_{1s} \\ I_{2s} \\ I_{Os} \end{bmatrix} \tag{3.4}$$

By solving the matrix in (3.3), the voltage gain and input current can be derived as (Y. Li et al., 2018):

$$V_{0s} = \left(\frac{M_{23}}{M_{12}} \right) V_1 \qquad I_{1s} = \frac{V_1}{\mathrm{R}_L} \frac{M^2{}_{23}}{M^2{}_{12}} \tag{3.5}$$

The constant output voltage, which is independent of the load resistance with zero phase angle, can be achieved from (3.5). However, in this design, the output voltage is only dependent on the mutual inductances, frequency and input voltage, which makes the design limited to only the mentioned parameters. In addition, it has been shown in (Y. Li et al., 2018) that as R_L increases in small coil design with small mutual inductances that are mostly used in electric bicycles and small EV vehicles, the system efficiency tends to increase and then dramatically decreases.

3.3 Analysis of S-S-LCLCC Compensation for Achieving CV with ZPA

The CV mode is obtained in conventional S-S-S three coils design as shown in the previous analyses. In this design, the series compensation, which is connected to receiver coil, is now replaced by LCLCC design. The S-S-LCLCC compensation has similar characteristics with double-sided LCC design in two coils WPT system. The advantages of double LCC over S-S in two coil design are the power efficiency stability improvement, reducing reactive power and accomplishing load independent output voltage and current output at ZPA, improving misalignment and reducing voltage stress. Therefore, in this section, S-S-LCLCC system for three coils design is introduced in Fig 3.2 and is analyzed to achieve the load-independent CV and further improvement of power efficiency stability, misalignment and reducing voltage stress in comparison with conventional three-coil design.

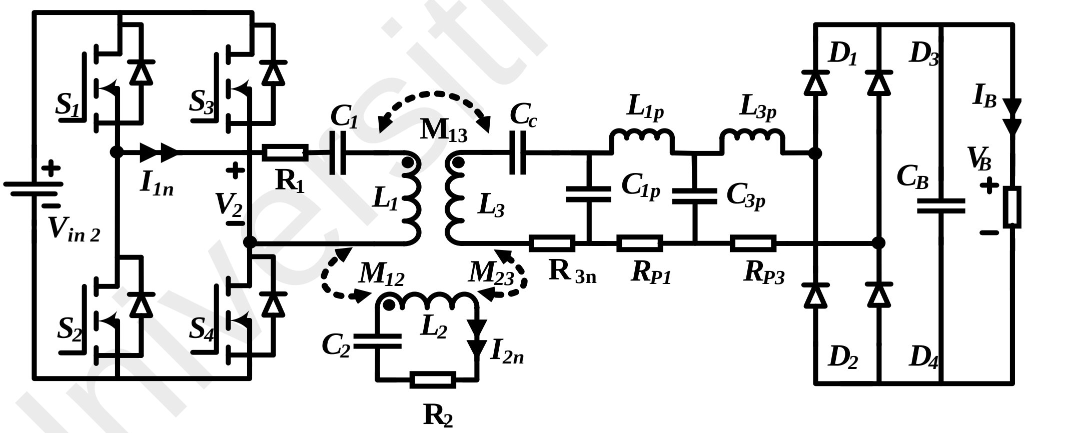

(a)

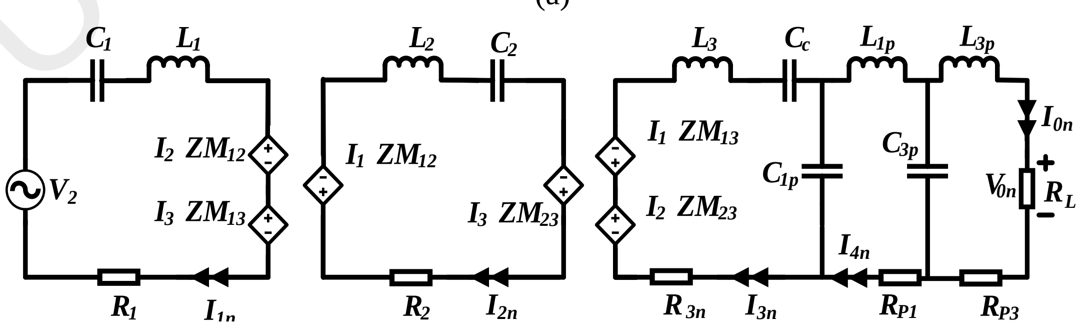

(b)

Figure 3.2: (a) Schematic circuit of S-S-LCLCC three coils compensation topology (b) AC equivalent circuit of S-S-LCLCC compensation topology

The system equations in Fig 3.2 can be expressed as

$$\begin{cases} V_2 = \left(X_1 + \mathrm{R}_1\right) I_{1n} + \left(\mathrm{ZM}_{12}\right) I_{2n} + \left(\mathrm{ZM}_{13}\right) I_{3n} \\ 0 = \left(\mathrm{ZM}_{12}\right) I_{1n} + \left(X_2 + \mathrm{R}_2\right) I_{2n} - \left(\mathrm{ZM}_{23}\right) I_{3n} \\ 0 = \left(\mathrm{ZM}_{13}\right) I_{1n} - \left(\mathrm{ZM}_{23}\right) I_{2n} + \left(\mathrm{ZL}_3 + \mathrm{ZC}_\mathrm{C} + \mathrm{ZC}_{1\mathrm{p}} + R_{3n}\right) I_{3n} - \left(\mathrm{ZC}_{1\mathrm{p}}\right) I_{4n} \\ 0 = -\left(\mathrm{ZC}_{1\mathrm{p}}\right) I_{3n} + \left(\mathrm{ZC}_{1\mathrm{p}} + \mathrm{ZL}_{1\mathrm{p}} + \mathrm{ZC}_{3\mathrm{p}} + R_{P1}\right) I_{4n} - \left(\mathrm{ZC}_{3\mathrm{p}}\right) I_{0n} \\ 0 = -\left(\mathrm{ZC}_{3\mathrm{p}}\right) I_{4n} + \left(\mathrm{ZL}_{3\mathrm{p}} + \mathrm{ZC}_{3\mathrm{p}} + R_{P3} + R_L\right) I_{0n} \end{cases} \tag{3.6}$$

R_{P1}, R_{P3} and R_{3n} can be calculated by

$$\begin{cases} R_{3n} = R_{L3} + R_{Cc} + R_{C1p} \\ R_{P1} = R_{C1p} + R_{L1p} + R_{C3p} \\ R_{P3} = R_{L3p} + R_{C3p} \end{cases} \tag{3.7}$$

For simplicity, similarly, the internal resistances of coils, additional inductors and capacitors are neglected. The design of additional inductors and capacitor are as follows:

$$\begin{cases} \mathrm{ZL}_{3\mathrm{p}} + \mathrm{ZC}_{3\mathrm{p}} = 0 \\ \mathrm{ZC}_{1\mathrm{p}} + \mathrm{ZL}_{1\mathrm{p}} + \mathrm{ZC}_{3\mathrm{p}} = 0 \\ \mathrm{ZL}_3 + \mathrm{ZC}_\mathrm{C} + \mathrm{ZC}_{1\mathrm{p}} = 0 \end{cases} \tag{3.8}$$

By substituting eq. (3.8) into eq. (3.6), more simplified equations can be transferred to a simpler matrix as follows:

$$\begin{bmatrix} V_2 \\ 0 \\ 0 \\ 0 \\ 0 \end{bmatrix} = \begin{bmatrix} 0 & \mathrm{ZM}_{12} & 0 & 0 & 0 \\ \mathrm{ZM}_{12} & 0 & \text{-}\mathrm{ZM}_{23} & 0 & 0 \\ 0 & \text{-}\mathrm{ZM}_{23} & 0 & \text{-}\mathrm{ZC}_{1\mathrm{p}} & 0 \\ 0 & 0 & \text{-}\mathrm{ZC}_{1\mathrm{p}} & 0 & \text{-}\mathrm{ZC}_{3\mathrm{p}} \\ 0 & 0 & 0 & \text{-}\mathrm{ZC}_{3\mathrm{p}} & R_L \end{bmatrix} \begin{bmatrix} I_{1n} \\ I_{2n} \\ I_{3n} \\ I_{4n} \\ I_{0n} \end{bmatrix} \tag{3.9}$$

Solving the above matrix, the current relationship and output voltage can be derived as it is stated in (3.10) . It is found that the input current is purely resistive. Therefore, achieving zero phase angle is possible. Moreover, load independent constant output voltage has been achieved. Unlike the conventional design, where the output voltage is only related to the frequency, the mutual inductances and input voltage, it is clear that the output voltage of LCLCC is also dependent on two additional capacitors C_{1p} and C_{3p}. Based on eq. (3.5) and last row of eq. (3.10) the condition when both S-S-S and S-S-LCLCC system have the same output voltage and delivering the same amount of output power can be obtained as (3.11):

$$\begin{cases} I_{1n} = \dfrac{V_2}{R_L}\left(\dfrac{\mathrm{ZM}_{23}}{\mathrm{ZM}_{12}}\right)^2\left(\dfrac{\mathrm{ZC}_{3\mathrm{p}}}{\mathrm{ZC}_{1\mathrm{p}}}\right)^2 = \dfrac{V_2}{R_L}\left(\dfrac{M_{23}}{M_{12}}\right)^2\left(\dfrac{C_{1p}}{C_{3p}}\right)^2 \\ I_{2n} = \dfrac{V_2}{\mathrm{ZM}_{12}} \\ I_{3n} = \dfrac{V_2}{R_L}\left(\dfrac{\mathrm{ZM}_{23}}{\mathrm{ZM}_{12}}\right)\left(\dfrac{\mathrm{ZC}_{3\mathrm{p}}}{\mathrm{ZC}_{1\mathrm{p}}}\right)^2 \\ I_{4n} = \dfrac{-V_2}{R_L}\left(\dfrac{\mathrm{ZM}_{23}}{\mathrm{ZM}_{12}}\right)\left(\dfrac{1}{\mathrm{ZC}_{1\mathrm{p}}}\right) \\ I_{0n} = \dfrac{-V_2}{R_L}\left(\dfrac{\mathrm{ZM}_{23}}{\mathrm{ZM}_{12}}\right)\left(\dfrac{\mathrm{ZC}_{3\mathrm{p}}}{\mathrm{ZC}_{1\mathrm{p}}}\right) = \dfrac{-V_2}{R_L}\left(\dfrac{M_{23}}{M_{12}}\right)\left(\dfrac{C_{1p}}{C_{3p}}\right) \\ V_{0n} = \left(\dfrac{M_{23}}{M_{12}}\right)\left(\dfrac{C_{1p}}{C_{3p}}\right)V_2 \end{cases} \tag{3.10}$$

$$\begin{cases} V_{0n} = V_{0s} \\ \dfrac{V_1}{V_2} = \left(\dfrac{C_{1p}}{C_{3p}}\right) \end{cases} \tag{3.11}$$

Where V_2 and V_{0n} are the AC input and output voltage of the new S-S-LCLCC design, V_1 and V_{0s} represent the AC input and output voltages of conventional S-S-S design respectively. Undoubtedly, the maximum efficiency of the conventional design is higher due to the additional capacitors and inductors of the new design. However, in the next section, by using the additional capacitor and input voltage, the overall efficiency of the system for the higher values of load resistance is significantly improved. This phenomenon is important since the second stage of the battery charging is CV for the higher values of equivalent load resistance of a battery in the recent WPT designs for EVs

(Y. Li et al., 2018; Tran et al., 2018; Vu, Tran, & Choi, 2018). Furthermore, this design has a contribution to improve misalignment and to shift the maximum efficiency to the desired load resistance. In the next sections, further analyses and comparison are discussed to prove the superior performance of the proposed design

3.4 Efficiency analysis of three coil system

As mentioned earlier, it is not possible to simply neglect the value of internal resistances in calculating the efficiency of the system. Therefore, the following equations are achieved by solving the last two rows of Matrix in eq. (3.3) for S-S-S compensation as

$$\begin{cases} \dfrac{I_{0S}}{I_{1S}} = \dfrac{\mathrm{ZM}_{12}\ \mathrm{ZM}_{23}}{\mathrm{ZM}^2{}_{23} - \mathrm{R}_2(\mathrm{R}_3 + R_L)} \\ \dfrac{I_{1S}}{I_{2S}} = \dfrac{\mathrm{ZM}^2{}_{23} - \mathrm{R}_2(\mathrm{R}_3 + R_L)}{\mathrm{ZM}_{12}(\mathrm{R}_3 + R_L)} \end{cases} \tag{3.12}$$

By substituting (3.12) into the first row of matrix in (3.3), the output current in terms of input voltage can obtained as

$$I_{0S} = \frac{\mathrm{ZM}_{12}\ \mathrm{ZM}_{23}}{\mathrm{R}_1\mathrm{ZM}^2{}_{23} + (\mathrm{R}_3 + \mathrm{R}_L)(\mathrm{ZM}^2{}_{12} - \mathrm{R}_1\mathrm{R}_2)} V_1 \tag{3.13}$$

Eventually, from (3.12) and (3.13), the input impedance and power efficiency of S-S-S three-coil system can be calculated as (J. Zhang et al., 2017):

$$Zin(\omega_0) = \frac{V_1}{I_{1S}} = \frac{\mathrm{R}_1\mathrm{ZM}^2{}_{23} + (\mathrm{R}_3 + \mathrm{R}_L)(\mathrm{ZM}^2{}_{12} - \mathrm{R}_1\mathrm{R}_2)}{\mathrm{ZM}^2{}_{23} - \mathrm{R}_2(\mathrm{R}_3 + \mathrm{R}_L)} \tag{3.14}$$

$$\eta_{3s} = \frac{P_{os}}{P_{1s}} = \frac{I^2{}_{0S}\mathrm{R}_L}{I_{1s}V_1} = \frac{\mathrm{R}_L}{q\mathrm{R}^2{}_L + w\mathrm{R}_L + e} \tag{3.15}$$

For better analysis of efficiency, q, w and e can be simplified further by assuming

$$\begin{cases} ZM^2{}_{23} - R_2R_3 \approx ZM^2{}_{23} \\ ZM^2{}_{12} - R_1R_2 \approx ZM^2{}_{12} \\ ZM^2{}_{23} - R_1R_3 \approx ZM^2{}_{23} \\ R_3 + R_L \approx R_L \end{cases} \tag{3.16}$$

Table 3.1: Complete and Simplified Equationsof Conventional S-S-S Three-Coil Design at Resonant frequency While Neglecting M13

	Complete Expressions	Simplified Expressions
q	$\frac{-R_2(ZM^2{}_{12} - R_1R_2)}{(ZM_{12}\ ZM_{23})^2}$	$\frac{-R_2}{ZM^2{}_{23}}$
w	$\frac{(ZM^2{}_{12} - R_1R_2)(ZM^2{}_{23} - R_2R_3) - R_2(R_1ZM^2{}_{23} + R_3(ZM^2{}_{12} - R_1R_2))}{(ZM_{12}\ ZM_{23})^2}$	1
e	$\frac{(R_1ZM^2{}_{23} + R_3(ZM^2{}_{12} - R_1R_2))(ZM^2{}_{23} - R_2R_3)}{(ZM_{12}\ ZM_{23})^2}$	$R_3 + \frac{R_1ZM^2{}_{23}}{ZM^2{}_{12}}$

This assumption is valid according to (J. Zhang et al., 2017). However, small error appears, which is caused by the simplification. Nevertheless, the performance of the simplified curve does not change. Table 3.1 shows the actual and simplified values of q, w and e for the conventional three-coil system. Based on the simplified model, the input impedance of this system can be further simplified as:

$$Zin_{3s} = \frac{R_1ZM^2{}_{23} + (R_3 + R_L)ZM^2{}_{12}}{ZM^2{}_{23} - R_2R_L} \tag{3.17}$$

Similar approach for calculating and simplifying LCLCC design has been used in this section in order to better differentiate the advantages of this topology in comparison to conventional design. The following equations are achieved by solving the last four rows of (3.6) and neglecting M_{13};

$$\begin{cases} \frac{I_{4n}}{I_{0n}} = \frac{R_L + \mathrm{R}_{P3}}{\mathrm{ZC}_{3P}} \\ \frac{I_{3n}}{I_{0n}} = \frac{\text{-}\mathrm{ZC}^2{}_{3P} + (R_L + \mathrm{R}_{P3})\mathrm{R}_{P1}}{\mathrm{ZC}_{1P}\mathrm{ZC}_{3P}} \\ \frac{I_{2n}}{I_{0n}} = \frac{\text{-}\mathrm{ZC}^2{}_{3P}\mathrm{R}_{3n} + (R_L + \mathrm{R}_{P3})(\mathrm{R}_{P1}\mathrm{R}3 - \mathrm{ZC}^2{}_{3P})}{\mathrm{ZC}_{1P}\mathrm{ZC}_{3P}\mathrm{ZM}_{23}} \end{cases} \tag{3.18}$$

$$\frac{I_{1n}}{I_{0n}} = \frac{\mathrm{ZC}^2{}_{3P}(\mathrm{R}_{3n}\mathrm{R}_2 - \mathrm{ZM}^2{}_{23})}{\mathrm{ZC}_{1P}\mathrm{ZC}_{3P}\mathrm{ZM}_{23}\mathrm{ZM}_{12}} - \frac{(R_L + \mathrm{R}_{P3})(\mathrm{R}_{P1}(\mathrm{R}_{3n}\mathrm{R}_2 - \mathrm{ZM}^2{}_{23}) - \mathrm{ZC}^2{}_{1P}\mathrm{R}_2)}{\mathrm{ZC}_{1P}\mathrm{ZC}_{3P}\mathrm{ZM}_{23}\mathrm{ZM}_{12}} \tag{3.19}$$

By substituting (3.16) into the first row of (3.6), the power efficiency of the system can be calculated as

$$\eta_{3n} = \mathrm{R}_L \frac{(\mathrm{ZC}_{1P}\mathrm{ZC}_{3P}\mathrm{ZM}_{23}\mathrm{ZM}_{12})^2}{AB} \tag{3.20}$$

where *A*, *B* and the input impedance are shown in Table 3.2. Analyzing of (3.20) is very complex, thus, to make the analysis and comparison simpler, similar simplification technique used in (3.15) is applied in (3.20). Therefore, the simplified efficiency expression of S-S-LCLCC design is

$$\eta_n = \frac{P_{0n}}{P_{1n}} = \frac{I^2{}_{0n}\mathrm{R}_L}{I_{1n}V1} = \frac{\mathrm{R}_L}{q_1\mathrm{R}_L^2 + w_1\mathrm{R}_L + e_1} \tag{3.21}$$

where q_1, w_1 and e_1 are expressed in Table 3.2

In order to have a better understanding at which load resistance the maximum efficiency appears, it is vital to calculate the optimum value of the output load using the partial derivative of the efficiency with respect to the load resistance. For simplicity, the simplified model is used as follows:

$$\frac{\partial \eta}{\partial R_L} = 0 \tag{3.22}$$

Solving (3.22), the optimal value of R_L can be derived for both of the conventional and new designs as follows:

$$R_L^{opt3s} = \sqrt{\frac{e}{q}} = \frac{M_{23}}{M_{12}} \sqrt{\frac{-1}{R_2}(ZM^2_{12}R_{3n} + ZM^2_{23}R_1)} \quad (3.23)$$

$$R_L^{opt3n} = \frac{C_{1P}M_{23}}{C_{3P}M_{12}} \sqrt{\frac{(ZC^2_{3P}ZM^2_{23}R_1 + ZM^2_{12}(ZC^2_{3P}R_{3n} + ZC^2_{1P}R_{P3})}{-R_{P1}ZM^2_{23} + R_2ZC^2_{1P}}} \quad (3.24)$$

Based on the recent charger designs of WPT battery, the lithium-ion battery charging process is divided into two stages. The first stage is happening when the equivalent load resistance of the battery is approximately between 10 and 30 Ω and in the second stage, the load resistance eventually increases from 30 to 250 Ω in order to accomplish CC and CV with ZPA respectively (Y. Li et al., 2018; Tran et al., 2018; Vu et al., 2018). Analyzing equation (3.23) yields that the optimum load resistance value of S-S-S system is proportional to the ratio of M_{23}/M_{13}. Additionally, since the main purpose of three-coil system is to have higher efficiency than conventional two-coil design, the study suggested that the relay coil is placed near to transmitter coil (J. Zhang et al., 2017). Optimum load resistance contributes to determine at which load resistance that the maximum efficiency will occur. Accordingly, the R_L^{opt3s} for S-S-S compensation in small coil designs, following the work in (Y. Li et al., 2018), will appear at much smaller value than 24 Ω in CV mode. It is clear that the maximum efficiency of the CV of this system will be placed in CC mode in (Y. Li et al., 2018). Therefore, the system cannot operate at its maximum efficiency. However, in the new S-S-LCLCC design, by using additional capacitors in (3.24), the optimal R_L^{opt3n} of S-S-LCLCC can be shifted to much higher load resistance without changing the coils design. This is very significant property since CV mode is operating at light load (higher equivalent load resistance of the battery) and it is able to achieve its highest efficiency

Table 3.2: Complete and Simplified Equations of S-S-LCLCC Three Coil Topology At Resonant Frequency and Neglecting M_{13}

	Complete Expressions
A	$(ZC^2_{3P}(R_{3n}R_2 - ZM^2_{23}) - (R_L + R_{P3})(R_{P1}(R_{3n}R_2 - ZM^2_{23}) - ZC^2_{1P}R_2))R1$ $+(-ZC^2_{3P}R_{3n} + (R_L + R_{P3})(R_{P1}R_{3n} - ZC^2_{1P}))ZM^2_{12}$
B	$ZC^2_{3P}(R_{3n}R_2 - ZM^2_{23}) - (R_L + R_{P3})(R_{P1}(R_{3n}R_2 - ZM^2_{23}) - ZC^2_{1P}R_2)$
Zin_n	$\dfrac{(R_L + R_{P3})(ZC^2_{1P}R_2)R1 - ZC^2_{3P}R_{3n}ZM^2_{12} - (R_L + R_{P3})ZC^2_{1P}ZM^2_{12}}{-ZC^2_{3P}ZM^2_{23} + (R_L + R_{P3})(R_{P1}ZM^2_{23} + ZC^2_{1P}R_2)}$

	Simplified Expressions		
A	$R_L(R_{P1}R_1ZM^2_{23} + ZC^2_{1P}R_2R_1 - ZC^2_{1P}ZM^2_{12}) - ZC^2_{3P}ZM^2_{23}R_1 - ZC^2_{3P}ZM^2_{12}R_{3n}$	q_1	$-\dfrac{R_{P1}ZM^2_{23} + R_2ZC^2_{1P}}{ZC^2_{3P}ZM^2_{23}}$
B	$ZC^2_{3P}(-ZM^2_{23}) - (R_L + R_{P3})(-R_{P1}ZM^2_{23} - ZC^2_{1P}R_2)$	w_1	1
Zin_n	$\dfrac{ZM^2_{12}(ZC^2_{3P}R_{3n} + (R_L + R_{P3})ZC^2_{1P})}{ZC^2_{3P}ZM^2_{23} - (R_L + R_{P3})(R_{P1}ZM^2_{23} + ZC^2_{1P}R_2)}$	e_1	$\dfrac{ZC^2_{3P}ZM^2_{23}R_1}{ZC^2_{1P}ZM^2_{12}} + \dfrac{ZC^2_{3P}R_{3n}}{ZC^2_{1P}} + R_{P3}$

3.5 Analysis of The Energy Efficiency Stiffness

This section illustrates the comparison of load variation and its effect on the energy efficiency stiffness to witness the stability of the energy efficiency of the conventional and proposed design more clearly as the equivalent battery load resistance changes. In order to analyze the energy stability of both systems, the second order differentiation of the efficiency with respect to load resistance at $\partial\eta/\partial RL = 0$ is (J. Zhang et al., 2017):

$$\left.\frac{\partial^2 \eta_{3s}}{\partial RL^2}\right|_{\frac{\partial \eta}{\partial RL}=0} = -2\frac{q}{e}\frac{\sqrt{qe}}{(2\sqrt{qe} + w)^2} \tag{3.25}$$

$$\left.\frac{\partial^2 \eta_{3n}}{\partial RL^2}\right|_{\frac{\partial \eta}{\partial RL}=0} = -2\frac{q_1}{e_1}\frac{\sqrt{q_1 e_1}}{(2\sqrt{q_1 e_1} + w_1)^2} \tag{3.26}$$

By dividing Eq. (3.25) with Eq. (2.36), the relationship of the energy stiffness can be expressed as

$$\frac{\left.\dfrac{\partial^2 \eta_{3s}}{\partial RL^2}\right|_{\frac{\partial \eta}{\partial RL}=0}}{\left.\dfrac{\partial^2 \eta_{3n}}{\partial RL^2}\right|_{\frac{\partial \eta}{\partial RL}=0}} = \frac{qe_1}{eq_1} \frac{4\sqrt{q_1 e_1} + \dfrac{w_1{}^2}{\sqrt{q_1 e_1}} + 4w_1}{4\sqrt{qe} + \dfrac{w^2}{\sqrt{qe}} + 4w} \tag{3.27}$$

In addition, to have better comparison and more accurate results, both systems are designed to have the same output voltage when delivering the same amount of power. As discussed earlier, in Eq. (3.11), the output voltage of LCLCC topology is proportional to the ratio of C_{1P} / C_{3P}. In the experimental design, C_{1P} is set to be approximately 1.42 times larger than C_{3P}. Therefore, the input voltage of LCLCC topology is 0.7 times the input voltage of S-S-S system in Eq. (3.10). Thus, $C_{3P} = 0.7\, C_{1P}$ and by substituting this equation into Table 3.1 and Table 3.2, the relationship between the parameters of power efficiency between S-S-S and S-S-LCLCC can be obtained as:

$$\begin{cases} q \succ q_1 \\ e_1 \succ e \end{cases} \tag{3.28}$$

Moreover, the effect of additional capacitors in e_1/e is much larger than q_1/q, yielding

$$\begin{cases} qe_1 \succ q_1 e \\ q_1 e_1 \succ qe \end{cases} \tag{3.29}$$

$$\left.\frac{\partial^2 \eta_{3s}}{\partial RL^2}\right|_{\frac{\partial \eta}{\partial RL}=0} \succ \left.\frac{\partial^2 \eta_{3n}}{\partial RL^2}\right|_{\frac{\partial \eta}{\partial RL}=0} \tag{3.30}$$

Eq. (3.29) shows that as the load resistance in S-S-S three-coil system increases, the energy efficiency stiffness decreases much faster compared to S-S-LCLCC system as a result of having much larger slope.

3.6 Analysis and design of the additional components of the proposed system

It is vital to illustrate the effect of the additional capacitors for having better comparison analysis between conventional and the new design. Therefore, the ratio between C_{3P} / C_{1P} is defined as $\alpha = C_{3P} / C_{1P}$. By substituting (α) into Eq.. (3.21) and

Simplified Expressions in Table 3.2, the less complex efficiency equation of the new system can be express as:

$$\eta_{3n} = \left(\mathrm{R}_L \left(\frac{a^2(\omega^4 M_{23}^2 \mathrm{C}_{1P}^2 \mathrm{R}_{P1} + \mathrm{R}_2)}{\omega^2 M_{23}^2} \right) + 1 + \frac{1}{\mathrm{R}_L} \left(\frac{M_{23}^2 \mathrm{R}_1}{a^2 M_{12}^2} + \frac{\mathrm{R}_{3n}}{a^2} + \mathrm{R}_{P3} \right) \right)^{-1} \tag{3.31}$$

Eq. (3.31) states that the smaller value of (α) can significantly improve the efficiency for the larger values of R_L in the S-S-LCLCC three coils system. Further discussion and detailed analysis of the additional capacitors will be discussed in chapter 4 by simulating Eq. (3.31)

3.7 Voltage Stress

In the recent three coils S-S-S design, the study in (Zhong, Zhang, Liu, & Hui, 2015) suggested that relay coil (L_2) should be much larger than transmitter and receiver coils. Moreover, the primary coil should be placed near or on the same plane as the relay coil in order the system to have higher efficiency than two-coil design (J. Zhang et al., 2017). However, this makes the current across the relay coil to be very large compare to other coils and it also increases the voltage stress across the resonant relay capacitor C_2 . Duo to the mentioned reasons, the S-S-S system requires a large quantity of capacitor in order to form the suitable C_2.(Y. Li et al., 2018; J. Zhang et al., 2017) This can be seen clearly in the experimental and measurement setup of (Y. Li et al., 2018) and the main losses is due to relay coil and its capacitor By solving the first row of matrix Eq. (3.4), the relay current (I_{2s}) in conventional S-S-S design can be calculated as (Y. Li et al., 2018)

$$I_{2s} = \frac{V_1}{\mathrm{ZM}_{12}} \tag{3.32}$$

By using Eq. (3.10), Eq. (3.11) and Eq. (3.32) the relationship between relay current of the new and the conventional design when both systems delivering the same amount of output power can be express as

$$I_{2n} = a(I_{2s}) \tag{3.33}$$

Since α =0.7, it is obvious that S-S-LCLCC topology has much smaller current across the relay coil, which indicates that the voltage stress across C_2 in the new system is much smaller than conventional design. Since the main losses in three coils system happens in relay coil, reducing current across this coil can be beneficial, which can be done by using smaller α.This also supports Eq. (3.31), which prove a better performance of the new design.

3.8 Quality factor and Power Delivery to Load

Power transfer efficiency (PTE) and Power delivery to load (PDL) of conventional three-coil system have been discussed in (Kiani et al., 2011; Y. Zhang, Lu, & Zhao, 2014) and they are often considered as important factors in the analysis of new compensation design. In order to derive the PDL of both conventional and new design, it is important to investigate the effect of the reflected impedances.

From Fig. 3.1, by ignoring the M_{13}, the reflected impedance of the receiver coil on the transmitter coil and the reflected impedance of the transmitter coil on the primary coil can be defined as (Z_{rt_3s}=$(\omega M_{23})^2/(X_3+R_3+R_L)$) and ($Z_{tp\_3s}$=$(\omega M_{12})^2/(X_2 + Z_{rt\_3s} + R_2)$), respectively. Therefore, by using Z_{rt_3s} and Z_{tp_3s}, the equivalent input impedance and PTE of S-S-S compensation can be derive as (Machnoor, Rodríguez, Kosta, Stang, & Lazzi, 2019).

$$Zin = Z_{tp\_3s} + X_1 + \mathrm{R}_1 \tag{3.34}$$

$$\eta_{3s} = \mathrm{PTE}_{3s} = \left(\frac{Z_{tp\_3s}}{Z_{tp\_3s} + \mathrm{R}_1}\right)\left(\frac{Z_{rt\_3s}}{Z_{rt\_3s} + \mathrm{R}_2}\right)\left(\frac{\mathrm{R}_L}{\mathrm{R}_L + \mathrm{R}_3}\right) \tag{3.35}$$

Note that when the S-S-S system operates at the resonant frequency (X_1=X_2=X_3=0), Eq. (3.34) and (3.35) will be the same as Eq. (3.14) and (3.15), respectively. By substituting (Q_1= $\omega L_1/R_1$), (Q_2= $\omega L_2/R_2$), (Q_3= $\omega L_3/(R_3+R_L)$), (M_{12}= $K_{12}\sqrt{L_1L_2}$) and

(M_{23}= $K_{23}\sqrt{L_2 L_3}$) into Eq. (36) and Eq. (37), PTE and PDL of conventional design in terms of the coupling coefficient and quality factor can be express as (Kiani et al., 2011)

$$\eta_{3s} = \left(\frac{(K_{12}^2 Q_1 Q_2)(K_{23}^2 Q_2 Q_3)}{(K_{12}^2 Q_1 Q_2 + K_{23}^2 Q_2 Q_3 + 1)(K_{23}^2 Q_2 Q_3 + 1)} \right) \left(\frac{\mathrm{R}_L}{\mathrm{R}_L + \mathrm{R}_3} \right) \tag{3.36}$$

$$\mathrm{PDL}_{3s} = P_{in}\eta_{3s} = \frac{V_1^2}{\mathrm{R}_1} \left(\frac{(K_{12}^2 Q_1 Q_2)(K_{23}^2 Q_2 Q_3)}{(K_{12}^2 Q_1 Q_2 + K_{23}^2 Q_2 Q_3 + 1)^2} \right) \left(\frac{\mathrm{R}_L}{\mathrm{R}_L + \mathrm{R}_3} \right) \tag{3.37}$$

As can be seen clearly in (3.36) and (3.37), expression ($k_{12}^2 Q_1 Q_2$) and ($k_{23}^2 Q_2 Q_3$) are playing critical role in both PTE and PDL performance of conventional design. Increasing or lowering down the value of ($k_{12}^2 Q_1 Q_2$) and ($k_{23}^2 Q_2 Q_3$) can be done by varying K_{12}, K_{23}, Q_1, Q_2 and Q_3. Quality factor of each coils are dependent on operating angular frequency, ac resistance and inductance of each coil. However, since, the design of the main coils is out of the scope of this paper, L_1, L_2 and L_3 have been adopted from the study in (Y. Li et al., 2018) and to make the comparison as fair as possible the operating angular frequency is also set to be the same as the mentioned study. This indicates that the value of Q_1, Q_2 and Q_3 will be constant. Therefore, the only parameters which can vary the value of ($k_{12}^2 Q_1 Q_2$) and ($k_{23}^2 Q_2 Q_3$) in this particular work are K_{12} and K_{23}..

Verifying efficiency formula for conventional system with using reflected equivalent impedance method and comparing the PDL and PTF equations in terms of quality factor and coupling coefficient have been discussed in the previous analysis.

The equivalent circuit of the S-S-LCLCC design is shown in Fig 3.3. In order to have detailed analysis, the efficiency and the equivalent impedance of each block diagram are derived and extracted as shown in Table 3.3

From Fig 3.3, the reflected equivalent impedance of the receiver coil on the transmitter coil and the reflected impedance of the transmitter side on the primary side for the new S-S-LCLCC system can be expressed as (Z_{rt}=(ωM_{23})^2/Z_r) and (Z_{tp}=(ωM_{12})^2/(X_2+Z_{rt}+R_2)) respectively. Consequently, the efficiency of the receiver coil and PTE of the S-S-LCLCC system are expressed as

$$\eta_{receiver} = \eta_{Za} \cdot \eta_{Zb} \cdot \eta_{Zc} \cdot \eta_{Zd} \cdot \eta_{Zr} \tag{3.38}$$

$$\mathrm{PTE}_n = \left(\frac{Z_{tp}}{Z_{tp} + \mathrm{R}_1}\right)\left(\frac{Z_{rt}}{Z_{rt} + \mathrm{R}_2}\right)\eta_{receiver} \tag{3.39}$$

Similar to the previous analysis, by substituting Q_1, Q_2, K_{12}, K_{23} and ($Q_n=\omega L_3/\mathrm{Re}(Z_r)$) into (3.38) and (3.39), PTE and PDL of LCLCC system in terms of coupling coefficient and quality factor can be expressed as

$$\eta_n = \eta_{receiver} \cdot \left(\frac{(K_{12}^2 Q_1 Q_2)(K_{23}^2 Q_2 Q_n)}{(K_{12}^2 Q_1 Q_2 + K_{23}^2 Q_2 Q_n + 1)(K_{23}^2 Q_2 Q_n + 1)}\right) \tag{3.40}$$

$$\mathrm{PDL}_n = \frac{\eta_{receiver} \cdot V_1^2}{\mathrm{R}_1}\left(\frac{(K_{12}^2 Q_1 Q_2)(K_{23}^2 Q_2 Q_n)}{(K_{12}^2 Q_1 Q_2 + K_{23}^2 Q_2 Q_n + 1)^2}\right) \tag{3.41}$$

Table 3.3 :Impedences and efficiency of block of the receiver side

Symbol	Equivalent Impedance	Efficiency (η)
Z_a	$\mathrm{ZL}_{3p} + R_{L3p} + R_L$	$\frac{R_L}{R_{L3p} + R_L}$
Z_b	$(\mathrm{ZC}_{3p} + R_{C3p}) \Vert Z_a$	$\frac{\lvert Z_b\rvert^2 \mathrm{Re}(Z_a)}{\lvert Z_a\rvert^2 \mathrm{Re}(Z_b)}$
Z_c	$\mathrm{ZL}_{1p} + R_{L1p} + Z_b$	$\frac{\mathrm{Re}(Z_b)}{R_{L1p} + \mathrm{Re}(Z_b)}$
Z_d	$(\mathrm{ZC}_{1p} + R_{C1p}) \Vert Z_c$	$\frac{\lvert Z_d\rvert^2 \mathrm{Re}(Z_c)}{\mathrm{Re}(Z_d)\lvert Z_c\rvert^2}$
Z_r	$\mathrm{ZL}_3 + \mathrm{ZC}_C + R_{L3} + R_{Cc} + Z_d$	$\frac{\mathrm{Re}(Z_d)}{R_{L3} + \mathrm{Re}(Z_d) + R_{Cc}}$

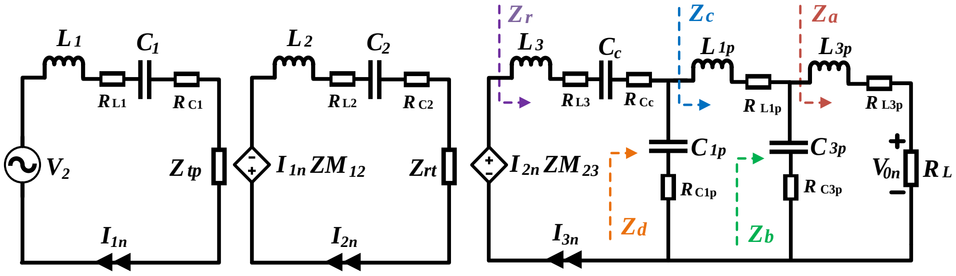

Figure 3.3: The equivalent circuit of proposed S-S-LCLCC

3.9 Misalignment performance

The effect of misalignment has been shown in many recent studies for two, three and four-coil systems theoretically and experimentally. Misalignment is mainly depending on the coil and compensation design and it is inversely proportional to the power efficiency. Moreover, it has been shown in (W. Li, Zhao, Deng, Li, & Mi, 2016; J. Zhang et al., 2017) that three-coil system and double-sided LCC in two-coil system perform better than conventional series-series two coil topology in terms of misalignment. Since misalignment is considered an important factor for WPT applications, the effect of it on the new S-S-LCLCC design is analyzed and compared in this section.

It has been shown in conventional three-coil system that as the mutual inductance decreases, the output and input power also tend to decrease, which makes the control part of WPT way simpler. Consequently, no additional converter for controlling the output current is required. In a typical three-coil system, the transmitter coil and relay coil are placed at the same plane. Therefore, only M_{23} will change as misalignment occurs. In order to have better comparison, both input current of S-S-S and S-S-LCLCC designs are calculated as:

$$\begin{cases} I_{1S} = \dfrac{V1}{Zin} = \dfrac{V1(\mathrm{ZM}^2{}_{23} - \mathrm{R}_2\mathrm{R}_L)}{\mathrm{R}_1\mathrm{ZM}^2{}_{23} + (\mathrm{R}_{3n} + \mathrm{R}_L)\mathrm{ZM}^2{}_{12}} \\ I^{ZM_{23}\simeq 0}{}_{1S} = \left| V1 \dfrac{\text{-}\mathrm{R}_2\mathrm{R}_L}{(\mathrm{R}_{3n} + \mathrm{R}_L)\mathrm{ZM}^2{}_{12}} \right| \end{cases} \tag{3.42}$$

$$\begin{cases} \left|I_{1n}\right| = \left|\dfrac{V1}{Zin_{3n}}\right| = \left|\dfrac{V1(\mathrm{ZC}^2{}_{3P}\mathrm{ZM}^2{}_{23} - (\mathrm{R}_L + \mathrm{R}_{P3})(\mathrm{R}_{P1}\mathrm{ZM}^2{}_{23} + \mathrm{ZC}^2{}_{1P}\mathrm{R}_2))}{\mathrm{ZM}^2{}_{12}(\mathrm{ZC}^2{}_{3P}\mathrm{R}_{3n} + (\mathrm{R}_L + \mathrm{R}_{P3})\mathrm{ZC}^2{}_{1P})}\right| \\ \left|I^{ZM_{23}\simeq 0}{}_{1n}\right| = \left|V1 \dfrac{-(\mathrm{R}_L + \mathrm{R}_{P3})(\mathrm{ZC}^2{}_{1P}\mathrm{R}_2)}{\mathrm{ZM}^2{}_{12}(\mathrm{ZC}^2{}_{3P}\mathrm{R}_{3n} + (\mathrm{R}_L + \mathrm{R}_{P3})\mathrm{ZC}^2{}_{1P})}\right| \end{cases} \tag{3.43}$$

In this section, similar characteristics happen in LCLCC design. This can be seen from Eq. (3.43) that when ZM_{23} decreases, the nominator becomes smaller and eventually becomes a constant when the maximum misalignment occurs. In addition, as the input current decreases, lesser power will be delivered to the receiver coil, which is the same as the conventional system in Eq. (3.45), where the output current of S-S-LCLCC also decreases in case of misalignment.

3.10 Experimental Setup

To verify the theoretical and simulation results, an experimental three-coil WPT system is implemented and tested as shown in Fig 3.4. Conduction losses are the main losses of the coils. Therefore, to eliminate it and make it as small as possible, Litz wire with 900 strands and a diameter of 4mm is used due to its low AC resistance magnitude. Further details of the number of turns and the size of coil can be found in (Y. Li et al., 2018) since the coil design and structure is adopted from the mentioned study to make a better comparison. However, there is a 5 mm gap between the primary and relay coil to make M_{13} affect smaller. All of the measured values at 200 kHz are provided in Table 3.4.

In order to compare S-S-S and S-S-LCLCC compensation, C_{1P}, C_{3P} and V_2 are designed using Eq. (3.11) to maintain the same power level for both topologies. Due to high carrying current potential and low equivalent series resistance (ESR), film capacitors are used. Moreover, air-core AC inductors have been adopted in this design since they have good performance compared to magnetic core inductance in the case of operating at high voltage conditions (Kazimierczuk & Sekiya, 2009) and availability in the laboratory. However, it is possible to use magnetic core inductance to minimize the coupling between the coils and to reduce the leakage to metal materials. Consequently, two additional air-core AC inductors with a diameter of 5cm are adopted in this topology. The capacitors, self-inductances, AC resistances and mutual inductances of the coils are measured using GwInstek-6300 LCR meter, which has the capability to provide accurate measurement up to 300 kHz. From the DC power supply, the power is transferred to the H-bridge inverter with the operating frequency of 200 kHz, the resonator, rectifier and eventually to the DC load, which acts like a battery charger. In the proposed system, four MOSFETs

(C2M0080120D) with 80 mΩ Rds on and fast recovery diodes (DSEI2X101-06A) are used for the inverter and rectifier respectively. The waveforms are taken by using Tek DPO3014 oscilloscope. For the measurement of power efficiency, YOKOGAWA WT500 power analyzer is used.

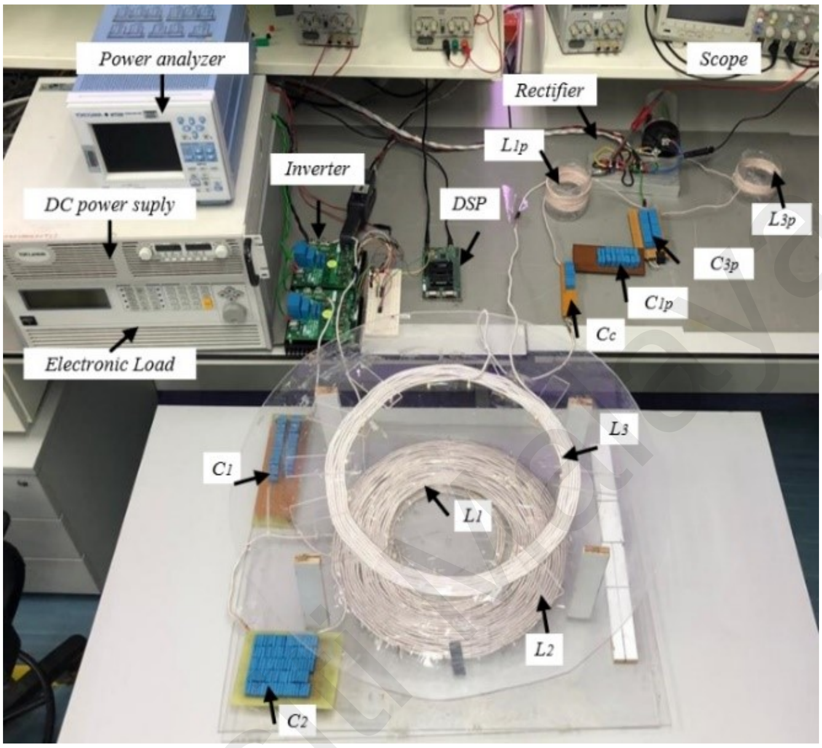

Figure 3.4: Three-coil S-S-LCLCC Prototype

Table 3.4:Experimental Measurement of The Parameters of S-S-LCLCC and S-S-S Three-Coil Wireless Power Transfer System

$L1$	$3.85\mu H$	$C1$	$164.49nF$	$M12$	$7.11\mu H$
$L2$	$163.21\mu H$	$C2$	$3.88nF$	$M23$	$7.17\mu H$
$L3$	$37.12\mu H$	$C3$	$17.06nF$	$M13$	$0.24\mu H$
$L1$p	$17.48\mu H$	$C1$p	$88.04nF$	$C3$p	$61.5nF$
Vin 1	$100V$	Cc	$21.16nF$	$L3$p	$10.3\mu H$
Vin 2	$70V$	VB	$100V$	IB	$4.2A$
RL2	0.31Ω	RC1p	$12.3m\Omega$	RC3p	$17.8m\Omega$
RL3	$99m\Omega$	RCc	$24.8m\Omega$	RL3p	$66m\Omega$
RL1p	$78m\Omega$	RL	$8\text{-}222\Omega$	RL1	$42m\Omega$
RC1	$4.6m\Omega$	RC2	$172.1\ m\Omega$	RC3	$7.3\ m\Omega$

Figure 3.5: A General Flow Chart to obtain Various Comparion between S-S-S and S-S-LCLCC Topologies

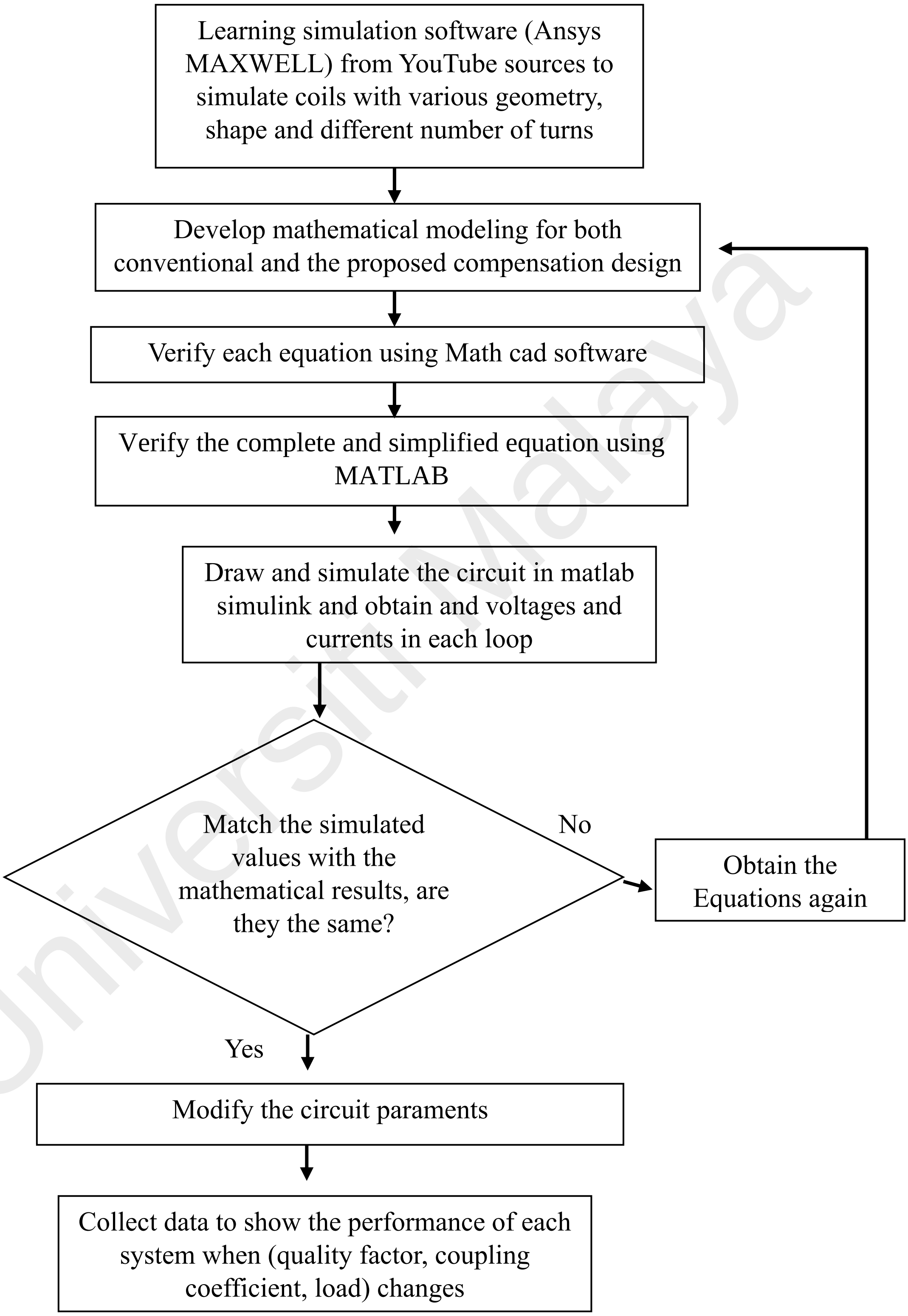

CHAPTER 4: RESULTS AND DISCUSSION

4.1 Introduction

The simulation and experimental results of the three-coil WPT system are presented in this chapter to verify the theoretical analysis. Moreover, base on the simulation results, the condition where the proposed work can outperform the conventional system has been analyzed and discussed in detail. Simplified formula for the efficiency equation and power delivery to load is also presented in this chapter to make analysis less complicated.

4.2 Simulation of Simplified Formula and Efficiency Analysis of WPT system

For the verification of the simplified formula in Eq. (3.15) and (3.20), the curve and characteristic of the power efficiency of the conventional three-coil design and S-S-LCLCC three-coil system are determined by MATLAB using the equations in Table 3.1, Table 3.2, Eq. (3.14), (3.17) and (3.20). Both tables consist of complete and simplified equations at the resonant frequency to make the analysis and design less complex. The parameters of both designs are shown in Table 3.3. Fig 4.1 shows the simulation results of the complete and simplified methods. The results have approximately 3% error, but the simplified method has a very similar trend, characteristics and shape as the original model. Therefore, according to Fig. 4.1, it is acceptable to use the simplified equations for analysis of the conventional and LCLCC three-coil designs. Consequently, by using the simplified parameters in Table 3.1 and Table 3.2, the graph of the first order differentiation of efficiency with respect to load resistance can be plotted in Fig. 4.2. It has been shown in Fig 4.2, for small value of load resistance, both systems have very sharp slopes. However, after the system reaches its maximum efficiency at around 7 Ω, the system efficiency tends to decrease rapidly in the S-S-S system.

On the other hand, S-S-LCLCC has much smaller change after 14.2 Ω, where its maximum efficiency appears. Therefore, the efficiency of S-S-LCC is much more stable than the conventional system, especially at higher load resistance. As mentioned earlier, CV stage operation area is designed for a larger value of the load resistance in the recent studies. Therefore, S-S-LCLCC has a significant advantage of power efficiency stability compared to S-S-S topology

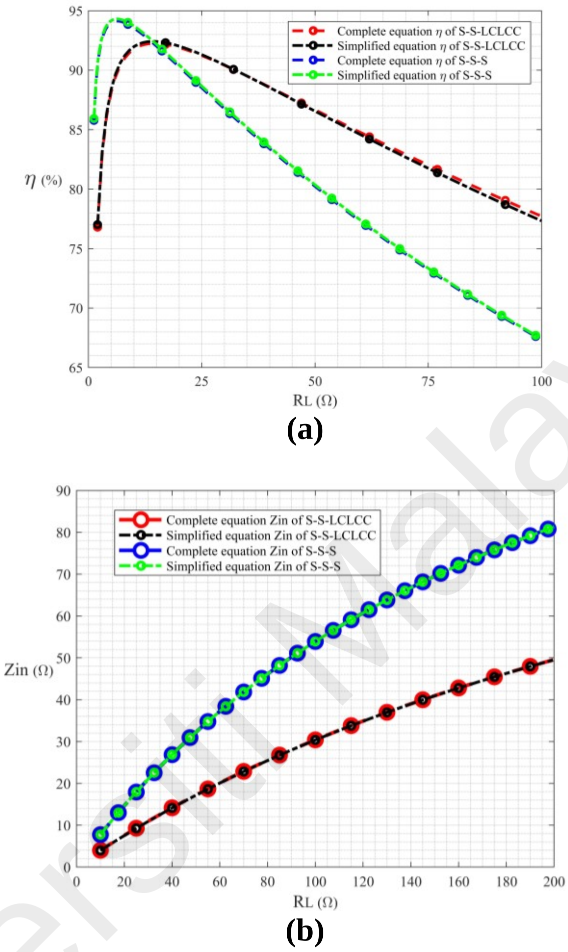

Figure 4.1: (a) Simulated Power efficiency of S-S-S and S-S-LCLCC system (b) Simulated Input Impedances of S-S-S and S-S-LCLCC topology

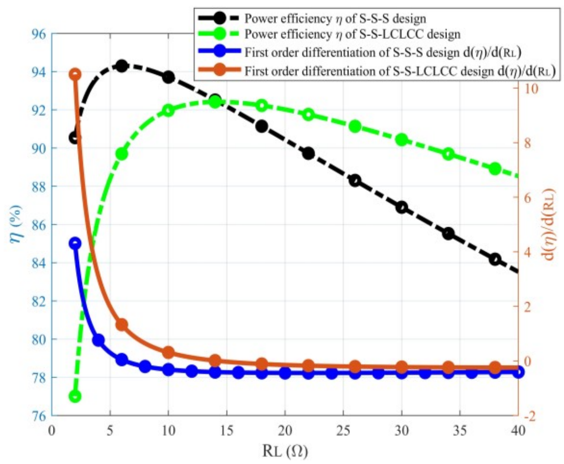

Figure 4.2: Simulated energy stiffness of S-S-S and S-S-LCLCC

4.3 Simulation Results for Selecting Additional Capacitors

As mentioned in Chapter 3, It is essential to show the effect of the additional capacitors for having better comparison analysis between conventional and the proposed new design. Therefore, by using Eq. (3.31) and simplified parameters in Table 3.2, the simulated efficiency of S-S-LCLCC with respect to (α) has been plotted in Fig 4.3.

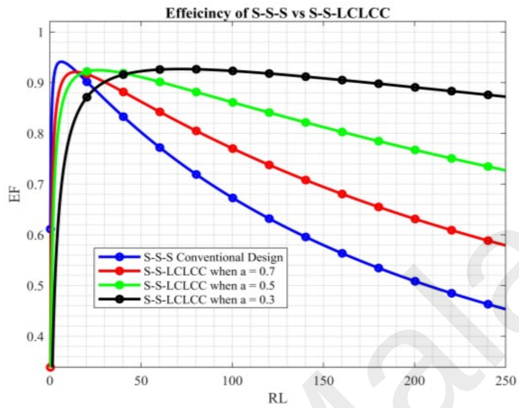

Figure 4.3: Simulated Efficiency of S-S-S and S-S-LCLCC in Terms of (α)

Fig 4.3 shows when α = 0.3, the performance efficiency of S-S-LCLCCC becomes much better than conventional design for larger values of R_L, which supporting Eq. (3.31). However, according to Eq. (3.10) and (3.11) as C_{3P} / C_{1P} ratio becomes smaller, the voltage gain of the new system increases. Since one of the main objectives of this work is to compare the performance analysis of new S-S-LCLCC design with S-S-S compensation in (Y. Li et al., 2018), the value of α is chosen to be 0.7. This is done so that the input voltage of the new design becomes closer value to the input voltage in (Y. Li et al., 2018) and by applying the Eq. (3.11), both designs can deliver the same output power and voltage for the fair comparison. Another approach in this work is choosing the additional inductors to be much smaller than relay and receiver coils since in the recent double-sided LCC design in two coil systems, additional inductors are usually chosen to be much smaller than the main coils (Vu et al., 2018). After selecting the value of additional inductor L_{3P} and α, it is now possible to calculate all other additional components for the new S-S-LCLCC design by using Eq. (3.8).

4.4 Quality factor and Power Delivery to Load simulation and discussion

In section 3.8, the formula for calculating power delivery to load and power transfer efficiency with respect to the quality factor of each coil has been derived. However, analysis of PDL and PTE is not simple since decreasing ($k_{23}^2 Q_2 Q_3$) causes (Z_{rt_3s} / Z_{rt_3s} +R_2) decreases and it increases the value of (Z_{tp_3s} / Z_{tp_3s} +R_1). Both of the following expressions have direct effect on PTE and PDL. Therefore, to better illustrate the effect of ($k_{23}^2 Q_2 Q_3$), PTE and PDL of the conventional three coil design have been plotted by using Eq. (3.36) and (3.37) with respect to K_{12} and K_{23}

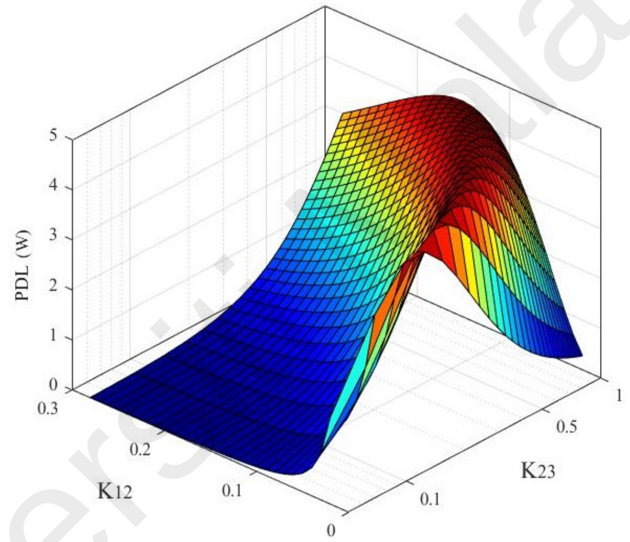

(a)

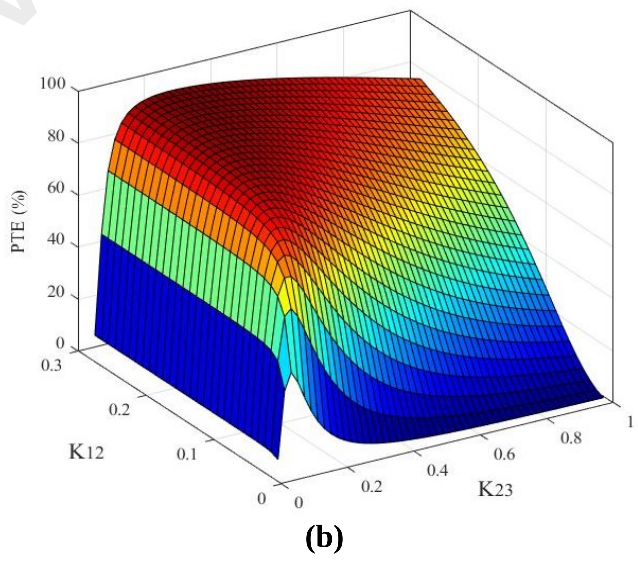

(b)

Figure 4.4: Power delivery to load and (b) efficiency of S-S-S system with respect to K_{12} and K_{23} where V1 =1V and R_L = 20 Ω

The maximum value of K_{12} in Fig. 4.4 is set to be in the condition where the primary coil is placed on the same axis as the transmitter coil and it can be reduces when the distance between the mentioned two coils increases. Moreover, further analysis of Fig 4.4 indicates that when $K_{12} \geq K_{23}$, the conventional S-S-S system is capable of achieving high efficiency. On the other hand, in order to maximize PDL, K_{23} must be much larger than K_{12}, which is in contrast from maximizing PTE for S-S-S system.

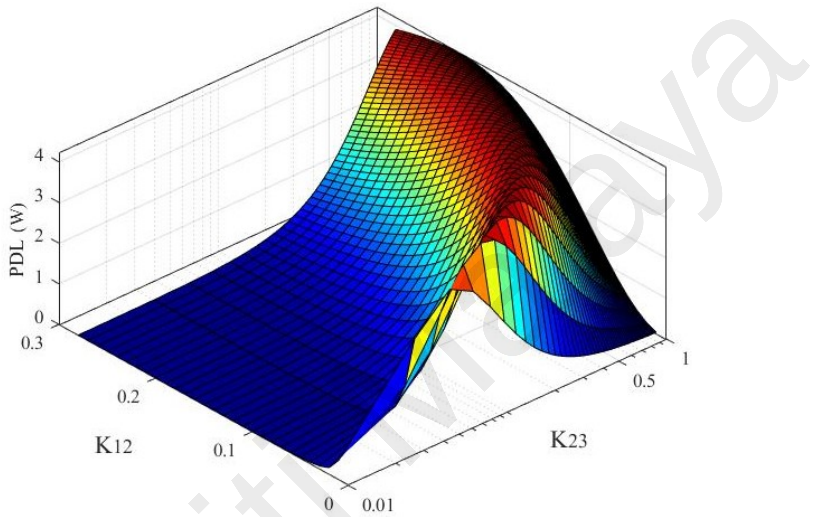

(a)

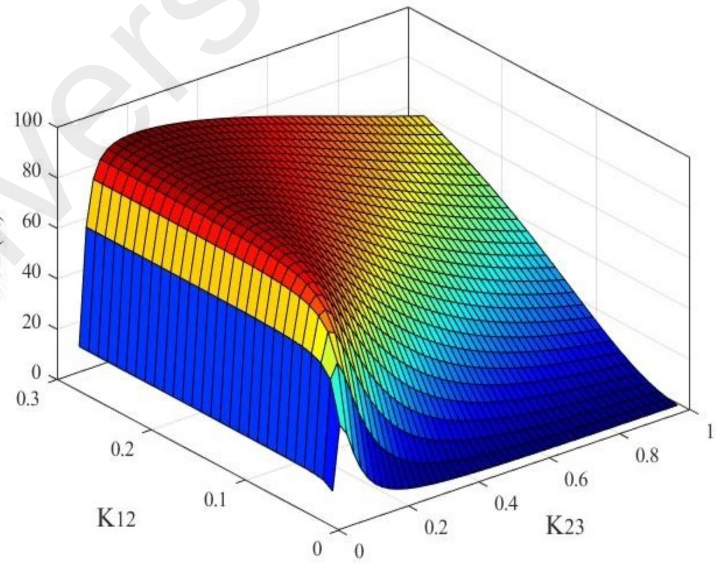

(b)

Figure 4.5:(a) PDL(b) PTE of S-S-LCLCC system with respect to K_{12} and K_{23} where V_1=1V and R_L = 20 Ω

Similar to the previous analysis PTE and PDL of the proposed S-S-LCLCC system with respect to variation of coupling coefficient and quality factor has been plotted in Fig 4.5.

Fig 4.5 shows alike to the conventional design, PDL of S-S-LCLCC system is maximized when K_{23} is larger than K_{12}. Therefore, the similar issue still exists in the new system. However, when $K_{12} \geq K_{23}$ (where both system can achieve high PTE), the S-S-LCLCC system in comparison to conventional design can deliver more power to the load. To better illustrate this effect, Fig 4.6 is plotted. Since PTF with respect to R_L has been discussed in the previous sections, in this analysis, R_L is now constant and the input voltage is set to be the same for both systems. Moreover, K_{12} is maximized (L_1 is placed on the same plane as L_2) and only K_{23} changes in the range of $K_{23} < K_{12}$ so that both systems can achieve high efficiency. According to (J. Zhang et al., 2017), at this condition, three-coil system is capable of having higher efficiency than two-coil design. Fig 4.6 clearly proves that PTE of S-S-LCLCC is much higher than conventional S-S-S system especially when K_{23} is larger and the value of α is smaller. In addition, the efficiency of the S-S-LCLCC compensation topology is higher although lower than that of the conventional topology at higher values of K_{23}. Very similar characteristics have been reported in (W. Li et al., 2016), which indicates that the S-S-LCLCC topology is similar to double-sided LCC design in two coil system. It can perform much better when the mutual inductances between the transmitter and receiver coil is minimized. Note that in (Y. Li et al., 2018), K_{23} is only 0.095 and to make the value of K_{23} to be very large so that S-S-S can have higher efficiency than the proposed S-S-LCLCC system, it is required to use magnetic core materials such as ferrite or to increase the size and the number of turns of the receiver coil. In consequences of that, K_{13} also becomes larger and this makes the value of M_{13} not to be close to zero anymore, which eventually leads the system to loses its ZPA characteristics. Nevertheless, by assuming K_{23} >0.2 while minimizing M_{13}

is possible even in that condition, the PDL of S-S-LCLCC will be much higher than the conventional topology. Therefore, it is clear that using S-S-LCLCC instead of S-S-S system for achieving CV while adopting the coil design in (Y. Li et al., 2018) is more beneficial.

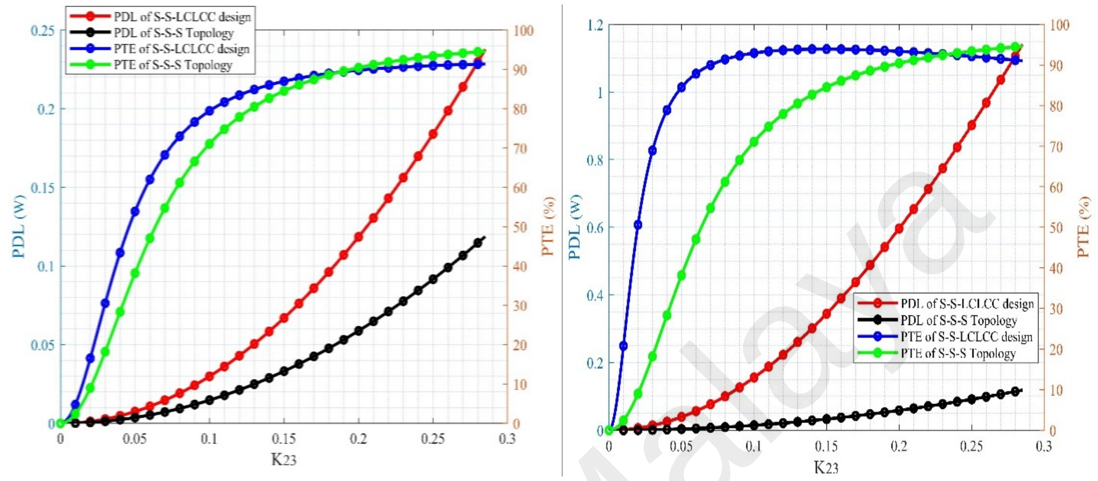

(a) **(b)**

Figure 4.6: PDL and PTE of S-S-S and S-S-LCLCC System

PTE in terms of coupling coefficient has been discussed in detail when all the quality factors remain the same as the study in (Y. Li et al., 2018) , however, in order to have fair analysis it is crucial to investigate the effect of PTE as the coil quality factors changes. Varying the coil quality factors can be done by changing the value of inductance and the internal resistance of each coil. However, the presence of R_L in Q_3 equation makes the denominator of the receiver coil quality factor to be large. Duo to the mentioned reason, R_3 has a negligible effect in Q_3 performance, therefore, the only other two parameters which are capable of incasing the Q_3 are ω and L_3. Despite, increasing operating angular frequency is considered one of the main factors and it may contribute to the value of Q_3 increases but it is not considered a good option because in WPT application the operating frequency is limited around 85Khz only. Another approach is to increase the size and the number of turns in the receiver coil. However, this is also hard to achieve when the transmission distance (Td) remains the same as before. Because as L_3 becomes larger, M_{13}

increases as well. As a consequence of that, the value of M_{13} will not be close to zero anymore and eventually, both systems lose their ZPA characteristics. Moreover, it is in contrast with first the assumption in (Y. Li et al., 2018) where M_{13} must be close to Zero. This indicates that if T_d does not increase , all the options which lead the value of Q_3 increases will make the first assumption in (Y. Li et al., 2018)to be not valid anymore. Therefore, from Eq. (3.36) and (3.40), the PTE of both topologies have been investigated with respect to the quality factor under two different conditions. Where in the first condition, Q_3 and T_d will remain the same as the study (Y. Li et al., 2018) and only Q_1 and Q_2 changes as it is presented in Fig 4.7. In the second condition, Q_1 and Q_2 vary again but this time L_3 increases to be as large as L_2 so that the value of Q_3 becomes much larger to provide the wider Q factor analysis as shown in Fig 4.8. In addition, Since L_3 becomes much larger, ANSYS software has been used to calculate the appropriate transmission distance so that the value of M_{13} still remains close to zero. Therefore, in this analysis, the value of K_{23} is getting smaller due to increasing the transmission distance. All the other parameters remain the same as (Y. Li et al., 2018).

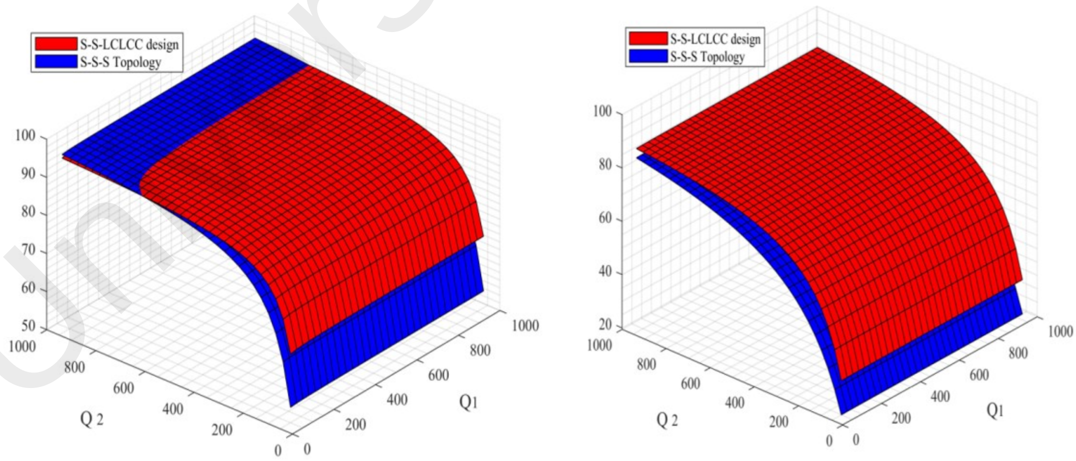

(a) (b)

Figure 4.7: PTE of both topologies with respect to quality factor, where L3 =38.29 μH , K23 = 0.095 at (a). RL=20Ω (b) RL=100Ω

The results in Fig 4.7 clearly shows that if the quality factor of the relay coil gets very large for small value of R_L the conventional system can perform better, however, for the large value of R_L regardless of the value of Q_1 and Q_2 , the PTE of S-S-LCLCC system is still much better than the conventional Topology. On the other hand, analysis of Fig 4.8 indicates that the new S-S-LCLCC has higher efficiency than the conventional system when Q_3 and Td get larger for both large and even small value of R_L. This is because K_{23} to the power of two in (3.36) and (3.40) has a stronger influence on PTE of both topologies in comparison to Q_3. Moreover, as it is presented in Fig 4.6 the new system performs much better when the coupling coefficient between relay and receiver coil is minimized and these results agree well with the results obtained and presented in Fig 4.7. Therefore, even in the case of using a similar coil design as the study in (J. Zhang et al., 2017) the proposed new system is capable of significantly improve PTE in comparison to the conventional topology.

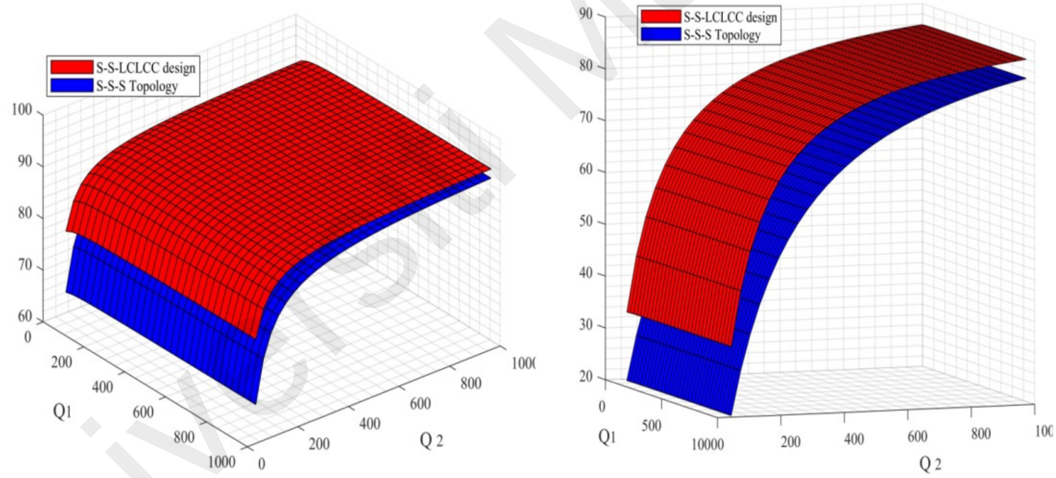

(a) **(b)**

Figure 4.8: PTE of both topologies with respect to quality factor, where R2=R3, L3 =165.39µH, K23 = 0.045 at (a). RL=10Ω (b) RL=100Ω

4.5 Quality Factor Analysis Under Wide Variation

Eq. (3.38) and (3.40) clearly show that the efficiency formula of both conventional and the new designs is very similar. The only three parameters that differentiate these two equations are Q_3, Q_n, and the receiver efficiency. Moreover, (Q_3= ωL_3/ (R_3+R_L)) and (Q_n=ωL_3/Re(Z_r)) are much smaller than (Q_1= $\omega L_1/R_1$) and (Q_2= $\omega L_2/R_2$) for both topologies due to the presence of R_L in the denominator of their equations. This indicates that R$_L$ can significantly change the value of Q_3, Q_n and the system efficiency as it is varying. Moreover, K_{12} and K_{23} are also considered very important factors and they are capable of varying efficiency performance of both systems. Therefore, the value of R$_L$, K_{12} and K_{23} have been fixed in all the provided figures so it is possible to plot efficiency characteristics based on the changes in quality factors only.

The resonant frequency is often constant in the WPT application, therefore, varying Q_1 and Q_2 can be done by changing L_1, L_2, R$_1$ and R$_2$ which eventually allowing the system to have a wide range of analysis where Q_1 and Q_2 will be changing in the range of 50 to 1000. On the other hand, to increase the value of Q_3 and Q_n it is easier to increase the value L_3 rather than reducing the value of R$_3$. This is because R$_L$ is much larger than R$_3$ and decreasing R$_3$ will have a slight effect on (R$_3$+R$_L$). Therefore, the receiver side quality factor for both systems can be defined as (Q_3= ω (βL_3) / (R$_3$+R$_L$)) and (Q_n= ω (βL_3) / Re (Z_r)). Where (β) changes in the range of (1 to 3) so that the analyis can be conducted up to 3 times larger Q_3 than the study in (Y. Li et al., 2018). Finally, to provide a complete Q factor the analysis has been seprated into three different sections and PTE is calculated by using Eq. (3.36) and (3.40) for S-S-S and S-S-LCLCC topology, respectively.

4.5.1 Condition 1: ($50 \le Q_1 \le 1000$), ($50 \le Q_2 \le 1000$) and $a = 0.7$

In this section, only Q_1 and Q_2 changes and K_{12}, K_{23} are the same as the study in (Y. Li et al., 2018). Additionally, the value of (β) is equal to one so that Q_3 becomes the same as the mentioned study.

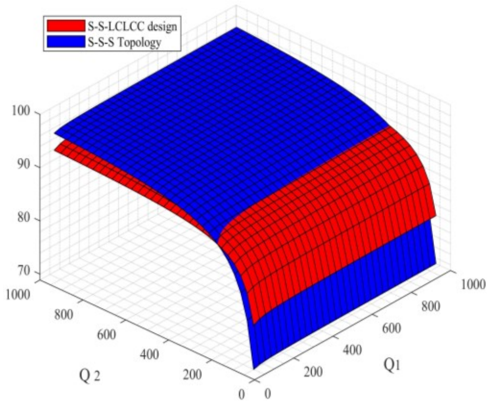

R$_L$ = 10 Ω

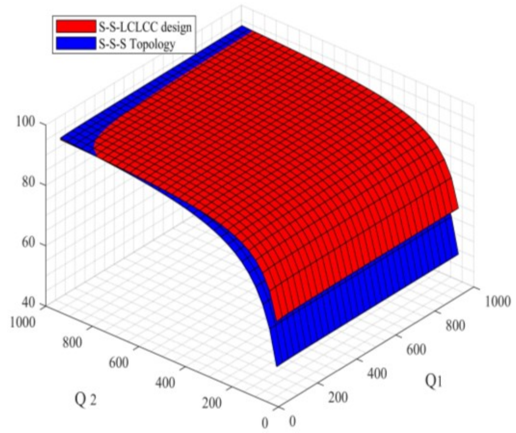

R$_L$ = 24 Ω

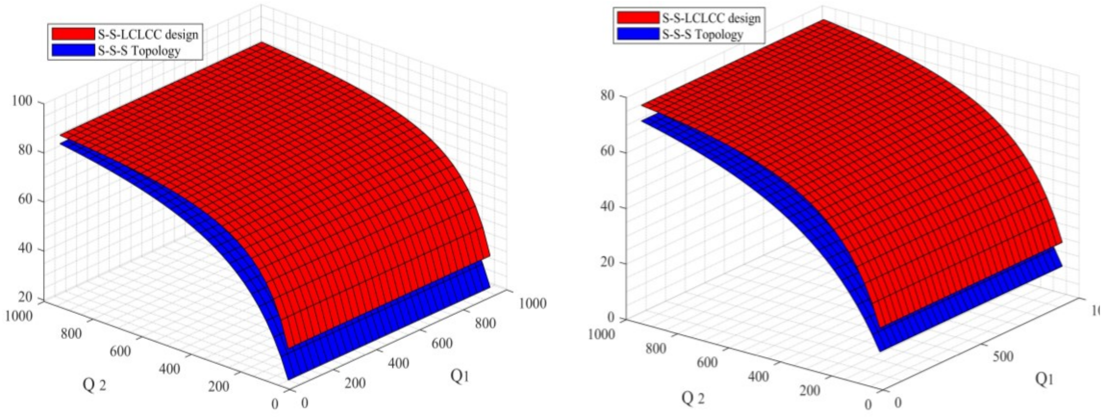

R_L = 100 Ω **R_L = 200 Ω**

Figure 4.9: Quality Factor Base on Condition 1

From the analysis of Fig. 4.9 it is clear that the efficiency performance of the S-S-LCLCC topology in comparison to the S-S-S system is much better regardless of the value of Q_1 and Q_2 when R_L is chosen to be large. However, for the small value of R_L, when the relay coil quality factor becomes large, the S-S-S system starts to perform better than the new design. It has been mentioned in the previous sections, CV mode is designed for the large value of R_L in all the recent studies (to be more specific, the study (Y. Li et al., 2018) CV mode started for R_L larger than 24 ohm). Therefore, using S-S-LCLCC topology for achieving CV is more beneficial.

4.5.2 Condition 2: ($50 \le Q_2 \le 1000$), ($1 \le \beta \le 3$) and $a = 0.7$

In this section, only Q_2, Q_3 and Q_n changes and all the other parameters are the same

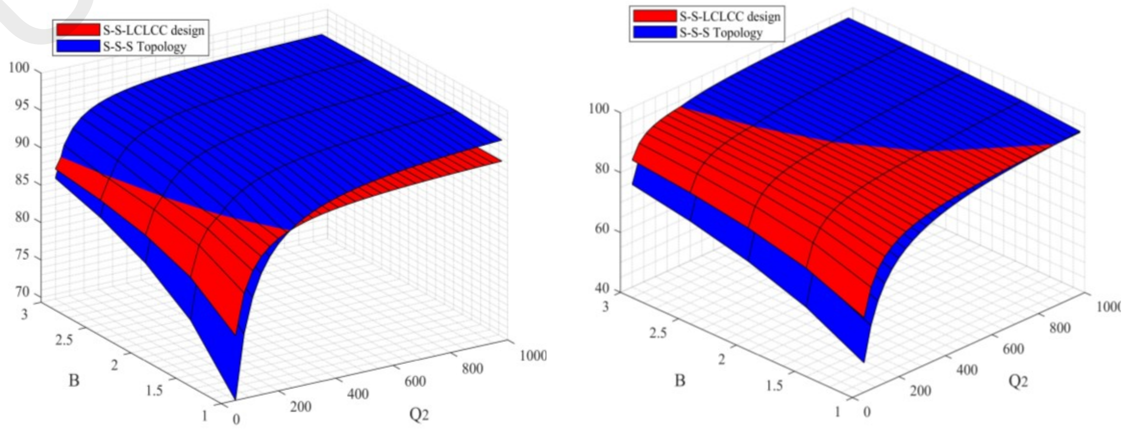

R_L = 10 Ω **R_L = 24 Ω**

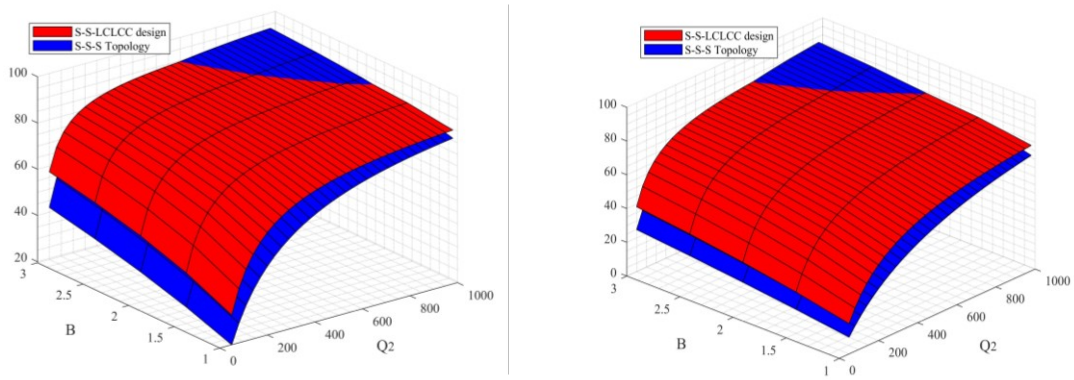

$R_L = 100\ \Omega$ $R_L = 200\ \Omega$

Figure 4.10: Quality Factor Base on Condition 2

In Condition 2 it has been shown clearly as Q_3 and Q_2 become larger, the S-S-S topology has better performance than the new design for the small value of R_L. The overall performance of the S-S-LCLCC system for the large value of R_L is still better than the conventional system but, S-S-S topology can potentially start to perform better even for the larger value of R_L as Q_2 and Q_3 become very large (almost 3 times of conventional design). However, these results can be improved for the new topology if the value of (α) decreases. This is because the receiver coil quality factor in the conventional design mainly depends on operating angular frequency and the inductance of L_3. However, Q_n in S-S-LCLCC is also related to [Re (Z_r)] as well. Additionally, the smaller value of (α) will make the magnetite of [Re (Z_r)] smaller and in consequence of that Q_n increases. This eventually leads to the performance of the system gets better for the larger value of R_L even when Q_3 becomes very large. To illustrate the effect of (α), Condition 2 has been done again by using the smaller value of (α) for R_L=100 and 200.

The results in Fig 4.11 clearly show that it is possible to redesign the S-S-LCLCC by reducing the value of (α) so that it performs much better than the conventional design for the large value of R_L even when relay and reviver coil Q factors becomes very large. A very similar analysis in Fig 4.6 has been done where the smaller value of (α) could improve the system efficiency. Also, it could significantly decrease the current across the relay coil, which may eventually lead to the coupler wire gauge and overall coupler size and the weight of the relay coil reduces. Moreover, since the voltage stress is also reduced in the relay resonant capacitors, a much lesser capacitor is required for secondary compensation compared to (Y. Li et al., 2018).

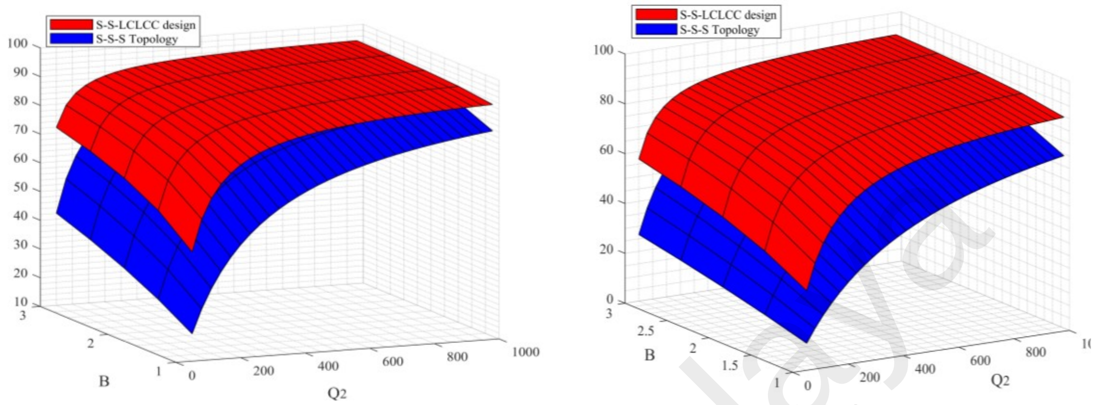

R_L = 100 Ω, α=0.5 **R_L = 100 Ω, α=0.3**

Figure 4.11: Quality Factor in Condition 2 when α Changes

4.5.3 Condition 3: ($50 \leq Q_1 \leq 1000$), ($1 \leq \beta \leq 3$) and $a = 0.7$

In this section, only $Q1$, $Q3$ and Qn changes and all the other parameters remain the same as well. Analysis of Condition 3 indicates that the S-S-S system is still far better than the new design for the small value of RL regardless of the value of $Q3$ and $Q1$. However, similar to Condition 1, the S-S-LCLCC system starts to perform much better as RL becomes larger, as can be witnessed from the blow figures.

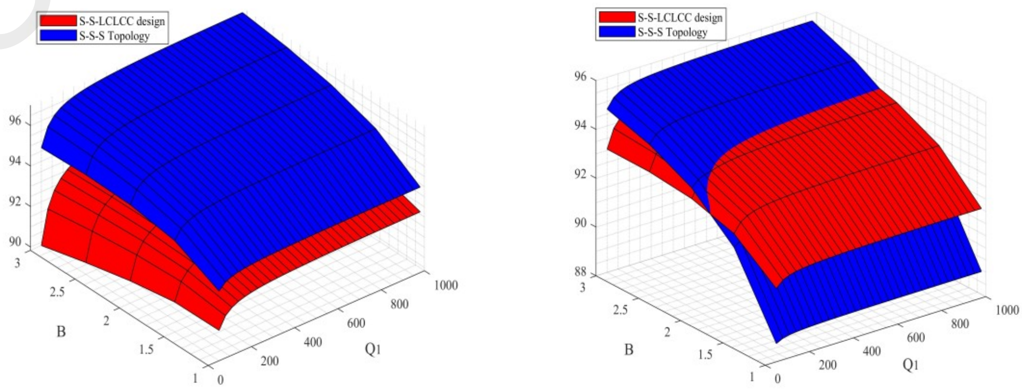

R_L = 10 Ω **. R_L = 24 Ω**

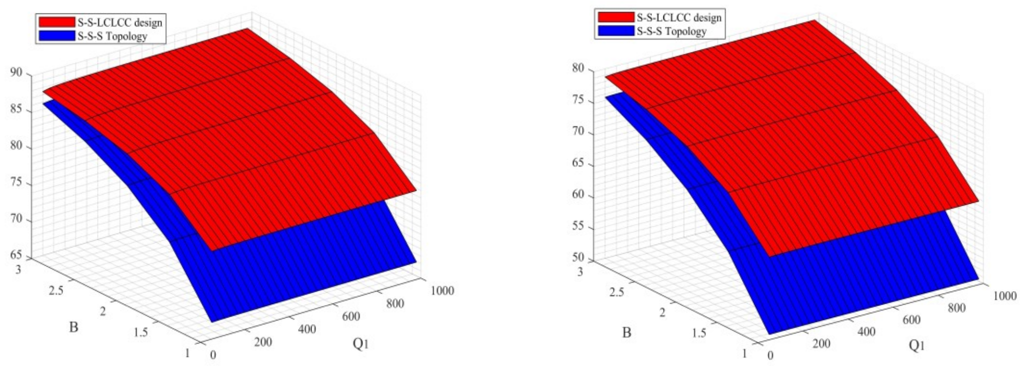

. $R_L = 100\ \Omega$ $R_L = 200\ \Omega$

Figure 4.12: Quality Factor Base on Condition 3

Therefore, it can be concluded that the overall performance of the new S-S-LCLCC topology for the larger value of the load resistance is much better than the conventional design in all the sections.

Nevertheless, implementing Condition 2 and 3 is hardly possible because in order to make Q_3 three times larger, it is required operating angular frequency increases and the inductance of the receiver coil becomes larger as well. Increasing frequency up to 600 kHz so that Q_3 can become large enough is not considered a good choice in practical application since the standard operating frequency for WPT application is limited and it is around 85 kHz only. Another approach is to significantly increase the inductance of L_3 so that the conventional S-S-S system becomes more efficient than the proposed new design, however, this is also hardly possible in practical WPT applications because by making L_3 much larger M_{13} also becomes large as well. In consequence of that, the first assumption in (Y. Li et al., 2018) where M_{13} must be equals to zero is also not valid anymore. Therefore, section 1 is the only practical section. It is worth mentioning that in section 1 the performance of S-S-LCLCC is much better than the conventional S-S-S topology and that is why it is preferable to use the new design to achieve CV mode. A similar conclusion had been made in Fig 4.3 where the new S-S-LCLCC compensation circuit starts to perform much better when the value of R_L is getting larger and larger.

Additionally, in order to present a more practical analysis for Condition 2 and 3, transmission distance had been increased as the value of Q_3 increases so that M_{13} still remains close to zero. This has been done by using ANSYS as shown in Fig. 4.13.

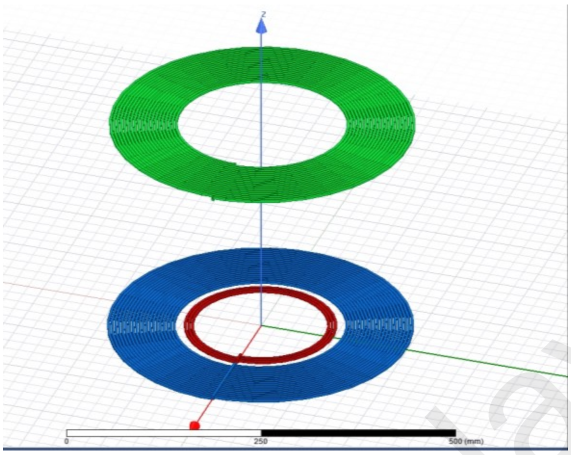

L_3 =165.39μH, K_{23} = 0.045, Td=330mm

Figure 4.13: ANSYS simulation of transmitter and receiver coils

Analysis of the above coil is presented in Fig 4.8. Note that this type for three coil designs where both relay and receiver coil are large have been used in (J. Zhang et al., 2017) as well and it is proven the performance of three coil systems is far better than two coil design. Analysis in the Fig 4.8 clearly shows the new S-S-LCLCC have higher efficiency than the conventional system when Q_3 and Td get large for both large and even small value of R_L, therefore, achieving CV mode, in the case of using the coil design in (J. Zhang et al., 2017) instead of study (Y. Li et al., 2018) , the new S-S-LCLCC system is still capable of providing significantly better results in comparison to conventional compensation topology.

4.6 Simulation of input impedance versus misalignment

Analysis of Eq. (3.43) shows that the input current in both conventional and the proposed new system decrease in the case of misalignment. This phenomenal can be proven from another approach. Based on Table 3.2 and Eq. (3.17), as ZM_{23} reduces, the equivalent input impedance will increase, as shown in Fig 4.14. Therefore, the input current of both systems decreases. Fig 4.14 also indicates that the input current of S-S-LCLCC system decreases more rapidly while delivering the same amount of output power as conventional design. Note that the input voltage of S-S-S is 1.42 times larger than S-S-LCC design in Eq. (3.11). For this reason, the input current in S-S-S topology is smaller when both systems deliver the same output power. However, as M_{23} decreases, the input current of S-S-LCLCC system tends to be closer as S-S-S input current. Since the voltage across the S-S-LCLCC is 0.7 times of the conventional design, S-S-LCLCC requires less input power for delivering the same amount of output power. In other words, the S-S-LCLCC design has less energy losses than S-S-S design when ZM_{23} decreases. This characteristic can be witnessed clearly in Fig 4.15, especially for larger values of equivalent load resistance of the battery, which is the main operation area of CV mode.

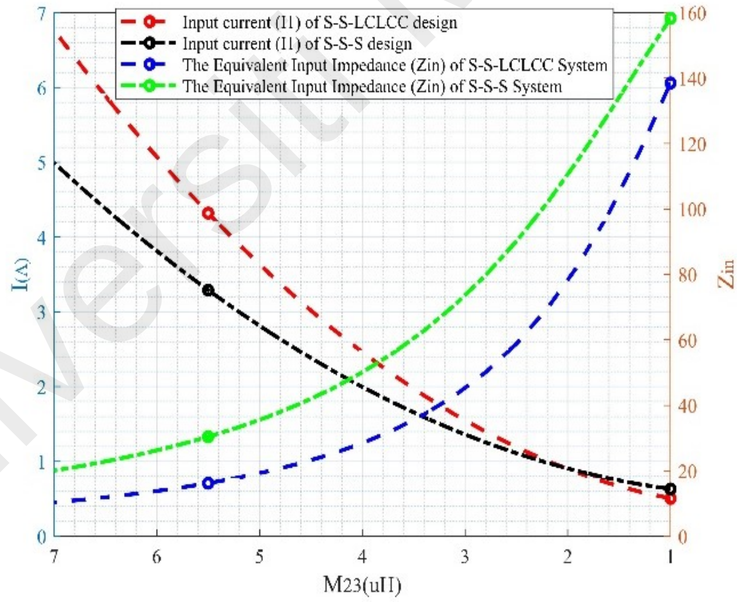

Figure 4.14: Simulated Equivalent Input impedance and Input current of S-S-S and S-S-LCLCC with respect to M23

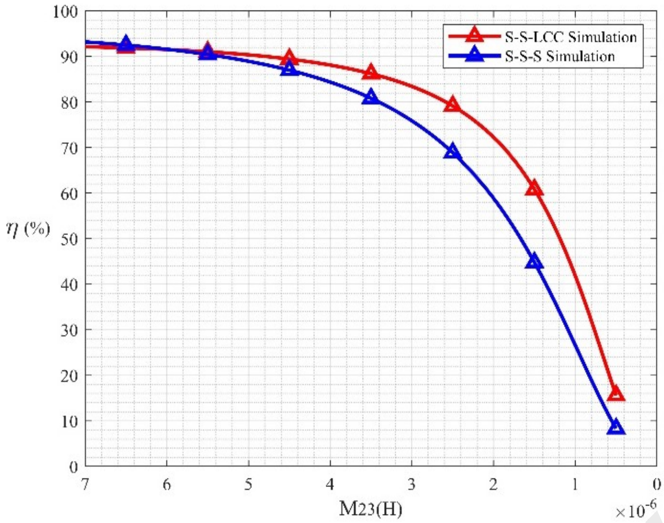

(a)

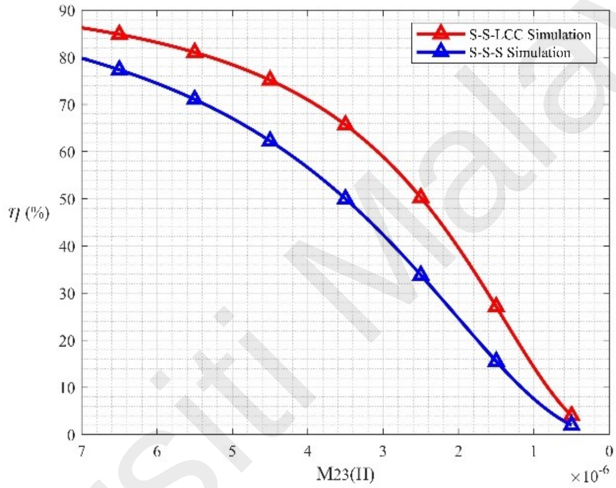

(b)

Figure 4.15 :. Power efficiency of the S-S-S and S-S-LCLCC system with respect to M23 at (a). RL=10Ω (b) RL=40Ω

4.7 Experimental measurement and waveforms

From the DC power supply, the power is transferred to the H-bridge inverter with the operating frequency of 200 kHz, the resonator, rectifier and eventually to the DC load, which acts like a battery charger. In the proposed system, four MOSFETs (C2M0080120D) with 80 mΩ Rds on and fast recovery diodes (DSEI2X101-06A) are used for the inverter and rectifier respectively. The waveforms are taken by using Tek DPO3014 oscilloscope. For the measurement of power efficiency, YOKOGAWA WT500 power analyzer is used. The experimental waveforms of the voltage, input current and output voltage in the constant voltage mode when the load is at 24 Ω and 48 Ω are shown in Fig. 4.16

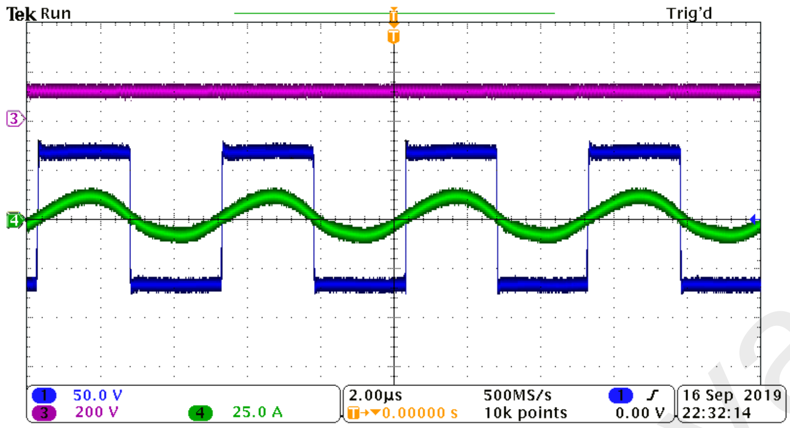

(a)

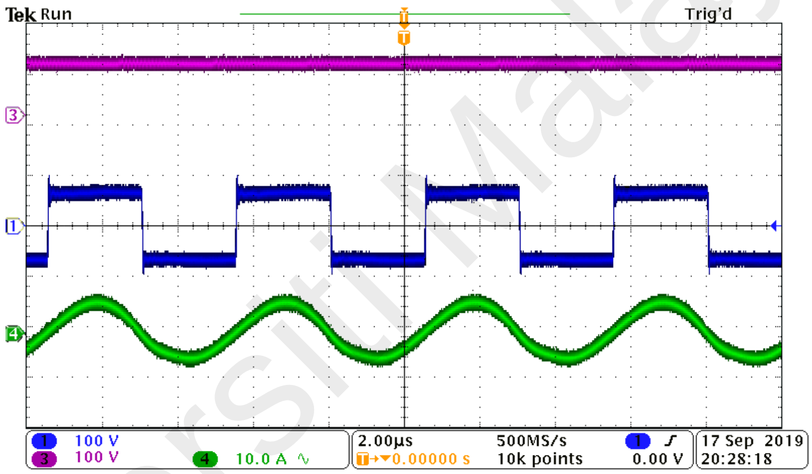

. (b)

Figure 4.16: ExperimentalMeasurements of waveforms on CV mode at (a). RL=24Ω (b) RL=48Ω

The S-S-LCLCC current is almost in phase with the input voltage and the system can nearly achieve ZPA while operating in CV mode. The same characteristics can be seen in the conventional design, which is supporting the theoretical analysis. A slight change of the output voltage as can be seen in Fig. 4.17 is caused by not purely resonance of the system and the slight effect of *M*13, which has been assumed to be zero in the theoretical analysis. Since the increment of the output voltage is less than 2% at about 100V, the proposed design is acceptable and it can be further improved by designing a new coil with better resonance capacitor compensation and smaller M_{13}

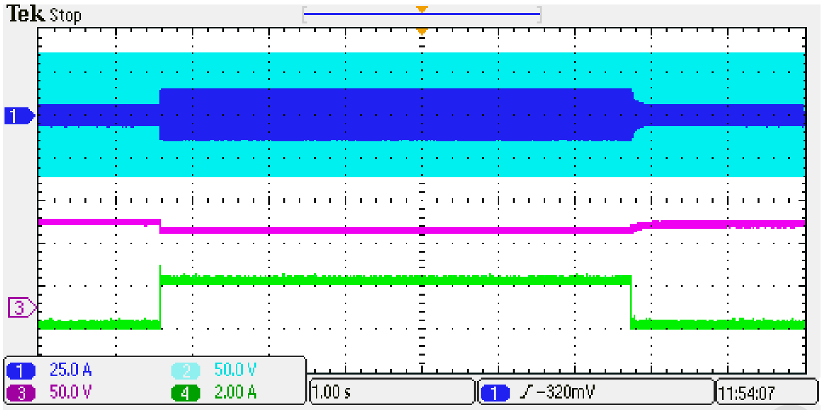

Figure 4.17:CV Waveform when sudden RL changes from48 Ω to 24 Ω and changes back to 48 Ω.

The measurement and simulation of the efficiency of both conventional and new systems at different loads are shown in Fig 4.18. In S-S-LCLCC, the additional capacitor helps the system maximum efficiency to occur at 14.2 Ω while the conventional maximum efficiency appears at 7 Ω. It is also possible to further shift the maximum efficiency of S-S-LCLCC to closer to 24 Ω without redesigning the coils structure and by only using smaller C_{3p}/C_{1p} ratio. However, since one of the main objectives of this work is to use smaller L_{1p}, L_{3p} and due to the mentioned analysis in section V, the ratio of C_{3p}/C_{1p} has been chosen to be 0.7. Nevertheless, the S-S-LCLCC for loads larger than

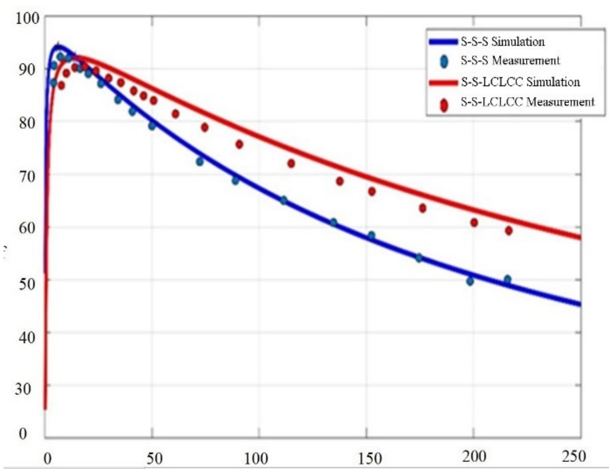

Figure 4.18: Measurements and Simulation of both Conventional and New Design with Respect to Load

24 Ω, which is the starting point of the operation of CV mode in (Y. Li et al., 2018), has higher efficiency. Also, when the load reaches 222 Ω, the efficiency of the new system becomes more significant and it has approximately 10% higher efficiency than the conventional design.

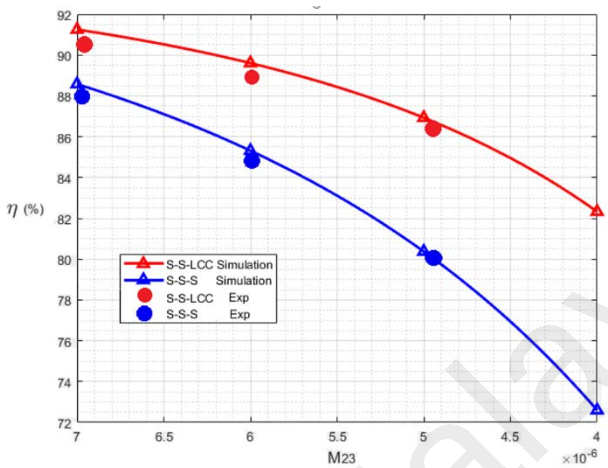

Figure 4.19:Measurements and Simulation of Both Conventional and New Design when the M23Changing duo to misalignment

The experimental measurement at different mutual inductances due to the misalignment affect at 24 Ω is shown in Fig 4.19, which further proves the superior performance of the newly proposed design at larger equivalent load resistance of the battery when misalignment occurs. The maximum efficiency of the new design reaches to 91.2% at 14.2 Ω and 89.6 % at 24 Ω while delivering 420W power. The measurement efficiency is slightly lower than the calculated values but the overall performance of the system has very similar trend as the theoretical and simulation results. For better comparison, both conventional and new designs are delivering the same amount of output power at approximately 100V output voltage.

In this section, to summarize some of the improvements compared to conventional S-S-S design (Y. Li et al., 2018), Table 4.1 has been plotted.

Table 4.1: Comparison Table between the Proposed S-S-LCLCC Topology and the Conventional S-S-S System (Y. Li et al., 2018)

Voltage stress across the secondary coil	S-S-LCLCC has lesser Voltage stress and requires lesser capacitance (reduces the cost)
Maximum efficiency	S-S-S has higher maximum efficiency than S-S-LCLCC topology
Efficiency stability in CV mode	S-S-LCLCC Effiteicny stability is much better than the Conventional S-S-S
An additional controller for input current	Unlike S-S in two coil system, Both systems do not require an additional controller
Misalignment performance	S-S-LCLCC has much better misalignment performance for higher load resistances
Power delivery to load	S-S-LCLCC design can transfer much more power, especially when the coupling coefficient increases

CHAPTER 5: CONCLUSIONS AND FUTURE WORK

5.1 Conclusions

In this work, three-coil S-S-S and S-S-LCLCC WPT topologies have been successfully compared and analyzed theoretically and experimentally. Moreover, simplified models of S-S-LCLCC has been successfully proposed to demonstrate the advantages of this new design. The benefits of S-S-LCLCC compared to the conventional design system are significant improvement of power efficiency at larger values of equivalent load resistance of the battery, reducing energy losses in the case of misalignment, reducing the voltage stress across the relay coil and shifting the optimum value of load resistance to the operating range of CV. Thus, the proposed system can achieve its maximum efficiency. Moreover, additional capacitors contribute to control of the voltage gain of the system together with the mutual inductances, frequency. Although the S-S-S topology has higher maximum efficiency due to having less components, in the case of using two-switch technique, which contributes the system to operate both in CC and CV mode with ZPA, the system cannot achieve its maximum efficiency at CV mode for small coil designs as in (Y. Li et al., 2018). However, the S-S-LCLCC design is capable of shifting its maximum efficiency to the desired equivalent battery load resistance. To validate the superior performance of S-S-LCLCC WPT of three-coil designs, calculation, simulation, simplification and experimental results have been successfully conducted for CV mode for only small coil design for both conventional S-S-S and new S-S-LCLCC design.

5.2 Future work

In this project, the advantages of multiple coils in comparison to the conventional two-coil system have been pointed out and it has been shown that three-coil system under some specified condition can outperform two-coil system. In the recent work, it has been shown that three coil systems can be used as resonant repeaters and can increase the transfer power as well. However, in this work, the primary coil and secondary coil have been placed in the same axis and the system does entirely used the concept of resonant repeaters. In future work, each coil can be optimized according to the concept of the resonant repeater to further improve the transfer power. Moreover, CC characteristics of the proposed S-S-LCLCC have not been discussed. Therefore, in future work, S-S-LCLCC design combined with S-S-LCC topology, which is capable of realizing CV and CC respectively, will be implemented by using the hybrid two-switch technique to investigate the performance of S-S-LCLCC and its effect on the S-S-LCC in the CC mode.

REFERENCES

Ahn, D., & Hong, S. (2013). A Study on Magnetic Field Repeater in Wireless Power Transfer. *IEEE Transactions on Industrial Electronics, 60*(1), 360-371. doi:10.1109/TIE.2012.2188254

Ahn, S., Pak, J., Song, T., Lee, H., Byun, J. G., Kang, D., . . . Kim, J. (2010, 25-30 July 2010). *Low frequency electromagnetic field reduction techniques for the On-Line Electric Vehicle (OLEV).* Paper presented at the 2010 IEEE International Symposium on Electromagnetic Compatibility.

Bandyopadhyay, S., Prasanth, V., Bauer, P., & Ferreira, J. A. (2016, 27-29 June 2016). *Multi-objective optimisation of a 1-kW wireless IPT systems for charging of electric vehicles.* Paper presented at the 2016 IEEE Transportation Electrification Conference and Expo (ITEC).

Bandyopadhyay, S., Venugopal, P., Dong, J., & Bauer, P. (2019). Comparison of Magnetic Couplers for IPT-Based EV Charging Using Multi-Objective Optimization. *IEEE Transactions on Vehicular Technology, 68*(6), 5416-5429. doi:10.1109/TVT.2019.2909566

Bojarski, M., Asa, E., Colak, K., & Czarkowski, D. (2017). Analysis and Control of Multiphase Inductively Coupled Resonant Converter for Wireless Electric Vehicle Charger Applications. *IEEE Transactions on Transportation Electrification, 3*(2), 312-320. doi:10.1109/TTE.2016.2566921

Bosshard, R., Iruretagoyena, U., & Kolar, J. W. (2016). Comprehensive Evaluation of Rectangular and Double-D Coil Geometry for 50 kW/85 kHz IPT System. *IEEE Journal of Emerging and Selected Topics in Power Electronics, 4*(4), 1406-1415. doi:10.1109/JESTPE.2016.2600162

Bosshard, R., & Kolar, J. W. (2016a). Inductive power transfer for electric vehicle charging: Technical challenges and tradeoffs. *IEEE Power Electronics Magazine, 3*(3), 22-30. doi:10.1109/MPEL.2016.2583839

Bosshard, R., & Kolar, J. W. (2016b). Multi-Objective Optimization of 50 kW/85 kHz IPT System for Public Transport. *IEEE Journal of Emerging and Selected Topics in Power Electronics, 4*(4), 1370-1382. doi:10.1109/JESTPE.2016.2598755

Bosshard, R., Kolar, J. W., Mühlethaler, J., Stevanović, I., Wunsch, B., & Canales, F. (2015). Modeling and $\eta $ - $\alpha $ -Pareto Optimization of Inductive Power Transfer Coils for Electric Vehicles. *IEEE Journal of Emerging and Selected*

Topics in Power Electronics, 3(1), 50-64. doi:10.1109/JESTPE.2014.2311302

Bosshard, R., Mühlethaler, J., Kolar, J. W., & Stevanović, I. (2013, 17-21 March 2013). *Optimized magnetic design for inductive power transfer coils.* Paper presented at the 2013 Twenty-Eighth Annual IEEE Applied Power Electronics Conference and Exposition (APEC).

Budhia, M., Boys, J. T., Covic, G. A., & Huang, C. (2013). Development of a Single-Sided Flux Magnetic Coupler for Electric Vehicle IPT Charging Systems. *IEEE Transactions on Industrial Electronics, 60*(1), 318-328. doi:10.1109/TIE.2011.2179274

Budhia, M., Covic, G., & Boys, J. (2010, 7-10 Nov. 2010). *A new IPT magnetic coupler for electric vehicle charging systems.* Paper presented at the IECON 2010 - 36th Annual Conference on IEEE Industrial Electronics Society.

Budhia, M., Covic, G. A., & Boys, J. T. (2011). Design and Optimization of Circular Magnetic Structures for Lumped Inductive Power Transfer Systems. *IEEE Transactions on Power Electronics, 26*(11), 3096-3108. doi:10.1109/TPEL.2011.2143730

Choi, S. Y., Gu, B. W., Jeong, S. Y., & Rim, C. T. (2015). Advances in Wireless Power Transfer Systems for Roadway-Powered Electric Vehicles. *IEEE Journal of Emerging and Selected Topics in Power Electronics, 3*(1), 18-36. doi:10.1109/JESTPE.2014.2343674

Choi, S. Y., Gu, B. W., Lee, S. W., Lee, W. Y., Huh, J., & Rim, C. T. (2014). Generalized Active EMF Cancel Methods for Wireless Electric Vehicles. *IEEE Transactions on Power Electronics, 29*(11), 5770-5783. doi:10.1109/TPEL.2013.2295094

Chopra, S., & Bauer, P. (2013). Driving Range Extension of EV With On-Road Contactless Power Transfer—A Case Study. *IEEE Transactions on Industrial Electronics, 60*(1), 329-338. doi:10.1109/TIE.2011.2182015

Chwei-Sen, W., Covic, G. A., & Stielau, O. H. (2001, 29 Nov.-2 Dec. 2001). *General stability criterions for zero phase angle controlled loosely coupled inductive power transfer systems.* Paper presented at the IECON'01. 27th Annual Conference of the IEEE Industrial Electronics Society (Cat. No.37243).

Chwei-Sen, W., Stielau, O. H., & Covic, G. A. (2005). Design considerations for a contactless electric vehicle battery charger. *IEEE Transactions on Industrial Electronics, 52*(5), 1308-1314. doi:10.1109/TIE.2005.855672

Conductix-Wampfler. (2013). Charging Electric Buses Quickly and Efficiently: Bus

Stops Fitted With Modular Components Make 'Charge & Go' Simple to Implement. Retrieved from http://www.conductix.us/en/news/2013-05-29/charging-electric-buses

Covic, G. A., & Boys, J. T. (2013). Modern Trends in Inductive Power Transfer for Transportation Applications. *IEEE Journal of Emerging and Selected Topics in Power Electronics, 1*(1), 28-41. doi:10.1109/JESTPE.2013.2264473

Covic, G. A., Kissin, M. L. G., Kacprzak, D., Clausen, N., & Hao, H. (2011, 17-22 Sept. 2011). *A bipolar primary pad topology for EV stationary charging and highway power by inductive coupling.* Paper presented at the 2011 IEEE Energy Conversion Congress and Exposition.

Dai, J., & Ludois, D. C. (2015). A Survey of Wireless Power Transfer and a Critical Comparison of Inductive and Capacitive Coupling for Small Gap Applications. *IEEE Transactions on Power Electronics, 30*(11), 6017-6029. doi:10.1109/TPEL.2015.2415253

Esteban, B., Sid-Ahmed, M., & Kar, N. C. (2015). A Comparative Study of Power Supply Architectures in Wireless EV Charging Systems. *IEEE Transactions on Power Electronics, 30*(11), 6408-6422. doi:10.1109/TPEL.2015.2440256

Feng, H., Cai, T., Duan, S., Zhang, X., Hu, H., & Niu, J. (2018). A Dual-Side-Detuned Series–Series Compensated Resonant Converter for Wide Charging Region in a Wireless Power Transfer System. *IEEE Transactions on Industrial Electronics, 65*(3), 2177-2188. doi:10.1109/TIE.2017.2745455

Feng, H., Cai, T., Duan, S., Zhao, J., Zhang, X., & Chen, C. (2016). An LCC-Compensated Resonant Converter Optimized for Robust Reaction to Large Coupling Variation in Dynamic Wireless Power Transfer. *IEEE Transactions on Industrial Electronics, 63*(10), 6591-6601. doi:10.1109/TIE.2016.2589922

Feng, H., Tavakoli, R., Onar, O. C., & Pantic, Z. (2020). Advances in High-Power Wireless Charging Systems: Overview and Design Considerations. *IEEE Transactions on Transportation Electrification, 6*(3), 886-919. doi:10.1109/TTE.2020.3012543

Fisher, T. M., Farley, K. B., Gao, Y., Bai, H., & Tse, Z. T. H. (2014). Electric vehicle wireless charging technology: a state-of-the-art review of magnetic coupling systems. *Wireless Power Transfer, 1*(2), 87-96. doi:10.1017/wpt.2014.8

Galigekere, V. P., Pries, J., Onar, O. C., Su, G., Anwar, S., Wiles, R., . . . Wilkins, J. (2018, 23-27 Sept. 2018). *Design and Implementation of an Optimized 100 kW*

Stationary Wireless Charging System for EV Battery Recharging. Paper presented at the 2018 IEEE Energy Conversion Congress and Exposition (ECCE).

Ghahary, A., & Cho, B. H. (1992). Design of transcutaneous energy transmission system using a series resonant converter. *IEEE Transactions on Power Electronics, 7*(2), 261-269. doi:10.1109/63.136242

Guidi, G., Suul, J. A., Jenset, F., & Sorfonn, I. (2017). Wireless Charging for Ships: High-Power Inductive Charging for Battery Electric and Plug-In Hybrid Vessels. *IEEE Electrification Magazine, 5*(3), 22-32. doi:10.1109/MELE.2017.2718829

Hao, H., Covic, G. A., & Boys, J. T. (2014). An Approximate Dynamic Model of LCL-T-Based Inductive Power Transfer Power Supplies. *IEEE Transactions on Power Electronics, 29*(10), 5554-5567. doi:10.1109/TPEL.2013.2293138

Ho, S. L., Wang, J., Fu, W. N., & Sun, M. (2011). A Comparative Study Between Novel Witricity and Traditional Inductive Magnetic Coupling in Wireless Charging. *IEEE Transactions on Magnetics, 47*(5), 1522-1525. doi:10.1109/TMAG.2010.2091495

Hou, J., Chen, Q., Wong, S., Tse, C. K., & Ruan, X. (2015). Analysis and Control of Series/Series-Parallel Compensated Resonant Converter for Contactless Power Transfer. *IEEE Journal of Emerging and Selected Topics in Power Electronics, 3*(1), 124-136. doi:10.1109/JESTPE.2014.2336811

Hui, S. Y. R., Zhong, W., & Lee, C. K. (2014). A Critical Review of Recent Progress in Mid-Range Wireless Power Transfer. *IEEE Transactions on Power Electronics, 29*(9), 4500-4511. doi:10.1109/TPEL.2013.2249670

Jeong, S., Jang, Y. J., & Kum, D. (2015). Economic Analysis of the Dynamic Charging Electric Vehicle. *IEEE Transactions on Power Electronics, 30*(11), 6368-6377. doi:10.1109/TPEL.2015.2424712

Jeong, S. Y., Choi, S. Y., Sonapreetha, M. R., & Rim, C. T. (2015, 5-6 June 2015). *DQ-quadrature power supply coil sets with large tolerances for wireless stationary EV chargers.* Paper presented at the 2015 IEEE PELS Workshop on Emerging Technologies: Wireless Power (2015 WoW).

Kamineni, A., Covic, G. A., & Boys, J. T. (2015). Analysis of Coplanar Intermediate Coil Structures in Inductive Power Transfer Systems. *IEEE Transactions on Power Electronics, 30*(11), 6141-6154. doi:10.1109/TPEL.2014.2378733

Kan, T., Lu, F., Nguyen, T., Mercier, P. P., & Mi, C. C. (2018). Integrated Coil Design for EV Wireless Charging Systems Using LCC Compensation Topology. *IEEE Transactions on Power Electronics, 33*(11), 9231-9241. doi:10.1109/TPEL.2018.2794448

Kazimierczuk, M. K., & Sekiya, H. (2009, 20-24 Sept. 2009). *Design of AC resonant inductors using area product method.* Paper presented at the 2009 IEEE Energy Conversion Congress and Exposition.

Keeling, N. A., Covic, G. A., & Boys, J. T. (2010). A Unity-Power-Factor IPT Pickup for High-Power Applications. *IEEE Transactions on Industrial Electronics, 57*(2), 744-751. doi:10.1109/TIE.2009.2027255

Khaligh, A., & Dusmez, S. (2012). Comprehensive Topological Analysis of Conductive and Inductive Charging Solutions for Plug-In Electric Vehicles. *IEEE Transactions on Vehicular Technology, 61*(8), 3475-3489. doi:10.1109/TVT.2012.2213104

Kiani, M., Jow, U., & Ghovanloo, M. (2011). Design and Optimization of a 3-Coil Inductive Link for Efficient Wireless Power Transmission. *IEEE Transactions on Biomedical Circuits and Systems, 5*(6), 579-591. doi:10.1109/TBCAS.2011.2158431

Kim, J., Son, H., Kim, K., & Park, Y. (2011). Efficiency Analysis of Magnetic Resonance Wireless Power Transfer With Intermediate Resonant Coil. *IEEE Antennas and Wireless Propagation Letters, 10*, 389-392. doi:10.1109/LAWP.2011.2150192

Kim, J. H., Lee, B., Lee, J., Lee, S., Park, C., Jung, S., . . . Baek, J. (2015). Development of 1-MW Inductive Power Transfer System for a High-Speed Train. *IEEE Transactions on Industrial Electronics, 62*(10), 6242-6250. doi:10.1109/TIE.2015.2417122

Kim, S., Covic, G. A., & Boys, J. T. (2017). Tripolar Pad for Inductive Power Transfer Systems for EV Charging. *IEEE Transactions on Power Electronics, 32*(7), 5045-5057. doi:10.1109/TPEL.2016.2606893

Kim, S., Covic, G. A., & Boys, J. T. (2018). Comparison of Tripolar and Circular Pads for IPT Charging Systems. *IEEE Transactions on Power Electronics, 33*(7), 6093-6103. doi:10.1109/TPEL.2017.2740944

Kim, S., Park, H., Kim, J., Kim, J., & Ahn, S. (2014). Design and Analysis of a Resonant Reactive Shield for a Wireless Power Electric Vehicle. *IEEE Transactions on Microwave Theory and Techniques, 62*(4), 1057-1066.

doi:10.1109/TMTT.2014.2305404

Li, S., Li, W., Deng, J., Nguyen, T. D., & Mi, C. C. (2015). A Double-Sided LCC Compensation Network and Its Tuning Method for Wireless Power Transfer. *IEEE Transactions on Vehicular Technology, 64*(6), 2261-2273. doi:10.1109/TVT.2014.2347006

Li, S., & Mi, C. C. (2015). Wireless Power Transfer for Electric Vehicle Applications. *IEEE Journal of Emerging and Selected Topics in Power Electronics, 3*(1), 4-17. doi:10.1109/JESTPE.2014.2319453

Li, W., Zhao, H., Deng, J., Li, S., & Mi, C. C. (2016). Comparison Study on SS and Double-Sided LCC Compensation Topologies for EV/PHEV Wireless Chargers. *IEEE Transactions on Vehicular Technology, 65*(6), 4429-4439. doi:10.1109/TVT.2015.2479938

Li, W., Zhao, H., Li, S., Deng, J., Kan, T., & Mi, C. C. (2015). Integrated ${LCC} $ Compensation Topology for Wireless Charger in Electric and Plug-in Electric Vehicles. *IEEE Transactions on Industrial Electronics, 62*(7), 4215-4225. doi:10.1109/TIE.2014.2384003

Li, Y., Hu, J., Lin, T., Li, X., Chen, F., He, Z., & Mai, R. (2019). A New Coil Structure and Its Optimization Design With Constant Output Voltage and Constant Output Current for Electric Vehicle Dynamic Wireless Charging. *IEEE Transactions on Industrial Informatics, 15*(9), 5244-5256. doi:10.1109/TII.2019.2896358

Li, Y., Xu, Q., Lin, T., Hu, J., He, Z., & Mai, R. (2018). Analysis and Design of Load-Independent Output Current or Output Voltage of a Three-Coil Wireless Power Transfer System. *IEEE Transactions on Transportation Electrification, 4*(2), 364-375. doi:10.1109/TTE.2018.2808698

Liu, N., & Habetler, T. G. (2015). Design of a Universal Inductive Charger for Multiple Electric Vehicle Models. *IEEE Transactions on Power Electronics, 30*(11), 6378-6390. doi:10.1109/TPEL.2015.2394734

Long, B. R., Miller, J. M., Daga, A., Schrafel, P. C., & Wolgemuth, J. (2016, 4-6 Oct. 2016). *Which way for wireless power: High Q or high k?* Paper presented at the 2016 IEEE PELS Workshop on Emerging Technologies: Wireless Power Transfer (WoW).

The Lost Journal of Nikola Tesla. (2016). Retrieved from https://www.amazon.com/Lost-Journals-Nikola-Tesla-Alternative/dp/1892062135

Lu, F., Hofmann, H., Deng, J., & Mi, C. (2015, 15-19 March 2015). *Output power and* *efficiency sensitivity to circuit parameter variations in double-sided LCC-compensated wireless power transfer system.* Paper presented at the 2015 IEEE Applied Power Electronics Conference and Exposition (APEC).

Lu, F., Zhang, H., Hofmann, H., & Mi, C. (2015). A Double-Sided LCLC-Compensated Capacitive Power Transfer System for Electric Vehicle Charging. *IEEE Transactions on Power Electronics, 30*(11), 6011-6014. doi:10.1109/TPEL.2015.2446891

Lu, F., Zhang, H., Hofmann, H., Su, W., & Mi, C. C. (2018). A Dual-Coupled LCC-Compensated IPT System With a Compact Magnetic Coupler. *IEEE Transactions on Power Electronics, 33*(7), 6391-6402. doi:10.1109/TPEL.2017.2748391

Lu, F., Zhang, H., & Mi, C. (2018). A Two-Plate Capacitive Wireless Power Transfer System for Electric Vehicle Charging Applications. *IEEE Transactions on Power Electronics, 33*(2), 964-969. doi:10.1109/TPEL.2017.2735365

Luo, Z., & Wei, X. (2018). Analysis of Square and Circular Planar Spiral Coils in Wireless Power Transfer System for Electric Vehicles. *IEEE Transactions on Industrial Electronics, 65*(1), 331-341. doi:10.1109/TIE.2017.2723867

Machnoor, M., Rodríguez, E. S. G., Kosta, P., Stang, J., & Lazzi, G. (2019). Analysis and Design of a 3-Coil Wireless Power Transmission System for Biomedical Applications. *IEEE Transactions on Antennas and Propagation, 67*(8), 5012-5024. doi:10.1109/TAP.2018.2883687

McSpadden, J. O., & Mankins, J. C. (2002). Space solar power programs and microwave wireless power transmission technology. *IEEE Microwave Magazine, 3*(4), 46-57. doi:10.1109/MMW.2002.1145675

Mohamed, A. A. S., Lashway, C. R., & Mohammed, O. (2017). Modeling and Feasibility Analysis of Quasi-Dynamic WPT System for EV Applications. *IEEE Transactions on Transportation Electrification, 3*(2), 343-353. doi:10.1109/TTE.2017.2682111

Nagendra, G. R., Covic, G. A., & Boys, J. T. (2014). Determining the Physical Size of Inductive Couplers for IPT EV Systems. *IEEE Journal of Emerging and Selected Topics in Power Electronics, 2*(3), 571-583. doi:10.1109/JESTPE.2014.2302295

Ongayo, D., & Hanif, M. (2015, 29 Nov.-2 Dec. 2015). *Comparison of circular and rectangular coil transformer parameters for wireless Power Transfer based on Finite Element Analysis.* Paper presented at the 2015 IEEE 13th Brazilian Power Electronics Conference and 1st Southern Power Electronics Conference

(COBEP/SPEC).

Pantic, Z., Bai, S., & Lukic, S. M. (2011). ZCS LCC-Compensated Resonant Inverter for Inductive-Power-Transfer Application. *IEEE Transactions on Industrial Electronics, 58*(8), 3500-3510. doi:10.1109/TIE.2010.2081954

Patil, D., McDonough, M. K., Miller, J. M., Fahimi, B., & Balsara, P. T. (2018). Wireless Power Transfer for Vehicular Applications: Overview and Challenges. *IEEE Transactions on Transportation Electrification, 4*(1), 3-37. doi:10.1109/TTE.2017.2780627

Petersen, M., & Fuchs, F. W. (2015, 19-20 May 2015). *Design of a Highly Efficient Inductive Power Transfer (IPT) System for Low Voltage Applications.* Paper presented at the Proceedings of PCIM Europe 2015; International Exhibition and Conference for Power Electronics, Intelligent Motion, Renewable Energy and Energy Management.

Ramezani, A., & Narimani, M. (2021). Optimal Design of Fully-Integrated Magnetic Structure for Wireless Charging of Electric Vehicles. *IEEE Transactions on Transportation Electrification*, 1-1. doi:10.1109/TTE.2021.3067875

Sasaki, S., Tanaka, K., & Maki, K. (2013). Microwave Power Transmission Technologies for Solar Power Satellites. *Proceedings of the IEEE, 101*(6), 1438-1447. doi:10.1109/JPROC.2013.2246851

Seungyoung, A., & Joungho, K. (2011, 11-15 April 2011). *Magnetic field design for high efficient and low EMF wireless power transfer in on-line electric vehicle.* Paper presented at the Proceedings of the 5th European Conference on Antennas and Propagation (EUCAP).

Shinohara, N. (2013). Beam Control Technologies With a High-Efficiency Phased Array for Microwave Power Transmission in Japan. *Proceedings of the IEEE, 101*(6), 1448-1463. doi:10.1109/JPROC.2013.2253062

Sinha, S., Regensburger, B., Doubleday, K., Kumar, A., Pervaiz, S., & Afridi, K. K. (2017, 1-5 Oct. 2017). *High-power-transfer-density capacitive wireless power transfer system for electric vehicle charging.* Paper presented at the 2017 IEEE Energy Conversion Congress and Exposition (ECCE).

Sohn, Y. H., Choi, B. H., Lee, E. S., Lim, G. C., Cho, G., & Rim, C. T. (2015). General Unified Analyses of Two-Capacitor Inductive Power Transfer Systems: Equivalence of Current-Source SS and SP Compensations. *IEEE Transactions on Power Electronics, 30*(11), 6030-6045. doi:10.1109/TPEL.2015.2409734

Suzuki, M., Ogawa, K., Moritsuka, F., Shijo, T., Ishihara, H., Kanekiyo, Y., . . . Ishida, M. (2017, 26-30 March 2017). *Design method for low radiated emission of 85 kHz band 44 kW rapid charger for electric bus.* Paper presented at the 2017 IEEE Applied Power Electronics Conference and Exposition (APEC).

Tavakoli, R., & Pantic, Z. (2018). Analysis, Design, and Demonstration of a 25-kW Dynamic Wireless Charging System for Roadway Electric Vehicles. *IEEE Journal of Emerging and Selected Topics in Power Electronics, 6*(3), 1378-1393. doi:10.1109/JESTPE.2017.2761763

Theodoridis, M. P. (2012). Effective Capacitive Power Transfer. *IEEE Transactions on Power Electronics, 27*(12), 4906-4913. doi:10.1109/TPEL.2012.2192502

Tran, D. H., Vu, V. B., & Choi, W. (2018). Design of a High-Efficiency Wireless Power Transfer System With Intermediate Coils for the On-Board Chargers of Electric Vehicles. *IEEE Transactions on Power Electronics, 33*(1), 175-187. doi:10.1109/TPEL.2017.2662067

Tritschler, J., Reichert, S., & Goeldi, B. (2014, 26-28 Aug. 2014). *A practical investigation of a high power, bidirectional charging system for electric vehicles.* Paper presented at the 2014 16th European Conference on Power Electronics and Applications.

Villar, I., Garcia-Bediaga, A., Iruretagoyena, U., Arregi, R., & Estevez, P. (2018, 23-27 Sept. 2018). *Design and experimental validation of a 50kW IPT for Railway Traction Applications.* Paper presented at the 2018 IEEE Energy Conversion Congress and Exposition (ECCE).

Vu, V., Tran, D., & Choi, W. (2018). Implementation of the Constant Current and Constant Voltage Charge of Inductive Power Transfer Systems With the Double-Sided LCC Compensation Topology for Electric Vehicle Battery Charge Applications. *IEEE Transactions on Power Electronics, 33*(9), 7398-7410. doi:10.1109/TPEL.2017.2766605

Waffenschmidt, E., & Staring, T. (2009, 8-10 Sept. 2009). *Limitation of inductive power transfer for consumer applications.* Paper presented at the 2009 13th European Conference on Power Electronics and Applications.

Wang, Q., & Wang, Y. (2018). Power efficiency optimisation of a three-coil wireless power transfer using compensatory reactance. *IET Power Electronics, 11*(13), 2102-2108. doi:https://doi.org/10.1049/iet-pel.2018.5378

Yilmaz, M., & Krein, P. T. (2013). Review of Battery Charger Topologies, Charging

Power Levels, and Infrastructure for Plug-In Electric and Hybrid Vehicles. *IEEE Transactions on Power Electronics, 28*(5), 2151-2169. doi:10.1109/TPEL.2012.2212917

Zaheer, A., Covic, G. A., & Kacprzak, D. (2014). A Bipolar Pad in a 10-kHz 300-W Distributed IPT System for AGV Applications. *IEEE Transactions on Industrial Electronics, 61*(7), 3288-3301. doi:10.1109/TIE.2013.2281167

Zaheer, A., Kacprzak, D., & Covic, G. A. (2012, 15-20 Sept. 2012). *A bipolar receiver pad in a lumped IPT system for electric vehicle charging applications.* Paper presented at the 2012 IEEE Energy Conversion Congress and Exposition (ECCE).

Zaheer, A., Neath, M., Beh, H. Z. Z., & Covic, G. A. (2017). A Dynamic EV Charging System for Slow Moving Traffic Applications. *IEEE Transactions on Transportation Electrification, 3*(2), 354-369. doi:10.1109/TTE.2016.2628796

Zahid, Z. U., Dalala, Z. M., Chen, R., Chen, B., & Lai, J. (2015). Design of Bidirectional DC–DC Resonant Converter for Vehicle-to-Grid (V2G) Applications. *IEEE Transactions on Transportation Electrification, 1*(3), 232-244. doi:10.1109/TTE.2015.2476035

Zakerian, A., Vaez-Zadeh, S., & Babaki, A. (2020). A Dynamic WPT System With High Efficiency and High Power Factor for Electric Vehicles. *IEEE Transactions on Power Electronics, 35*(7), 6732-6740. doi:10.1109/TPEL.2019.2957294

Zhang, H., Lu, F., Hofmann, H., Liu, W., & Mi, C. C. (2016). A Four-Plate Compact Capacitive Coupler Design and LCL-Compensated Topology for Capacitive Power Transfer in Electric Vehicle Charging Application. *IEEE Transactions on Power Electronics, 31*(12), 8541-8551. doi:10.1109/TPEL.2016.2520963

Zhang, J., Yuan, X., Wang, C., & He, Y. (2017). Comparative Analysis of Two-Coil and Three-Coil Structures for Wireless Power Transfer. *IEEE Transactions on Power Electronics, 32*(1), 341-352. doi:10.1109/TPEL.2016.2526780

Zhang, W., & Mi, C. C. (2016). Compensation Topologies of High-Power Wireless Power Transfer Systems. *IEEE Transactions on Vehicular Technology, 65*(6), 4768-4778. doi:10.1109/TVT.2015.2454292

Zhang, W., Wong, S., Tse, C. K., & Chen, Q. (2014a). Design for Efficiency Optimization and Voltage Controllability of Series–Series Compensated Inductive Power Transfer Systems. *IEEE Transactions on Power Electronics, 29*(1), 191-200. doi:10.1109/TPEL.2013.2249112

Zhang, W., Wong, S., Tse, C. K., & Chen, Q. (2014b). An Optimized Track Length in Roadway Inductive Power Transfer Systems. *IEEE Journal of Emerging and Selected Topics in Power Electronics, 2*(3), 598-608. doi:10.1109/JESTPE.2014.2301460

Zhang, W., Wong, S., Tse, C. K., & Chen, Q. (2015). Load-Independent Duality of Current and Voltage Outputs of a Series- or Parallel-Compensated Inductive Power Transfer Converter With Optimized Efficiency. *IEEE Journal of Emerging and Selected Topics in Power Electronics, 3*(1), 137-146. doi:10.1109/JESTPE.2014.2348558

Zhang, Y., Lu, T., & Zhao, Z. (2014, 14-18 Sept. 2014). *Reducing the impact of source internal resistance by source coil in resonant wireless power transfer.* Paper presented at the 2014 IEEE Energy Conversion Congress and Exposition (ECCE).

Zhao, J., Cai, T., Duan, S., Feng, H., Chen, C., & Zhang, X. (2016). A General Design Method of Primary Compensation Network for Dynamic WPT System Maintaining Stable Transmission Power. *IEEE Transactions on Power Electronics, 31*(12), 8343-8358. doi:10.1109/TPEL.2016.2516023

Zhao, L., Thrimawithana, D. J., & Madawala, U. K. (2017). Hybrid Bidirectional Wireless EV Charging System Tolerant to Pad Misalignment. *IEEE Transactions on Industrial Electronics, 64*(9), 7079-7086. doi:10.1109/TIE.2017.2686301

Zhong, W. X., Zhang, C., Liu, X., & Hui, S. Y. R. (2015). A Methodology for Making a Three-Coil Wireless Power Transfer System More Energy Efficient Than a Two-Coil Counterpart for Extended Transfer Distance. *IEEE Transactions on Power Electronics, 30*(2), 933-942. doi:10.1109/TPEL.2014.2312020

LIST OF PUBLICATIONS AND PAPERS PRESENTED

1. P. Darvish, S. Mekhilef and H. A. B. Illias, "A Novel S–S–LCLCC Compensation for Three- Coil WPT to Improve Misalignment and Energy Efficiency Stiffness of Wireless Charging System," in IEEE Transactions on Power Electronics, vol. 36, no. 2, pp. 1341-1355, Feb. 2021, doi: 10.1109/TPEL.2020.3007832. **, (Accepted)**
2. P. Darvish, A.Hossain,S. Mekhilef H.Illias,N.M.L.Tan , "Design and Analysis of a Three-Coil Topology for WPT Applications", *IEEE Transactions on Power Electronics* , (**Under Review**)